

15 AUGUST 1963

REPORT 5992

COPY NO. 6

(Title -- Unclassified)

FINAL REPORT

PYROLYTIC REFRACTORY THRUST CHAMBER DEVELOPMENT

for the Period
1 July 1962 through 31 March 1963

UNCLASSIFIED

(Title -- Unclassified)

FINAL REPORT,
(PYROLYTIC REFRACTORY THRUST CHAMBER DEVELOPMENT)
for the Period
1 July 1962 through 31 March 1963

IS-17 (NASA Contract NAS 7-54, Amendment 1)
Project 264

(NASA CR-55213) Rept. 5992 CTS. p. 9, 10, 4, 3, 26-1

PREPARED BY

J. G. Campbell
J. G. Campbell,
C. D. Coulbert
C. D. Coulbert, and
Samuel Sklarew
S. Sklarew Aug. 15, 1963 10 14/2

APPROVED BY

M. E. Goodhart
M. E. Goodhart
Senior Project Engineer
Advanced Technology Development

CHECKED BY

C. D. Coulbert
C. D. Coulbert
Project Engineer

UNCLASSIFIED

5807009
THE  CORPORATION
VAN NUYS, CALIFORNIA

CONTENTS

<u>Section</u>		<u>Page</u>
I	SUMMARY.	1
II	INTRODUCTION	2
III	STRESS ANALYSIS.	6
	A. General.	6
	B. Residual Stresses.	6
	C. Proof Stresses	10
	D. Operating Stresses	11
	E. Combustion Chamber Stress Summary.	11
	F. Throat Stress Summary.	12
	G. Methods of Analysis.	13
	H. Effective Strength of Pyrolytic Graphite	22
	I. Discussion of Stress Analysis.	22
IV	RESIDUAL STRESS TEST PROGRAM	24
	A. Pressure Rupture Test Results.	25
	B. Residual Stress Results.	25
V	PYROLYTIC MATERIALS TESTING.	27
	A. Plasma Torch Oxidation Tests	27
	B. Acetylene Torch Oxidation Tests.	28
	C. Compatibility Tests.	28
VI	MOTOR FIRING TESTS	29
	A. Composite Pyrolytic Graphite Motor	29
	B. Free-Standing Boron Nitride Throat	29
	C. Edge Oriented Boron Nitride Throat	30
	D. Tapered Pyrolytic Graphite Motors.	30
VII	BRAZING STUDIES.	32
VIII	OTHER PYROLYTIC MATERIALS.	33
IX	CONCLUSIONS.	35
X	RECOMMENDATIONS.	36
XI	REFERENCES	38

CONTENTS (Continued)

<u>Section</u>	<u>Page</u>
-- TABLE I -- Average Wall Thickness of Tubes Before Machining. . . .	38
-- TABLE II -- Anneal History of Pyrolytic Graphite Tubes	39
-- TABLE III -- Results of Pressure Rupture Test.	40
-- TABLE IV -- Results of Residual Stress Test.	41
-- TABLE V -- Results of Plasma Torch Testing of Pyrolytic Materials. .	42
-- TABLE VI -- Results of Acetylene Torch Testing of Pyrolytic Materials.	44
-- TABLE VII -- Summary of Test Data for Pyrolytic Graphite Thrust Chambers	45
-- APPENDIX A -- Summary of Nomenclature.	94
-- DISTRIBUTION	96

UNCLASSIFIED

ILLUSTRATIONS

<u>Figure</u>	<u>Page</u>
1. Residual Stress on Inside Surface.	46
2. Residual Stress on Outside Surface	47
3. Residual Stress on Middle a-b Plane.	48
4. Longitudinal and Tangential Stresses on the Inside Surface of Pyrolytic Graphite Cylinders and Cones	49
5. Longitudinal and Tangential Stresses on the Outside Surface of Pyrolytic Graphite Cylinders and Cones	50
6. Circumferential Growth Stress.	51
7. Free Standing Pyrolytic Graphite Motor	52
8. Axial Residual Stress - Outside Surface of Throat.	53
9. Circumferential Proof Stress - Inside Surface of Combustion Chamber - Stress Free Temperature = 0°F.	54
10. Circumferential Proof Stress - Inside Surface of Combustion Chamber - Stress Free Temperature = 2000°F	55
11. Circumferential Proof Stress - Inside Surface of Combustion Chamber - Stress Free Temperature = 3000°F	56
12. Circumferential Proof Stress - Inside Surface of Combustion Chamber - Stress Free Temperature = 4000°F	57
13. Circumferential Proof Stress - Inside Surface of Combustion Chamber - As-Deposited Material.	58
14. Circumferential Proof Stress - Outside Surface of Combustion Chamber - As-Deposited Material.	59
15. Axial Proof Stress - Outside Surface of Combustion Chamber - As-Deposited Material.	60
16. Circumferential Proof Stress - Optimum Thickness-Radius Ratio - Combustion Chamber	61
17. Circumferential Proof Stress - Inside Surface of Throat - As-Deposited Material.	62

MAC A63

UNCLASSIFIED

UNCLASSIFIED

ILLUSTRATIONS (Continued)

<u>Figure</u>		<u>Page</u>
18.	Circumferential Proof Stress - Outside Surface of Throat - As-Deposited Material.	63
19.	Pyrolytic Graphite Motor Wall Temperatures	64
20.	Pyrolytic Graphite Motor Wall Temperatures	65
21.	Circumferential Operating Stress - Combustion Chamber - $P_c = 50$ psia.	66
22.	Circumferential Operating Stress - Combustion Chamber - $P_c = 150$ psia.	67
23.	Pyrolytic Graphite Motor Wall Temperature - Combustion Chamber.	68
24.	Operating Stress - Combustion Chamber - As-Deposited Material.	69
25.	Operating Stress - Combustion Chamber - As-Deposited Material.	70
26.	Circumferential Operating Stress - Combustion Chamber - As-Deposited Material.	71
27.	Circumferential Operating Stress - Throat - Outside Surface - Stress-Free Temperature = 0°F	72
28.	Circumferential Operating Stress - Throat - As-Deposited Material.	73
29.	Axial Operating Stress - Throat - As-Deposited Material.	74
30.	Axial Operating Stress - Throat - Stress Free Temperature = 0°F (Condition 4).	75
31.	Combustion Chamber Stresses - Stress Free Temperature = 0°F	76
32.	Combustion Chamber Stresses - Stress Free Temperature = 2000°F	77
33.	Combustion Chamber Stresses - Stress Free Temperature = 4000°F	78
34.	Combustion Chamber Stresses - As-Deposited Material.	79
35.	Throat Stresses - Stress Free Temperature = 0°F	80
36.	Throat Stresses - As-Deposited Material (Condition 3).	81

MAC A 673

UNCLASSIFIED

ILLUSTRATIONS (Continued)

<u>Figure</u>		<u>Page</u>
37.	Effect of Axial Load on Proof Stress - Maximum Circumferential Stress - Stress Free Temperature = 4000°F.	82
38.	Effect of Axial Load on Axial Proof Stress - Stress Free Temperature = 4000°F	83
39.	Tensile and Yield Strength of Pyrolytic Graphite in the a-Direction.	84
40.	Composite Pyrolytic Graphite Thrust Chamber Assembly	85
41.	Free Standing Boron Nitride Throat Insert in Ablative Thrust Chamber.	86
42.	Pyrolytic Boron Nitride Washer Throat Insert after 200 seconds Burning Time	87
43.	Sea Level Motor and Injector	88
44.	Sea Level Motor and Injector - Disassembled.	89
45.	Altitude Motor and Injector - Disassembled	90
46.	Tapered Chamber - Injector Joint	91
47.	Samco Pyrolytic Graphite Thrust Chamber.	92
48.	X-Ray Photo of Samco Pyrolytic Graphite Thrust Chamber	93

I. SUMMARY

92159

Pyrolytic materials were evaluated for construction of liquid propellant thrust chambers. The materials investigated included pyrolytic graphite, boron nitride, zirconium carbide and hafnium carbide.

Initial and steady state stresses in free-standing pyrolytic graphite motors were analyzed for several possible residual stress distributions and an approach to design optimization was studied. The strength of the heat treated pyrolytic graphite cylinders evaluated experimentally was increased by several different annealing cycles at temperatures between 2000°F and 3200°F.

Motor firing tests of 25 pound and 100 pound thrust chambers showed boron nitride to be inferior to pyrolytic graphite in erosion/oxidation resistance to combustion gases containing water vapor.

Comparative oxidation rate tests with plasma and oxy-acetylene torches were performed on 15 pyrolytic materials, with lowest oxidation rates obtained on a pyrolytic zirconium carbide - graphite alloy and on magnesium oxide. Twelve pyrolytic materials were tested at room temperature for compatibility with N_2O_4 , 90% H_2O_2 , MMH and Aerozine 50; none were affected. Attempts to braze pyrolytic graphite to Type 321 stainless steel were unsuccessful due to delaminations and fracture of the pyrolytic graphite.

Free-standing pyrolytic graphite structures have also been considered for re-entry nose cones and leading edges. During extensive testing and prototype production, it was found that the anisotropy which is responsible for the material's unusual properties also creates some special problems of a severity and complexity which had not been foreseen.

With the close concurrence of these disappointing results in several types of application, the earlier sentiment of extreme enthusiasm turned to one of skepticism regarding the potentialities of pyrolytic graphite. However, the development of new high temperature materials has been a slow process, with many false starts recorded for every success. Therefore, with so few candidate materials for use in very high temperature environments, it seems prudent to make a thorough, even though slow, search for ways to utilize and improve the best properties of this material while avoiding the consequences of its unfavorable characteristics.

Although intensive efforts had been made to use pyrolytic graphite coatings in propulsion system combustion chambers, the possibility of using free-standing pyrolytic graphite as the primary thrust chamber structure was at first overlooked. The first experimental firing of such a thrust chamber was performed at the Jet Propulsion Laboratory, California Institute of Technology, in 1961. Shortly thereafter, similar thrust chambers were tested at Marquardt using liquid propellants. Free-standing pyrolytic graphite chambers are particularly applicable to liquid rockets for space propulsion systems, which are frequently designed for system optimization to operate at chamber pressures of 150 psia or less.

The motor firings at Marquardt were part of a program, sponsored by the National Aeronautics and Space Administration, to investigate analytically and experimentally the feasibility and advantages of using free-standing pyrolytic graphite or similar pyrolytic materials for a radiation cooled, liquid rocket thrust chamber for operation in space.

During the first year's work, reported in Reference 1, two small free-standing motors, with a throat diameter of 0.75 inch, were successfully tested at a chamber pressure of 100 psia, using the propellants $N_2O_4/0.75 N_2H_4-0.25 MMH$. The motors were made of an alloy of pyrolytic graphite containing a small amount of boron, which at the time was thought to increase the strength and oxidation resistance of the pyrolytic graphite. Throat erosion rates of about 0.2 mil/sec were measured.

Although both of the free-standing chambers tested at Marquardt successfully withstood a firing chamber pressure of 100 psia and a proof test pressure of 135 psig, it had been found by JPL that the reliability of similar motors in proof testing was marginal, which was attributed to the residual stresses existing in the free-standing chambers. Also, pyrolytic graphite was known to be anisotropic, and the effect this condition would have on motor stresses and strength during operation was not known.

Therefore, stress studies of free-standing motors were begun at Marquardt, and progressed to the development of a method of analysis which would be applicable not only to the analysis of residual stresses, but of operational stresses as well.

Since the structural capability of free-standing pyrolytic graphite motors might not be sufficient for all desired applications, several composite motors were designed to permit use of some of the best properties of the material, although with a sacrifice of part of the potential weight saving offered by the free-standing concept. The composite designs were based on use of a nozzle machined in flat pyrolytic graphite disks, with the a-b plane normal to the motor axis. Tests of several of these motors were partially successful but revealed problems of sealing and differential thermal expansion of the chamber elements.

In addition to pyrolytic graphite, a number of other high temperature materials have been made by the vapor deposition process, sometimes involving pyrolysis of the source gas, other times involving reduction or reaction between the source gas and the substrate. In any case, these materials were in a form never before available, and their applicability to thrust chamber design was also included in the investigation. A number of the materials were tested for oxidation resistance in a water vapor bearing plasma torch, and several free-standing motors of pyrolytic boron nitride were purchased.

This report presents the results of a nine-month study which was a continuation of the first year's work, and was directed toward the following objectives:

1. Analysis of the structural capability of free-standing thrust chambers fabricated from pyrolytic graphite and other pyrolytic materials, and definition of the importance of mechanical properties in determining their structural capability.
2. Investigation of the sources and possible remedies for the problems of residual stress in pyrolytic graphite.
3. Design, fabrication and test firing of complete liquid rocket thrust chamber assemblies fabricated from the most promising pyrolytic refractories.

In order to achieve these objectives the following program was conducted:

1. Stress analysis of free-standing pyrolytic graphite motors was performed to determine stresses in the combustion chamber and nozzle throat walls for various loading conditions of residual stress, initial motor firing and steady state motor firing. A wide range of possible residual stress distributions were considered in order to establish whether or not the structural capability of the motors could be improved by some optimization of residual stress.

2. A program of experimental heat treating and structural testing of free-standing pyrolytic graphite cylinders was performed to investigate the possibility of modifying the residual stresses or increasing the strength of the cylinders. The results of the testing program were examined for clues to the cause of residual stress and the reason for the reduction of effective strength of free-standing pyrolytic graphite cylinders, as compared to the strength of flat specimens.
3. Motor firings of composite design and free-standing pyrolytic graphite motors were performed. The free-standing motor had a conical combustion chamber and expansion skirt, and was intended to be an optimum design to minimize residual stress and motor-injector attachment weight. Motor firings were also made to test the oxidation resistance of pyrolytic boron nitride in an actual combustion environment.
4. Ten pyrolytic materials were tested for oxidation and erosion resistance in a plasma torch containing water vapor, and five materials were tested in an oxy-acetylene flame.
5. The structural capability of these and other new pyrolytic materials was evaluated by observing their brittleness and structure. Two motors made of a new form of pyrolytic graphite, known as Pyroid, were purchased and examined by X-ray.
6. The compatibility of twelve pyrolytic materials in N_2O_4 , 90% H_2O_2 , monomethyl hydrazine and 0.5-hydrazine-0.5 UDMH was determined by room temperature immersion tests.
7. Attempts were made to develop techniques for brazing pyrolytic graphite to stainless steel, which if successful would be very useful as a light weight attachment between motor and injector.

III. STRESS ANALYSIS

A. General

A stress analysis was made of free-standing pyrolytic graphite motors, using a cylindrical model to describe the combustion chamber and throat regions. The method of analysis developed is applicable to other pyrolytic materials, such as boron nitride, which have the same type of anisotropy as pyrolytic graphite. However, all numerical results are for pyrolytic graphite which is the only material which has demonstrated sufficient structural capability to date. No attempt was made to analyze stresses in regions of greater geometrical complexity such as attachment points or in the nozzle convergent region.

The stresses occurring in a free-standing pyrolytic graphite motor were analyzed for three loading conditions, defined as follows:

1. Residual Stresses

These are the stresses which exist in pyrolytic graphite at room temperature (approximated as 0°F for convenience) before any pressure or thermal stresses are imposed.

2. Proof Stresses

These are the stresses which occur in a motor at 0°F after the motor operating pressure is imposed, but before thermal stresses due to motor operation have occurred. The circumferential proof stress in the combustion chamber, usually the critical stress in a free-standing motor, is closely approximated by the stress in a combustion chamber during a static proof test. However, since the throat is blocked during such a proof test resulting in chamber pressure at the throat, the throat circumferential stress during a proof test is greater than the throat proof stress as defined here.

3. Operating Stresses

These are the stresses which occur in a motor during steady state motor operation. The motor temperature distribution was taken to be that which would result from the use of $\text{N}_2\text{O}_4/0.5 \text{ N}_2\text{H}_4 - 0.5 \text{ UDMH}$ at an O/F ratio of 2.0 and a C* efficiency of 95%. The motor temperatures for this propellant are typical of those for a number of other propellants such as O_2H_2 , $\text{N}_2\text{O}_4/\text{N}_2\text{H}_4$, and $\text{N}_2\text{O}_4/0.75 \text{ N}_2\text{H}_4 - 0.25 \text{ MMH}$.

B. Residual Stresses1. Anisotropic Stresses

Changes of uniform temperature in pyrolytic graphite cause stresses due to its anisotropic properties. These anisotropic residual stresses can be calculated if the pyrolytic graphite is assumed to be stress-free at some temperature.

Residual stresses in a pyrolytic graphite cylinder of thickness, t , and inside radius, r_i , are shown in Figures 1, 2, and 3 for stress-free temperatures of 2000°F and 4000°F, the latter being approximately the deposition temperature. Extreme values of the circumferential and axial stresses almost always occur at the cylinder surfaces, while maximum radial stresses occur in the center of the cylinder wall. Radial tensile stress at a given thickness-radius ratio is less during proof and operation loading conditions than the residual stress, so only the residual radial stresses are presented in this report. Since the residual stresses are automatically defined by the stress-free temperature, the various anisotropic residual stress distributions will hereinafter be designated simply by their stress-free temperature.

2. As-Deposited Stresses in Cylindrical Combustion Chamber

Residual stresses which have been measured in cylinders are considerably different than those predicted by anisotropic theory for any stress-free condition. Residual stresses measured in pyrolytic graphite which has been deposited on a female mandrel are shown in Figures 4 and 5, for as-deposited material, for material which has been annealed near 4000°F, and for anisotropic material which is stress-free at the deposition temperature. Male mandrels cause much greater residual stresses than female mandrels, and hence are seldom used. Linear extrapolations of the data points for the as-deposited material were used in defining residual stresses for the as-deposited material at other thickness-radius ratios. The residual stresses defined by linear extrapolation will hereinafter be designated as-deposited residual stresses. Other data, not shown, confirm the validity of a linear extrapolation for circumferential as-deposited residual stresses on the inside surface, at least to a thickness-radius ratio of 0.09, and it is likely that such an extrapolation is justifiable for outside surface circumferential stresses. However, the linear extrapolations of axial stresses can only be justified by the lack of any better information, and subsequent conclusions regarding axial stresses at thickness-radius ratios greater than 0.05 or less than 0.03 must be considered tentative.

It is important to realize also that a certain amount of scatter exists in the experimental data, so that the residual stresses in any particular part might easily be as much as 2000 psi greater or less than the assumed as-deposited distribution.

Two factors which have been hypothesized as causing the difference between anisotropic and as-deposited stresses, are growth (variable lattice transformation) during deposition, and stresses in growth cones (nodules) which are always found in pyrolytic graphite.

a. Nodules

Nodules grow in pyrolytic graphite from irregularities on the mandrel surface. It is predicted in Reference 2 that stresses due to the nodules will be compressive on the inside surface and tensile on the outside surface of cylinders deposited on female mandrels. It is also predicted in Reference 2 that the magnitude of nodule stresses will be greater on the outside surface than on the inside surface. Some data were presented in Reference 2 which are consistent with these predictions and partial confirmation can be obtained from Figures 4 and 5 by determining the increment from anisotropic stresses to as-deposited stresses, as tabulated below:

AS-DEPOSITED RESIDUAL STRESS
MINUS ANISOTROPIC RESIDUAL STRESS

	Axial		Circumferential	
t/r_i	0.03	0.05	0.03	0.05
Inside	-3750	-2720	-3200	-2570
Outside	+4140	+2840	+3220	+3020

The signs of the stress increments tabulated above conform with the predictions of Reference 2 but the magnitude of stress on the outside surface is significantly greater than the stress on the inside surface in only two of the four cases tabulated above. The nodule stresses have not been equated quantitatively with the difference between as-deposited and anisotropic stresses. Also, nodules are usually unevenly distributed through pyrolytic graphite, and it is quite possible that stress concentrations exist at some nodules which are much greater than the magnitude of stress indicated by the data tabulated above.

b. Growth

Pyrolytic graphite permanently changes its dimensions when it is exposed to temperatures above 4000°F, with elongation in the a-direction and contraction in the c-direction. The rate and total amount of growth increase with temperature. Also, a small amount of growth occurs below 4000°F. It has been suggested that pyrolytic graphite grows during deposition, so that the material deposited first will have a longer time for growth than that deposited last, leading to stresses within the material. However, an analysis of the stresses due to the growth effect, with material thickness a function of time, has not been accomplished. Therefore, the difference between anisotropic and as-deposited stresses cannot definitely be correlated with growth at the present time. In addition to the difficulty of developing a method of analysis, the effects of stress, temperature and time on the rate and ultimate amount of growth are not known. References 3 and 4 discuss the advisability of using an empirical method to investigate the effect of growth during deposition. However, no results based upon this approach have been published.

Stresses due to growth after deposition can be calculated by methods similar to those used in calculating residual stresses due to cool down. The results of such calculations are shown in Figure 6. Growth in the a-direction was assumed to be 0.5, 1.0, and 2.0%, while the contraction in the c-direction was twice the amount of a-direction growth. Figure 6 shows circumferential stresses which are tensile at the inside surface and compressive at the outside surface. The amounts of a and c-direction growth used in the calculations are representative of the growth reported in Reference 3 for annealing near 4000°F. At higher temperatures, the ratio of c-direction contraction to a-direction growth is about 3 or 4, which increases the growth stresses even more.

3. As-Deposited Stresses at Throat

Some of the factors which have been hypothesized as contributing to as-deposited residual stresses in cylinders have been discussed above. However, the geometry of the throat region of a free-standing motor is even more complex, and predictions of stresses here are difficult because of the uncertain effects of the mandrel on the throat and the effects of the throat geometry on anisotropic stresses due to uniform temperature changes or temperature gradients. This uncertainty is particularly true of axial stresses in the throat, which will be most affected by the convergent-divergent geometry.

Nearly all of the free-standing chambers which have been built to date have had a conventional throat geometry of a C-D nozzle, with a contraction ratio of about 4 and a radius of curvature about equal to the throat diameter. A simple model for analyzing throat stresses has been suggested by one of the major pyrolytic graphite manufacturers. This model assumes that the effect of the throat curvature on the axial stress can be accounted for by superposition of the stresses in a hypothetical cylinder shown in Figure 7, positioned so that its outside surface coincides with the inside surface of the nozzle and its inside surface coincides with the outside surface of the nozzle.

One experimentally measured value of axial residual stress was obtained from the Jet Propulsion Laboratory, California Institute of Technology. The stress was for the outside throat surface of a C-D nozzle which had a radius of curvature equal to the throat diameter. In order to correlate these data with analytical methods, three conditions of residual stress behavior, were defined, all based on a radius of curvature (i.e., radius of the hypothetical cylinder) equal to the nozzle throat diameter. The three conditions are defined as follows:

Condition 1

Axial stresses equal to those of an as-deposited cylinder with the throat thickness-radius ratio. No effect of hypothetical cylinder.

Condition 2

Superposition of axial stresses of an as-deposited cylinder with the throat value of thickness-radius ratio, plus circumferential as-deposited stresses for the opposite surface of the hypothetical cylinder having half the throat thickness-radius ratio (Figure 7).

Condition 3

Superposition of axial stresses of an as-deposited cylinder with the throat value of thickness-radius ratio, plus circumferential stresses for the opposite surface of the hypothetical cylinder, stress-free at 4000°F, and with half the throat thickness-radius ratio (Figure 7).

UNCLASSIFIED

Condition 3 seems to be the most logical assumption. It implies that the increment between anisotropic residual stresses and as-deposited residual stresses, whether it be due to nodules, growth or whatever, need only be applied once at the surfaces of the motor, and that the additional effect of the hypothetical cylinder can be explained strictly in terms of its anisotropic behavior when heated or cooled. This type of behavior has been assumed throughout the report in calculating operating stresses. That is, the operating stresses are the result of superposition of stresses due to anisotropic material behavior when heated from 0°F to the operating temperature distribution, plus the residual stresses, whether they be theoretical for some assumed stress-free condition or the as-deposited residual stresses.

The calculated axial residual stresses at the throat are shown in Figure 8, together with the single experimental data point. Good correlation with Condition 3 is shown. Therefore, although a single data point obviously does not completely resolve such a complicated situation, Condition 3 behavior was assumed for the throat axial residual stresses.

C. Proof Stresses

1. Combustion Chamber

Proof stresses in the combustion chamber are shown in Figures 9 through 15 for several assumed residual stress conditions.

It is seen that an optimum thickness-radius ratio exists for each residual stress condition and each chamber pressure, at which the proof stress is a minimum. (The obvious exception is for 0°F stress-free motors, which by definition will experience only pressure stresses, which steadily decrease with increasing thickness-radius ratios.) If the thickness-radius ratio is decreased from the optimum value, the stress will increase because of the pressure stress; if the ratio is increased from the optimum, the residual stress will increase more rapidly than the pressure stress decreases, so that again the total of the two will increase. The circumferential proof stress at the inside of the combustion chamber for the optimum thickness-radius ratio is shown in Figure 16. It is seen that the minimum possible stress increases steadily with chamber pressure, implying that a free-standing pyrolytic graphite motor will have a maximum permissible chamber pressure, which cannot be increased by making the wall thicker.

Figure 16 also shows a cross-hatched area which is an estimate of possible scatter for as-deposited residual stresses. One of the most important conclusions to be drawn from Figure 16 is that the as-deposited residual stress condition is more favorable for proof loading than if the material followed the theoretical predictions for 3000° and 4000°F stress-free material. The fact that the as-deposited residual stresses are so favorable is just a fortunate coincidence at the present time.

UNCLASSIFIED

UNCLASSIFIED

2. Throat

Circumferential proof stresses in the throat are shown in Figures 17 and 18. Axial proof stress in the throat is not shown since it is more compressive than the residual stress, due to the motor thrust on the expansion skirt during firing.

D. Operating Stresses

Operating stresses in the motor throat and combustion chamber were calculated for steady state motor wall temperatures shown in Figures 19 and 20. A linear temperature gradient from the inside to outside surface was assumed.

1. Combustion Chamber

Circumferential operating stresses for stress-free conditions of 0, 2000 and 4000°F are shown in Figures 21 and 22. Motor operation is the only loading condition found in this study to cause maximum circumferential stresses in the interior of the wall. The stresses plotted are the maximum tensile stresses, regardless of where they occur. Axial operating stresses for the assumed stress-free conditions are much less than the circumferential stresses and are not shown. It is shown in Figures 21 and 22 that the operating stresses, unlike residual and proof stresses, are a function of the radius as well as the thickness-radius ratio, as indicated in Figure 23 which shows combustion chamber wall temperatures for inside radii of 1 and 2 inches.

Axial operating stresses for the as-deposited residual stress distribution are of the same magnitude as the circumferential stresses as shown in Figures 24 and 25. The slight dependence of the operating stresses on radius as well as thickness-radius ratio is again shown in Figure 26.

2. Throat

Circumferential operating stresses at the throat are shown in Figures 27 and 28. Axial operating stresses, shown in Figures 29 and 30, consist of stresses due to operating temperature and pressure, plus superimposed axial residual stresses, which are considered to be those of Condition 3 in Figure 29 and Condition 4 in Figure 30. Condition 4 was defined as being stress-free at 0°F, that is, no residual stresses. It is seen that if a 0°F stress-free condition could be achieved, the axial operating stresses would be much less than for Condition 3 as-deposited residual stresses.

E. Combustion Chamber Stress Summary

It is evident from the results presented that the various possible residual stress distributions have a pronounced effect on the loading condition which produces the maximum tensile stress. This relation is better seen by comparing the summary of important combustion chamber stresses at 150 psia for stress-free material, presented in Figures 31 through 33, with the stresses for as-deposited material, presented in Figure 34. For 0°F stress-free material, the operational

MAC A63

UNCLASSIFIED

stress is much greater than the proof stress. This relation changes progressively as the stress-free temperature increases, so that for 4000°F stress-free material, the proof stress is much more important than the operating stress. For as-deposited material, the axial stresses, which are unimportant for the various stress-free assumptions, become of comparable magnitude at some thickness-radius ratios. Operational stresses exceed proof stresses in as-deposited material at thickness-radius ratios less than about 0.07, but the proof stress is much greater at larger ratios. However, in comparing operating and proof stresses, the importance of the assumptions of constant material properties must be considered. As will be shown later, the most important elastic constants are the modulus of elasticity in the a-direction and the thermal expansion coefficient in the c-direction. For residual and proof stresses, material properties are needed only between 0° and 4000°F, and the assumed average values of the elastic constants are valid. For the operating stresses, however, part of the wall is over 4000°F, and the modulus of elasticity starts to decrease rapidly at this temperature, which would tend to decrease stresses. Furthermore, the thermal expansion above 4000°F is complicated by the simultaneous occurrence of growth, which might tend to increase stresses. In view of these factors, the calculated operating stresses cannot be considered as accurate as the residual and proof stresses.

The question naturally arises as to what residual stress condition would be optimum for the combustion chamber to best meet all three loading conditions. From Figures 31 through 34, and considering optimum thickness-radius ratios in all cases to reduce the stress as much as possible, it can be seen that both materials with a stress-free temperature of 2000°F, and material with as-deposited residual stresses, would have an optimum stress of 7000 psi. Material stress-free at 4000°F would have an optimum stress of 8100 psi, and material stress-free at 0°F would have the highest optimum stress of all, 9300 psi. Therefore, the condition of zero residual stresses, which one might think would be the ultimate goal, is actually the worst of the four residual stress conditions considered, at least for the combustion chamber. Of course, the analysis has used constant material properties, and the operating stresses in particular are probably conservatively high. But the principle conclusion can still be drawn that there is not any unusual advantage to any of the residual stress conditions assumed. A hypothetical residual stress distribution could possibly be specified which might permit lower stresses at the optimum thickness-radius ratio, but this has not yet been done. Furthermore, methods of achieving any particular residual stress condition desired do not presently exist.

F. Throat Stress Summary

Important throat stresses are shown for a 0°F stress-free condition in Figure 35 and for as-deposited (Condition 3) material in Figure 36. The operational stress exceeds the proof stress for 0°F stress-free material, just as it does in the combustion chamber. For the as-deposited material, proof stresses are greatest at large thickness-radius ratios, and proof or residual stresses are close to the maximum (operational) stresses at small thickness-radius ratios. Again, the optimum stress for as-deposited material would be slightly less than for 0°F stress-free material, but there is not enough difference to make one much preferable to the other.

UNCLASSIFIED

G. Methods of Analysis

1. General Solution

The stress analysis results were obtained from a digital computer program for the general solution of the stresses in the center of an infinitely long cylinder, using cylindrical coordinates r , θ , and z . The c -direction of the pyrolytic graphite is parallel to the radial direction r , and the a - b plane of pyrolytic graphite is concentric with the cylindrical planes containing the axial direction z and the circumferential direction θ . Perfectly elastic material behavior was assumed, with axially symmetric temperature and internal pressure. Axial plane strain exists in such a cylinder, and all shear stresses and strains vanish. Pyrolytic graphite is a transversely isotropic material with the axis of symmetry in the c -direction. Therefore, the generalized Hooke's law can be written as follows:

$$\epsilon_{\theta\theta} = s_{11} \sigma_{\theta\theta} + s_{12} \sigma_{zz} + s_{13} \sigma_{rr} + \alpha_{\theta\theta} T \quad (1)$$

$$\epsilon_{zz} = s_{12} \sigma_{\theta\theta} + s_{11} \sigma_{zz} + s_{13} \sigma_{rr} + \alpha_{zz} T \quad (2)$$

$$\epsilon_{rr} = s_{13} \sigma_{\theta\theta} + s_{13} \sigma_{zz} + s_{33} \sigma_{rr} + \alpha_{rr} T \quad (3)$$

$$\sigma_{\theta\theta} = c_{11} \epsilon_{\theta\theta} + c_{12} \epsilon_{zz} + c_{13} \epsilon_{rr} - \gamma_{\theta\theta} T \quad (4)$$

$$\sigma_{zz} = c_{12} \epsilon_{\theta\theta} + c_{11} \epsilon_{zz} + c_{13} \epsilon_{rr} - \gamma_{zz} T \quad (5)$$

$$\sigma_{rr} = c_{13} \epsilon_{\theta\theta} + c_{13} \epsilon_{zz} + c_{33} \epsilon_{rr} - \gamma_{rr} T \quad (6)$$

Where

T = Temperature increment from some reference stress-free state

s_{ij} = Elastic compliances

c_{ij} = Elastic stiffnesses

α_{ij} = Coefficients of thermal expansion

γ_{ij} = Thermal stress coefficients

ϵ_{ij} = Strain

σ_{ij} = Stress

The system of symbols and subscripts is the same as used in Reference 1 and is explained in Reference 5.

MAC 163

UNCLASSIFIED

The thermal stress coefficients γ_{ij} can be written in terms of the stiffnesses (Reference 5) as follows:

$$\gamma_{\theta\theta} = (c_{11} + c_{12}) \alpha_{\theta\theta} + c_{13} \alpha_{rr} \quad (7)$$

$$\gamma_{rr} = 2 c_{13} \alpha_{\theta\theta} + c_{33} \alpha_{rr} \quad (8)$$

The stiffnesses can be written in terms of the compliances (Reference 5) as follows:

$$c_{11} + c_{12} = s_{33}/X_1 \quad (9)$$

$$c_{11} + c_{12} = 1/(s_{11} - s_{12}) \quad (10)$$

$$c_{13} = -s_{13}/X_1 \quad (11)$$

$$c_{33} = (s_{11} + s_{12})/X_1 \quad (12)$$

where

$$X_1 = s_{33} (s_{11} + s_{12}) - 2 s_{13}^2 \quad (13)$$

The compliances can be defined in terms of the following conventional elastic constants (Reference 5):

$$s_{11} = \frac{1}{E_1} \quad (14)$$

$$s_{33} = \frac{1}{E_3} \quad (15)$$

$$s_{12} = \frac{\nu_{12}}{E_1} \quad (16)$$

$$s_{13} = \frac{\nu_{13}}{E_1} \quad (17)$$

For this problem, the equilibrium equations reduce to the following (Reference 6):

$$\frac{d\sigma_{rr}}{dr} + \frac{\sigma_{rr}}{r} (1 - \sigma_{\theta\theta}) = 0 \quad (18)$$

The strain displacement equations are as follows:

$$\epsilon_{rr} = \frac{du}{dr} \quad (19)$$

and

$$\epsilon_{\theta\theta} = \frac{u}{r} \quad (20)$$

where u = radial displacement.

By substituting from the stress-strain equation, and denoting the constant axial strain by C_3 , we can get the following differential equation:

$$\frac{d^2u}{dr^2} + \frac{1}{r} \frac{du}{dr} - \frac{c_{11}}{c_{33}} \frac{u}{r^2} = \frac{(\lambda_{rr} - \lambda_{\theta\theta}) T - (c_{13} - c_{12}) C_3}{c_{33} r} + \frac{\lambda_{rr}}{c_{33}} \frac{dT}{dr} \quad (21)$$

The derivation of a comparable equation, using a different axis of symmetry, is presented in Reference 7.

If we let

$$A^2 = \frac{c_{11}}{c_{33}} \quad (22)$$

and let

$$\phi = \frac{\lambda_{rr} - \lambda_{\theta\theta}}{c_{33}} \frac{T}{r} + \frac{\lambda_{rr}}{c_{33}} \frac{dT}{dr} + \frac{(c_{12} - c_{13}) C_3}{c_{33}} \frac{1}{r} \quad (23)$$

the solution to Equation (21) can be written as follows:

$$u = (C_1 + V_1) r^A + (C_2 + V_2) r^{-A} \quad (24)$$

where C_1 and C_2 are constants of integration, and

$$V_1 = \frac{1}{2A} \int r^{-A+1} \phi \, dr \quad (25)$$

$$V_2 = - \frac{1}{2A} \int r^{A+1} \phi \, dr \quad (26)$$

A linear radial temperature gradient of the following form:

$$T = a_0 + a_1 r \quad (27)$$

was assumed, and by combining Equations (23) through (27) an equation for u can be obtained. Then, by use of Equations (19) and (20), Equations (4), (5) and (6) can be written as follows:

$$\begin{aligned} \sigma_{\theta\theta} = & (c_{11} + A c_{13}) C_1 r^{A-1} + (c_{11} - A c_{13}) C_2 r^{-A-1} + \left[c_{12} + \frac{D(c_{11} + c_{13})}{1-A^2} \right] C_3 \\ & + \frac{(c_{11} + c_{13}) B a_0}{1-A^2} + \frac{(c_{11} + 2c_{13})(B+C) a_1 r}{4-A^2} + \lambda_{\theta\theta} a_0 - \lambda_{\theta\theta} a_1 r \end{aligned} \quad (28)$$

$$\begin{aligned} \sigma_{zz} = & (c_{12} + A c_{13}) C_1 r^{A-1} + (c_{12} - A c_{13}) C_2 r^{-A-1} + \left[c_{11} + \frac{D(c_{12} + c_{13})}{1-A^2} \right] C_3 \\ & + \frac{(c_{12} + c_{13}) B a_0}{1-A^2} + \frac{(c_{12} + 2c_{13})(B+C) a_1 r}{4-A^2} - \lambda_{\theta\theta} a_0 - \lambda_{\theta\theta} a_1 r \end{aligned} \quad (29)$$

$$\begin{aligned} \sigma_{rr} = & (c_{13} + A c_{33}) C_1 r^{A-1} + (c_{13} - A c_{33}) C_2 r^{-A-1} + \left[c_{13} + \frac{D(c_{13} + c_{33})}{1-A^2} \right] C_3 \\ & + \frac{(c_{13} + c_{33}) B a_0}{1-A^2} + \frac{(c_{13} + 2c_{33})(B+C) a_1 r}{4-A^2} - \lambda_{rr} a_0 - \lambda_{rr} a_1 r \end{aligned} \quad (30)$$

Where

$$B = \frac{\lambda_{rr} - \lambda_{\theta\theta}}{c_{33}} \quad (31)$$

$$C = \frac{\lambda_{rr}}{c_{33}} \quad (32)$$

$$D = \frac{c_{12} - c_{13}}{c_{33}} \quad (33)$$

UNCLASSIFIED

If complete axial restraint is assumed, $C_3 = 0$, and only the two constants of integration C_1 and C_2 must be evaluated, which can be done by specifying the radial pressure σ_{rr} at the inner and outer radii, and substituting into Equation (30), getting two equations in two unknowns.

For a finite axial strain, C_3 will not be zero, and must be obtained from the boundary condition as follows:

$$\int_{r_i}^{r_o} \sigma_{zz} r dr = \frac{F_{zz}}{2\pi} \quad (34)$$

where F_{zz} is the axial load, which must be specified. Integration of Equation (34) after substitution for σ_{zz} from Equation (29) leads to the following:

$$\begin{aligned} H_1 (r_o^{A+1} - r_i^{A+1}) C_1 + H_2 (r_o^{-A+1} - r_i^{-A+1}) + H_5 (r_o^2 - r_i^2) C_3 \\ + H_3 (r_o^3 - r_i^3) + H_4 (r_o^2 - r_i^2) = \frac{F_{zz}}{2\pi} \end{aligned} \quad (35)$$

Where

$$H_1 = \frac{c_{12} + A c_{13}}{A + 1} \quad (36)$$

$$H_2 = \frac{c_{12} - A c_{13}}{-A + 1} \quad (37)$$

$$H_3 = \frac{(c_{12} + 2c_{13})(B+C)a_1 - \lambda_{\theta\theta} a_1(4 - A^2)}{3(4 - A^2)} \quad (38)$$

$$H_4 = \frac{(c_{12} + c_{13}) B a_o - \lambda_{\theta\theta} a_o(1 - A^2)}{2(1 - A^2)} \quad (39)$$

$$H_5 = \frac{c_{11}}{2} \frac{(c_{12} + c_{13}) D}{2(1 - A^2)} \quad (40)$$

Equation (35) together with Equation (30) evaluated at the inner and outer radii provide three equations for determination of the three unknowns C_1 , C_2 and C_3 . The stresses are then evaluated from Equations (28), (29), and (30).

MAC 4673

UNCLASSIFIED

2. Effect of Axial Load

If complete axial restraint is assumed, the analysis is simplified to the solution of two equations in two unknowns. This method was used in the previous work (Reference 1) for hand calculation of stresses due to a radial temperature gradient in a thin walled pyrolytic graphite cylinder, assuming that circumferential stresses are not affected by the resultant axial load. Although exact only for isotropic materials, it has been shown by use of the digital computer program that there is practically no effect of axial stresses on circumferential stresses for the linear radial temperature gradients considered. There is a somewhat greater effect on residual stresses, as shown in Figure 37. Circumferential proof stresses on the inside surface of a cylinder are shown to be indistinguishable for zero end load and an end load which would exist in a combustion chamber with a contraction ratio of 4.0 and an expansion coefficient of 1.89. The effect of complete axial restraint is negligible for small thickness-radius ratios and gradually increases to as much as 7% at a thickness-radius ratio of 0.2.

The axial load effect is much more important for axial stress, of course, particularly for thin walls. The following expression can easily be derived for the axial load on the cylindrical portion of a combustion chamber of a free-standing motor for which all thrust is transmitted to the injector head, which is the usual situation for free-standing motors:

$$F_{zz} = P_c A_c \left(1 - \frac{C_F}{\epsilon_c} \right) \quad (41)$$

Where

P_c = Chamber pressure

A_c = Chamber cross sectional area

C_F = Nozzle expansion coefficient

ϵ_c = Chamber contraction ratio

Equation (41) should be used with caution for contraction ratios near 1.0, in which case certain simplifying assumptions usually made in evaluating the expansion coefficient are not valid.

Axial stress in a combustion chamber is shown in Figure 38 for zero end load ($\epsilon_c = C_F$), and for an end load due to a contraction ratio of 4.0 and an expansion coefficient of 1.89. A large decrease in axial stress can be achieved in very thin walls by using a zero axial load.

3. Elastic Constants of Pyrolytic Graphite

The motor stresses were calculated using the following values of the elastic constants:

$$E_1 = 4.0 \times 10^6 \text{ lb/in.}^2$$

$$E_3 = 1.5 \times 10^6 \text{ lb/in.}^2$$

$$\nu_{12} = -0.15$$

$$\nu_{13} = 0.9$$

$$\alpha_{\theta\theta} = 1.0 \times 10^6 \text{ in./in.}^\circ\text{F}$$

$$\alpha_{rr} = 14.0 \times 10^6 \text{ in./in.}^\circ\text{F}$$

The importance of the numerical accuracy of each of the elastic constants was investigated by calculating the residual stress at the inside surface of a cylinder with a thickness-radius ratio of 0.08, assuming no end load and a 4000°F stress-free condition. The value of each constant was varied within limits established by compressibility and strain energy criteria given in Reference 1, keeping all other constants at the nominal values listed above.

a. Modulus of Elasticity in c-Direction

The c-direction modulus was found to be unimportant, as shown below:

E_3	$\sigma_{\theta\theta}$
0.5	8367
1.0	8384
1.5	8389 (nominal value)
2.5	8396

b. Modulus of Elasticity in a-b Plane

The modulus in the deposition plane is of dominant importance, as would be expected.

E_1	$\sigma_{\theta\theta}$
2.5	5246
4.0	8389 (nominal value)
5.0	10,483

c. Poisson's Ratio in a-b Plane

The absolute magnitude of Poisson's ratio in the deposition plane can be important in establishing residual stresses.

ν_{12}	$\sigma_{\theta\theta}$
-0.5	10,923
-0.15	8389 (nominal value)
0.2	8545

d. Poisson's Ratio in a-c Plane

The ratio of contraction in the c-direction to elongation in the loaded a-direction is not important, as shown by the following results:

ν_{13}	$\sigma_{\theta\theta}$
0.5	8390
0.7	8390
0.9	8390 (nominal value)

e. Coefficient of Thermal Expansion in a-b Plane

Quite large percentage changes in the coefficient of thermal expansion in the a-b plane are possible with only moderate effect on the residual stress:

$\alpha_{\theta\theta}$	$\sigma_{\theta\theta}$
0.5×10^{-6}	8712
1.0×10^{-6}	8389 (nominal value)
2.0×10^{-6}	7744
4.0×10^{-6}	6453

f. Coefficient of Thermal Expansion in c-Direction

The coefficient of thermal expansion in the c-direction has a strong effect on the residual stress.

α_{rr}	$\sigma_{\theta\theta}$
7×10^{-6}	3872
10×10^{-6}	5808
14×10^{-6}	8389 (nominal value)
18×10^{-6}	10,971
21×10^{-6}	12,907

4. Simplified Equations

Some of the stresses in pyrolytic graphite can be calculated with good accuracy by the use of several simple equations given below.

a. Pressure Stresses

Circumferential stress in a thin pyrolytic graphite cylinder with 150 psig internal pressure and zero axial load was calculated for a range of thickness-radius ratios. The results are tabulated below:

$\frac{t}{r_i}$	$\frac{Pr_i}{t}$ (psi)	Circumferential Pressure Stress,		$\frac{\sigma_{\theta\theta}, \text{ Inside}}{Pr_i/t}$
		Inside (psi)	Outside (psi)	
0.05	3000	3093	2912	1.031
0.10	1500	1598	1412	1.065
0.15	1000	1103	912	1.103
0.20	750	858	663	1.144

A good approximation of the pressure stresses in thin pyrolytic graphite cylinders can be made by use of the following simple hoop tension equation:

$$\sigma_{\theta\theta} = \frac{Pr_i}{t} \quad (42)$$

b. Residual Stresses

A simple equation for circumferential residual stresses is given in (2).

$$\sigma_{\theta\theta} = \frac{E_1 (\alpha_{rr} - \alpha_{\theta\theta}) T}{2 (1 - U_2^2)} \frac{t}{r_i} \quad (43)$$

This equation gives good correlation with the anisotropic tensile stresses on the inside surface and compressive stresses on the outer surface, but cannot be used for radial temperature gradients. The relative importance of the various elastic constants as previously discussed is consistent with Equation (43). Another method of calculating residual and thermal stress is presented in Reference 8.

H. Effective Strength of Pyrolytic Graphite

The tensile strength of pyrolytic graphite in the a-direction, based on tensile tests of flat specimens, is shown in Figure 39. Strength at room temperature of well over 10,000 psi is indicated, based on the applied load and the cross-sectional area.

Strength of pyrolytic graphite tubes, on the other hand, has generally indicated failure under circumferential pressure stress, in the a-direction, of about 2000 to 4000 psi. If the estimated residual stress in as-deposited cylinders is added to the pressure stress, a total stress at failure of 6000 to 8000 psi is indicated. It is recommended that a tensile strength in the a-direction of 8000 psi be used when estimating the structural capability of free-standing motors. It is probable that the strength of pyrolytic graphite tubes increases with temperature in the same way as the strength of flat samples shown in Figure 39, but this has not been proven. However, it has been observed that free-standing motors operate quite successfully at chamber pressures which frequently cause failure during proof tests at room temperature. This can probably be attributed to either the increase of strength at elevated temperature, or the fact that proof stresses usually exceed the operation stresses, which is generally shown by the stress analysis.

Compressive strength in the a-direction is not well established, but experience indicates that it is probably greater than tensile strength, since most failures are tensile, and it is known that compressive stresses of comparable magnitude often exist on the opposite face of a cylinder. Because of this, very few compressive stresses have been presented from the stress analysis.

Tensile strength in the c-direction is about 500 psi at room temperature and drops to very low values at elevated temperature. However, the operating radial stresses are compressive and compressive strength in the c-direction is very high, so that the most critical radial stresses are residual stresses.

I. Discussion of Stress Analysis

Free-standing pyrolytic graphite motors have been shown to be marginal for operation at chamber pressures up to 150 psia, based on a strength of 8000 psi for cylinders, and a combustion temperature near 5000°F. However, the range of permissible thickness-radius ratios is rather small for this strength, and could be increased considerably by a strength of 10,000 or 12,000 psi. An increase of strength to this amount might well be possible, since flat pyrolytic graphite is this strong or stronger.

It was found that overall capability of the material was not greatly different for any of four widely different residual stress conditions; in fact, the type of residual stress commonly encountered (as-deposited material) is somewhat more favorable than various idealized residual stress states. This is due to the anisotropic nature of pyrolytic graphite, and it has not been found possible to reduce the extent of this anisotropy up to the present time.

The most effective way to reduce the anisotropy would be by reducing the coefficient of thermal expansion in the c-direction.

An increase in thermal conductivity in the c-direction would also be beneficial since lower inside wall temperatures would result, with a reduction in oxidation rate. Operating stresses would also be reduced in many cases. The low c-direction conductivity is one of the great advantages of pyrolytic graphite for many applications, but is not advantageous for a free-standing motor.

It should be noted that the motor stresses are dependent mostly on the ratio of wall thickness to inside radius. This means that large and small motors are equally feasible; in fact, the larger the motor size the thicker the wall could be made, so that a finite erosion rate would have less relative effect on larger motors.

Free-standing pyrolytic graphite motors may well be feasible for advanced liquid propellant systems which have flame temperatures near 6000°F. In fact, some of these systems, such as F_2/H_2 , would probably erode the pyrolytic graphite less than the hypergolic systems which produce water vapor. Although operating stresses would be expected to increase with combustion temperatures, a meaningful evaluation of stresses at these high temperatures would necessitate inclusion of the temperature dependency of material elastic properties in the analysis. Growth rates would be so great near 6000°F that growth stresses during motor firing would also have to be included in the stress analysis. The limitations on structural capability resulting from the combination of growth at 6000°F and the low elastic modulus at 6000°F are not immediately apparent. In fact, growth data from Reference 9 show that growth rate increases rapidly at temperatures of about 4300°F and becomes enough to affect motor stresses of the present analysis within several minutes. Referring to Figure 23, it can be seen that growth could begin to affect the present analysis for thickness-radius ratios above 0.06.

UNCLASSIFIED

IV. RESIDUAL STRESS TEST PROGRAM

A program of annealing and testing of pyrolytic graphite cylinders was conducted to determine the effect of annealing on the residual stresses and strength of the cylinders. Previous annealing done by the major manufacturers of pyrolytic graphite was limited almost exclusively to anneal temperatures above 4000°F. It has been shown both experimentally (Figures 4 and 5) and theoretically (Section III) that growth which occurs above 4000°F after deposition increases the circumferential residual stress on the inside surface of cylinders, which is usually the critical residual stress. This effect explains the results reported in Reference 10, which show a reduction of rupture strength of cylinders annealed above 4000°F. Therefore, it appeared more promising to anneal at intermediate temperatures in the range of 2000° to 3000°F.

Twenty-six tubes were manufactured by High Temperature Materials, Inc., with identical deposition conditions and mandrel design. Each tube was 4 inches long, taken from the center of an 8 inch long tube. The internal diameter was 2 inches, the wall thickness 0.060 inch + 0.000 - 0.005. Each tube was machined on the mandrel side to a depth of 0.003 to 0.005 inch. Any additional machining to meet thickness tolerances was done on the inside surface. The amount of machining done on each tube can be judged from the wall thickness as deposited, listed in Table I. Six tubes were tested by High Temperature Materials, Inc. without annealing, and twenty tubes were annealed by Marquardt before being returned to HTM for testing. The tubes were annealed in pairs, so that one tube could be used to determine the effect on strength, and the other the effect on residual stresses.

The following three annealing facilities were used:

1. The Marshall furnace zirconia tubes electrically heated
2. The Curtiss-Wright furnace with graphite tubes heated by graphite resistance elements
3. Radiant heater tubes placed in axial symmetry inside the pyrolytic graphite tubes

All three facilities were purged with helium or argon. Negligible oxidation occurred in the Curtiss-Wright furnace. However, small amounts of oxidation of pyrolytic graphite occurred in the Marshall furnace and the internal radiant heater.

The anneal history for each tube is given in Table II. The radiant heater facility was automatically controlled so that the inside surface temperature rose to 2000°F at the rate of 2000°F per minute, after which the inner surface was maintained at 2000°F for 2 minutes, followed by cool down. It took 2 or 3 minutes to cool down before the next cycle.

MAC 6673

UNCLASSIFIED

UNCLASSIFIED

A. Pressure Rupture Test Results

The results of pressure rupture tests are given in Table III. Although some variation exists among tubes with the same heat treatment, some trends are obvious. First, three of four as-deposited tubes ruptured at a low pressure, lower in fact, than had been expected, based on previous experience with somewhat similar pyrolytic graphite parts. Second, there is a consistent improvement in strength with increasing number of cycles of internal radiant heating. Annealing at 2500°F also is effective in increasing strength. The effect of 3200°F anneal is difficult to interpret; seven hours was apparently beneficial while 25 hours was ineffective. There is some possibility that growth occurred during the tests at 3200°F at a very slow rate, but enough to counteract the effect of strengthening for the longer test. The temperature at which growth begins, if indeed there is such a threshold, is not known. The lowest temperature for which growth data is available is 3450°F (Reference 9). Growth of 0.09% in the a-direction and 0.3% in the c-direction was reported for 1 hour anneal.

As discussed earlier, it is thought that growth tends to increase the circumferential tension on the inside surface, reducing the pressurization strength. However, one test was performed at temperatures above 4000°F to get comparative data. The rupture pressure of a tube (No. 15) cycled seven times in a 7 hour period between 2500° and 4500°F was one of the lowest of the heat treated tubes although higher than three out of four of the as-deposited tubes. The second tube (No. 16) failed when bumped slightly after anneal, with a straight longitudinal crack indicating tension on the inside surface.

B. Residual Stress Results

Results of the residual stress tests are shown in Table IV. The stresses were calculated by High Temperature Materials, Inc. from strains recorded by rosette strain gages. Two gages were attached on the inside and outside surface 0.5 inch from one end, and two were attached in the center of the tube. The specimens were cut with a hand saw to as small a square area containing the gages as was convenient. It was assumed that all residual strains were then relieved, so that the indicated strains were the negative of the residual strains. The residual stresses were then calculated by the following equations (given by High Temperature Materials, Inc.):

$$\sigma_{\theta\theta} = - \frac{E_1}{1 - \nu_{12}^2} (\epsilon_{\theta\theta} + \nu_{12} \epsilon_{zz}) \quad (44)$$

$$\sigma_{zz} = - \frac{E_1}{1 - \nu_{12}^2} (\epsilon_{zz} + \nu_{12} \epsilon_{\theta\theta}) \quad (45)$$

MAC 6679

UNCLASSIFIED

The circumferential stresses are approximately equal, of opposite sign, on the inside and outside surfaces. The axial stresses are larger in tension on the outside surface than the compressive stresses on the inside surface. This is customary and sometimes is attributed to the effect of growth and mandrel restraint. It is also to be noted that the axial stresses decrease near the free end, which may be due to the fact that all axial stresses become zero at the end.

The principle conclusion drawn from the residual stress test results is that there is no evidence of a large change in the residual stresses for any of the anneal cycles. The circumferential stresses are of the most interest since the ruptured tubes were not loaded axially, and probably the rupture failures occurred in tension at the inside surface. From the center station circumferential stresses on the inside surface (shown in Table IV) it is possible to see a partial correlation between the residual stresses and rupture pressure of tubes exposed to the same heat treatment. Although the inner tensile stress in the two as-deposited tubes was higher than all but one of the heat treated tubes, that one tube (No. 22) was heat treated the same as Tube 21, which recorded a very high rupture stress. On the other hand, there is a consistent trend between decreasing residual stress in Tubes 4, 2, and 6, and the corresponding increased strength of their companion tubes, Numbers 3, 1, and 5. However, the decrease in indicated residual stress is less than the increase in hoop strength in corresponding tubes. That is, the residual stress decreases from 3360 to 2880 in Tubes 4 and 6, while the hoop strength increases from 2720 to 5770 in the corresponding ruptured tubes. This suggests that the strength of the tubes might be controlled by localized stress concentrations which are not fully indicated by strain gage measurements, but which are being released by the heat treatment.

V. PYROLYTIC MATERIALS TESTING

A. Plasma Torch Oxidation Tests

Oxidation of pyrolytic materials by water vapor was investigated using the plasma torch with secondary mixing chamber described in Reference 1. Argon and about 7% hydrogen were heated in the plasma arc, and hydrogen and oxygen were added in the secondary mixing chamber to provide a stoichiometric mixture, with the effluent containing 30% of water vapor by weight. All samples were placed 1.5 inches from the exit of the secondary mixing chamber.

Previous experience indicates that the oxidation rate of pyrolytic graphite samples heated to between 3000° and 4000°F by this plasma torch are much higher than at the throat of a free-standing motor operating at 100 psia with $N_2O_4/0.4 N_2H_4-0.5$ UDMH. However, the plasma tests are considered valuable as an indication of the relative oxidation rates of various materials when exposed to water vapor, which is the principle oxidizing agent in many combustion gases. The results for eleven pyrolytic materials are given in Table V.

Boron nitride near 3900°F had a much smaller erosion rate than pyrolytic graphite, which is consistent with the results of earlier testing. Additions of Mo and Zr to BN lessened its oxidation resistance.

The titanium carbide sample appeared melted far below its expected melting temperature, which may have been due to melting of its oxides. An alloy of tungsten in pyrolytic graphite eroded much more than pyrolytic graphite, confirming similar results reported in Reference 1.

Thin coatings of hafnium carbide and zirconium carbide on ATJ graphite rapidly oxidized, but the oxidized coating showed very good adherence to the graphite, although ultimately a failure would occur. The adherence of the hafnium oxide seemed to be somewhat better than that of the zirconium oxide. The coatings on these samples were found to be about 0.001 inch thick rather than 0.010 inch as ordered. The adherence of the thinner coating to the graphite is probably superior.

The average erosion rate of the alloy of 20% by weight of zirconium carbide in pyrolytic graphite was about one-fourth of that of pyrolytic graphite, due to the retardation of oxidation caused by the presence of the zirconium oxide. The oxide momentarily adheres to the surface, then is removed by the shear forces of the gas flow and is immediately replaced by a new oxide layer from the rapidly oxidized zirconium carbide. Whether the oxide would adhere long enough to be beneficial under the shear forces in a motor throat is not known.

B. Acetylene Torch Oxidation Tests

Several pyrolytic materials were tested in an oxygen acetylene flame. The results are shown in Table VI.

Most of the weight loss of the graphite samples coated with HFC and ZrC was due to oxidation of the graphite after coating failure.

The magnesium oxide sample had the greatest oxidation resistance of any material yet tested, with almost negligible change after a 15 minute test at 3900°F (uncorrected). The sample tested actually consisted of a cluster of contiguous crystals. The boundary planes between crystals, although evident before the test, did not appear to separate or crack during or after the test.

C. Compatibility Tests

Five minute immersion tests were made to determine the compatibility at room temperature of N_2O_4 , 90% hydrogen peroxide, monomethyl hydrazine and 50% hydrazine-50% UDMH with the following materials:

1. Pyrolytic graphite
2. Tungsten - pyrolytic graphite alloy
3. Boron - pyrolytic graphite alloy
4. Boron nitride
5. Titanium carbide
6. 20% zirconium carbide - pyrolytic graphite alloy
7. Tantalum carbide coating on pyrolytic graphite
8. Hafnium carbide coating on graphite
9. Zirconium carbide coating on graphite
10. Silicon carbide
11. Boron nitride - molybdenum alloy
12. Boron nitride - zirconium alloy

No reactions or weight changes of the materials were detected.

VI. MOTOR FIRING TESTS

A number of motors made in part or wholly of pyrolytic materials were tested, using N_2O_4 with either monomethyl hydrazine or a 50-50 mixture of hydrazine and UDMH. Detailed test data are given in Table VII. A description of each type of motor and a summary of test results follows:

A. Composite Pyrolytic Graphite Motor

The composite motor consisted of a pyrolytic graphite combustion chamber liner and an edge oriented pyrolytic graphite throat, surrounded by a graphite case within a steel shell, as shown in Figure 40. Two composite chambers were made. Chamber No. 1 was tested for three runs (5, 6, and 7) of approximately 30 seconds each, separated by several minutes off time. Run No. 8, intended for longer duration, was terminated due to a pin hole failure through the steel case near the junction of the edge oriented throat and the chamber liner. Otherwise, very little erosion was evident on the liner and throat, with an unusually low average throat erosion rate of 0.01 mil/sec. The low erosion rate was no doubt due in part to the fact that steady state temperatures were not reached in the edge oriented pyrolytic graphite, which has a high radial thermal conductivity.

The liner and throat of composite chamber No. 1 were used to make another composite assembly which was also used to test an annular insert of graphite coated with a pyrolytic coating developed by Marquardt and discussed in Section VIII of this report. The annular insert fit snugly within the chamber liner as shown in Figure 40. However, the insert expanded during firing more than the pyrolytic graphite liner, causing a crack in the liner and burnout during run No. 16, which consisted of two 30-second firings plus a third firing of 19 seconds. The pyrolytic RM-005 coating did not appear to be affected by the combustion gases or the thermal expansion. The throat erosion rate on the edge oriented pyrolytic graphite throat during run 16 was 0.0366 mil/sec, about three times greater than measured on the same throat insert during runs 5 through 8.

Composite chamber No. 2 was also tested with an annular insert in the combustion chamber, and although the insert O.D. had been reduced to provide clearance within the liner, the liner again failed because of thermal expansion of the insert. Throat erosion on the throat insert of chamber No. 2 was about the same as for the first runs on chamber No. 2. Again, RM-005 coating on the combustion chamber insert did not appear to be affected. Combustion efficiency during the composite motor tests ranged between 93 and 97%.

B. Free-Standing Boron Nitride Throat

Two motors composed of a pyrolytic boron nitride throat liner salvaged from free-standing motors, within a reinforced phenolic chamber and throat, were tested in 30 second runs separated by off times which varied from run to run.

Chamber No. 1 was tested for four 30 second runs (9 to 12) plus one 20 second run (13). Its appearance after the tests is shown in Figure 41. The throat erosion rate was about 0.47 mil/sec. Combustion efficiency was 94 to 98% for these tests.

Chamber No. 2 had a very thin throat insert, and no erosion data were obtained due to rapid failure.

C. Edge Oriented Boron Nitride Throat

Two motors made of reinforced phenolic with edge oriented pyrolytic boron nitride throats were tested. The throat erosion of one motor was 0.19 mils/sec over a total testing time of 122 seconds. The second motor was tested for 10 runs of 30 seconds each, after which the throat was almost completely destroyed (Figure 42). Combustion efficiency was about 96%. No precise erosion rate data were obtained.

The motor firing tests show that the oxidation or erosion rate of pyrolytic boron nitride is much greater than that of pyrolytic graphite in this type of combustion gas.

D. Tapered Pyrolytic Graphite Motors

A tapered free-standing pyrolytic graphite motor was designed to minimize residual stresses which had caused internal wall delaminations at the throat and near the injector flange of the 100-pound thrust motor tested previously (Reference 1.) Development of a light weight attachment between the motor and injector was also desirable. The design consists of a conical combustion chamber, a conical expansion skirt, and a large radius of curvature in the throat region. The axial residual stress at the throat of such a motor would approach that of Condition 1, shown in Figure 8, as the radius of curvature increases.

Four sea level motors ($\epsilon_e = 1.38$) and one altitude motor ($\epsilon_e = 40$) were purchased from Berylco. The chamber and skirt conical half angles were 7°, 30° and 15°, respectively. A throat radius of curvature of 3 inches, a throat diameter of 0.860 inch, and wall thicknesses of 0.040 to 0.050 inch were specified. The contraction ratio at the injector face was 4.1 and L^* was 8.3 inches. A sea level motor is shown attached to the injector in Figure 43 and disassembled in Figure 44. The disassembled altitude motor is shown in Figure 45. All four motors were X-rayed; no delaminations were found. The wall thickness at the throat of the altitude motor was 0.042 inch.

The four sea level motors were proof tested with water while attached to a dummy injector head and sealed at the throat. Two were checked at 100 psig, a third at 150 psig and the fourth failed at 90 psig. The failure indicated a local high stress region which might have been caused by misalignment of the motor during assembly of the motor and injector.

The dry injector-motor seal was satisfactory in the proof tests; one or two drops of water leaked after 5 to 8 minutes at proof pressures. The injector-motor seal is formed by seating the conical chamber on a conical shoulder of the injector as shown in Figure 46. A large compressive stress between the inner chamber surface and the tapered shoulder is maintained by eight spring loaded bolts acting on a split steel ring through a continuous outer ring as shown in Figure 46.

The injector head assembly built for this motor, including valves, was pressure flow checked. The spray pattern indicated that all fuel flow stream tubes were biased to the right of the centerline, giving a spiral effect at impingement. Oxidizer flows were normal. The best flow pattern was an oxidizer/fuel ratio of about 1.6; as the O/F was increased toward 2.0 the pattern became even more unsatisfactory.

UNCLASSIFIED

Attempts to adequately test a sea level motor using $N_2O_4/0.5 N_2H_4-0.5$ UDMH at an O/F of 1.6, were unsuccessful due to low efficiency combustion of about 76%. Burning runs of 3.4, 9.9, 30.5, and 30.6 seconds were made, but the motor barely became hot. No erosion of the motor occurred, and the motor injector seal was satisfactory. No further motor tests are planned until combustion efficiency is improved.

Part of the reason for the low efficiency may be due to the short L^* ; however, good efficiency has been obtained from other 100-pound thrust motors using an L^* of 8 inches. It is possible that the conical combustion chamber will require a greater L^* , but more probably the poor performance was caused by the bad fuel spray pattern.

Although a low combustion efficiency during the tapered motor tests prevented a complete evaluation of the design, some important results have been obtained from the tapered motor program, as follows:

1. A complete thrust chamber with a 40:1 expansion skirt was fabricated from pyrolytic graphite for the first time.
2. The one motor which was fired did not fail although exposed to some sharp chamber pressure fluctuations due to rough combustion.
3. The light weight conical attachment between injector and motor was found to provide a satisfactory pressure seal. A somewhat more severe sealing problem will be encountered when the chamber wall temperatures reach their maximum values with good combustion efficiency, but the results so far are encouraging.
4. No delaminations were found in any of the four tapered motors, even though the thickness-radius ratio at the throat was about 0.10.

MAC A673

UNCLASSIFIED

UNCLASSIFIED

VII. BRAZING STUDIES

An investigation was made of the feasibility of brazing the a-b plane of pyrolytic graphite to Type 321 stainless steel. Twelve different commercial braze alloys were evaluated to determine their ability to wet and bond to pyrolytic graphite. These alloys were IM Microbraz, Standard Microbraz, J-8100, J-8300, CM-50, CM-53, CM-60, CM-62, AGC-1, AGC-7, Ag-Mn, and Au-Ni.

Four of the above brazes wetted and bonded to pyrolytic graphite more readily than the others. They were: Ag-Mn, CM-62, AGC-7, and J-8300. However, when these alloys were used to attach pyrolytic graphite to Type 321 stainless steel, the joints failed on cooling by delamination of the pyrolytic graphite. A successful braze was apparently achieved between the Type 321 SS and the surface of the pyrolytic graphite, but differential contraction on cooling caused a delamination failure beneath the surface of the pyrolytic graphite.

A mechanical test bar was designed with a slotted channel in one end for insertion of the pyrolytic graphite. In this way, the shear stress acting on the braze joint would be symmetrical on both sides of the pyrolytic graphite. The joint was brazed with J-8300 alloy at 2145°F for 20 minutes in an argon atmosphere. A J-8300 braze filler was obtained from General Electric Company. Its composition is 61% Ni, 19% Cr, 10% Si and 10% Mn.

Two specimens were brazed, but both contained partial fractures or delaminations in the pyrolytic graphite after cooling.

Efforts to braze pyrolytic graphite to Mo/0.5% Ti alloy, Zircalloy-2 and Fansteel 80 are reported in Reference 3. A large number of braze alloys were used, but failure due to delamination occurred in all cases. When an intermediate layer of ZT graphite was placed between the pyrolytic graphite and the Mo/0.5% Ti, an apparently sound joint was formed, but failed at a shear stress of about 100 psi at room temperature. After consideration of the difficulties reported above, and the additional problems which would be encountered in using a brazed joint at high temperatures, it was decided to curtail further effort in brazing.

MAC A 673

UNCLASSIFIED

VIII. OTHER PYROLYTIC MATERIALS

Pyrolytic materials other than pyrolytic graphite were evaluated for use in liquid propellant combustion chambers, and their present state of development is described below, based in part on results reported in Reference 1.

Boron Nitride

Pyrolytic boron nitride has superior oxidation resistance at temperatures below 4000°F. However, at higher temperatures it more readily oxidizes, and it appears that boron nitride is inferior to pyrolytic graphite. It has the same type of anisotropy as pyrolytic graphite, but is not as strong, so that it is not promising as a chamber material for oxidizing combustion gases.

Titanium Nitride

A thin sample of TiN was tested with a piece of graphite behind it to resist the force of the plasma torch exhaust. This material is quite brittle, and the 0.009 inch thickness was completely consumed in 100 seconds in the plasma torch. The oxidation rate of TiN could not be obtained from this test, but structurally it does not appear promising.

Carbides

A number of carbides were tested in water vapor during this and the preceding study (Reference 1). They included ZrC, HfC, NbC, TaC, TiC, and SiC. With the exception of SiC, most of the carbides oxidized quite readily. Thin coatings of HfC and ZrC, although rapidly oxidized, form refractory oxides with a melting temperature of 5020°F for HfO₂ and 4850°F for ZrO₂. Durability of these thin oxide layers is unpredictable. NbC and TaC oxidized readily, or spalled off of their pyrolytic graphite substrates. The sample of TiC evidently oxidized, and it was also quite brittle and did not show any promise as a load carrying material.

Silicon carbide is the only carbide which offers any possibility of use as a load carrying oxidation resistant material. Brittleness is its principle problem. Samples of silicon carbide on graphite received from Raytheon were thinner than the samples tested previously, so no more tests were performed during this period.

Marquardt has developed a SiC type pyrolytic coating, RM-005 and this coating is presently being evaluated under other programs. Two free-standing cylinders were made from the combustion chamber annular inserts mentioned in Section VI by oxidizing the graphite. The cylinders of RM-005 which remained contained hair line cracks.

Pyroid

Space Age Materials Corporation has developed a new method of production of pyrolytic graphite which permits deposition of thicknesses far in excess of those possible by the conventional techniques. They have named this material Pyroid. Two free-standing Pyroid chambers were procured, using the inner dimensions of the free-standing 100 pound thrust motor tested in previous work Reference

MAC A573

UNCLASSIFIED

1. One of the chambers is shown in Figure 47, and an X-ray of the motor is shown in Figure 48. The exit inside diameter is about 1.25 inches, and the wall thickness about 0.75 inch. Numerous delaminations exist within the wall, but even so this type of structure might be practicable. A large growth in the converging section is shown in the X-ray. The two Pyroid motors were not tested because of defects which might be eliminated with further development.

Pyrolytic Graphite Alloys

The most promising new pyrolytic materials are alloys of ZrC and HfC in pyrolytic graphite. Raytheon reports strength of an alloy of 20% ZrC in pyrolytic graphite of 50,000 and 100,000 psi for two tests. The alloy approaches the ductility of pyrolytic graphite which is much less brittle than the pure ZrC. Similar alloys of other carbides in pyrolytic graphite are possible. No free-standing shapes of any of the carbide alloys have been made. As noted in Section V, the oxidation resistance of the 20% ZrC alloy is also improved, at least in the plasma torch environment.

Elements alloyed with pyrolytic graphite include tungsten and boron. Neither element seems to improve oxidation resistance; in fact it is lower with tungsten. Boron in small amounts was one of the first substances to be alloyed with pyrolytic graphite. However, it does not seem to add to the strength or oxidation resistance, in fact there is some evidence that delaminations occur more readily in the boron alloy.

MAC A673

UNCLASSIFIED

IX. CONCLUSIONS

1. Free-standing pyrolytic graphite thrust chambers have been shown analytically to be structurally feasible for combustion gas temperatures near 5000°F, and for chamber pressures up to about 150 psia. Operation at higher pressures is limited by tensile strength and residual stresses of the material.
2. Limitations of feasibility are only slightly affected by chamber size, so that a wide range of thrust levels is possible. Since permissible chamber wall thickness is proportional to motor dimensions, a larger motor can have a thicker wall, so that it will be proportionally less affected by a given amount of erosion than a smaller motor.
3. Free-standing pyrolytic graphite thrust chambers may be feasible for combustion gas temperatures above 5000°F, but analytical confirmation would require consideration of growth and the variation of elastic properties of pyrolytic graphite with temperature.
4. None of the four residual stress cases studied were markedly superior. A residual stress distribution which is advantageous for one loading condition will be relatively unfavorable for another loading condition. This is due to the anisotropic nature of pyrolytic graphite. A finer discrimination between various residual stress conditions would require consideration of the temperature dependence of the elastic properties used in the analysis.
5. An increase in strength of pyrolytic graphite in thrust chamber configurations would permit operation with thicker walls and at higher chamber pressures. The measured strength of small thrust chambers and cylinders is usually between 4000 to 8000 psi, as contrasted to the tensile strength of flat samples of well over 10,000 psi.
6. Several heat treatment histories imposed on pyrolytic graphite cylinders evidently increased the strength from about 5000 psi to as much as 9000 psi. However, it appears that the average strength of the cylinders tested was lower than that of similar cylinders produced in the past. Whether strengthening could be achieved in pyrolytic graphite which is initially stronger, or whether additional strengthening could be achieved by further heat treatment is not known.
7. Strength and residual stress in pyrolytic graphite cylinders fluctuates considerably for supposedly identical specimens. All testing should be done in sufficient quantities to avoid drawing erroneous conclusions based on non-representative samples.
8. Pyrolytic boron nitride is inferior to pyrolytic graphite as an oxidation resistant material in the combustion chamber environment.

9. An alloy of 20% zirconium carbide shows a promising improvement in oxidation resistance over that of pyrolytic graphite, based on plasma torch tests. Tensile strength of this material appears to be much greater than pyrolytic graphite.

10. Pyroid, a new form of pyrolytic graphite, RM-005, a silicon carbide type pyrolytic material, and an alloy of zirconium carbide in pyrolytic graphite are the only pyrolytic materials besides conventional pyrolytic graphite which were found to be potentially useful in liquid propellant thrust chambers.

X. RECOMMENDATIONS

1. Further study of heat treating effects is recommended to better understand its capability for strengthening of pyrolytic graphite.

2. Reasons for the difference between tensile strength of pyrolytic graphite in flat specimens and cylinders should be studied. Such a study should attempt to correlate tensile strength with mandrel design, deposition conditions, nodule size, and other variables of production.

3. Analysis and testing of advanced pyrolytic materials for thrust chamber applications should be continued. An alloy of 20% zirconium carbide in pyrolytic graphite, a silicon carbide type material and Pyroid are especially recommended for further study.

4. Motor firings of a tapered pyrolytic graphite thrust chamber should be continued in order to fully define its operating characteristics.

5. All testing of pyrolytic graphite should be done in quantities sufficiently large to define the variation as well as the average properties of supposedly identical items.

XI. REFERENCES

1. Marquardt Report 5907, "Final Report - Pyrolytic Graphite Rocket Thrust Chamber Development for the Period 8 June 1961 to 7 June 1962", 31 July 1962.
UNCLASSIFIED.
2. Coffin, L. F., Jr., "A Note on the Structure-Property Relationships for Pyrolytic Graphite", Paper Presented at AIAA Launch and Space Vehicle Shell Structures Conference, Palm Springs, California, 1-3 April 1963.
3. Lockheed Missiles and Space Division Report IMSC-80 1376, "Pyrolytic Graphite Final Report", Volume II, 1 June 1962, AD 392 785. CONFIDENTIAL.
4. Garber, A. M., "Pyrolytic Materials for Thermal Protection Systems", Aerospace Engineering, January 1963, pp 126-137.
5. Hearmon, R. F. S., "An Introduction to Applied Anisotropic Elasticity", Oxford University Press. 1961.
6. Timoshenko, S., and Goodier, J. N., "Theory of Elasticity", McGraw Hill, New York, 1951.
7. Atlantic Research Corp., Quarterly Progress Report Through August 1961, Contract No. DA-36-034-ORD-3279 RD, Project No. TB 4-004, "Improvement of the Usefulness of Pyrolytic Graphite in Rocket Motor Applications", 15 September 1961, AD 263475.
8. Levy, S., "Thermal Stresses in Pyrolytic Graphite", Paper Presented at AIAA Launch and Space Vehicle Shell Structures Conference, Palm Springs, California, 1-3 April 1963.
9. General Electric Co., Report No. 60-RL-2564M, "Effects of Annealing on the Structure of Pyrolytic Graphite", November 1960. UNCLASSIFIED.
10. Lockheed Missiles and Space Division, Report IMSC-80 1376, "Pyrolytic Graphite Final Report", Volume I, 1 June 1962, AD 329784. CONFIDENTIAL.

TABLE I

AVERAGE WALL THICKNESS OF TUBES BEFORE MACHINING

Tube No.	Thickness (in.)	Tube No.	Thickness (in.)
1	0.067	14	0.070
2	0.065	15	0.067
3	0.073	16	0.067
4	0.072	17	0.075
5	0.069	18	0.072
6	0.069	19	0.072
7	0.071	20	0.072
8	0.075	21	0.074
9	0.068	22	0.070
10	0.068	23	0.065
11	0.068	24	0.067
12	0.068	25	0.065
13	0.068	26	0.065

TABLE II

ANNEAL HISTORY OF PYROLYTIC GRAPHITE TUBES

Tube No.	Anneal Furnace	Weight Before (gms)	Weight After (gms)	Anneal History
1	Radiation	54.6134	54.0773	50 cycles between 500°F-2000°F
2	Radiation	54.0611	53.5929	50 cycles between 500°F-2000°F
3	Radiation	54.9806	54.844	10 cycles between 500°F-2000°F
4	Radiation	54.0521	53.9071	10 cycles between 500°F-2000°F
5	Radiation	54.8272	50.9916	250 cycles between 1000°F-2000°F
6	Radiation	54.4579	52.0931	250 cycles between 1000°F-2000°F No heat treat
8	Radiation	55.0208	53.3264	250 cycles between 1000°F-2000°F
9	C-W	55.8558	55.8520	30 cycles between 2500°F-3000°F in 7 hours
10	C-W	55.2753	55.2711	30 cycles between 2500°F-3000°F in 7 hours
11	C-W	55.5942	--	7 hours at 2500°F
12	C-W	55.8840	--	7 hours at 2500°F
13	Radiation	55.8603	53.7720	250 cycles between 1000°F-2000°F
14				No heat treat
15	C-W	55.6717	55.6724	7 cycles between 2500°F-4500°F in 7 hours
16	C-W	54.9776	54.9705	7 cycles between 2500°F-4500°F in 7 hours
17	Marshall	55.8712	54.3906	30 hours at 2500°F
18	Marshall	55.5507	54.9794	30 hours at 2500°F
19	C-W	55.2618	55.2576	25 hours at 3200°F
20	C-W	55.8007	55.7935	25 hours at 3200°F
21	C-W	55.4750	55.4748	7 hours at 3200°F
22	C-W	55.7603	55.7583	7 hours at 3200°F
23				No heat treat
24				No heat treat
25				No heat treat
26				No heat treat

TABLE III

RESULTS OF PRESSURE RUPTURE TEST

Tube No.	Rupture Pressure (psig)	Inside Radius (in.)	Wall Thickness (in.)	Pressure Stress (psi)
1	210	1.007	0.058	3650
3	160	1.004	0.059	2720
5	315	1.007	0.055	5770
*7	156	1.0**	0.055**	2840**
8	143	1.009	0.055	2620
10	200	1.006	0.059	3410
12	195	1.003	0.061	3210
13	245	1.008	0.057	4330
*14	74	1.006	0.059	1260
15	140	1.009	0.058	2440
17	340	1.005	0.059	5790
19	120	1.002	0.059	2040
21	315	1.002	0.060	5260
*23	70	1.008	0.059	1200
*25	60	1.007	0.060	1010

* Tested in as-deposited condition.

** Approximate

TABLE IV

RESULTS OF RESIDUAL STRESS TEST

Tube No.	Distance From End	$\frac{t}{r_i}$	Residual Stresses - psi			
			Circumferential		Axial	
			Outside	Inside	Outside	Inside
2	0.5	0.057	-2540	2040	4090	-2090
	2.0	0.057	-1850	3160	5290	-2980
4	0.5	0.056	-2480	2320	4340	-1370
	2.0	0.057	-1800	3360	5270	-2180
6	0.5	0.054	-3110	2950	2490	-500
	2.0	0.054	-2400	2880	3490	-2260
9	0.5	0.058	-3620	--	2770	--
	2.0	0.058	-3010	3730	4000	-2080
11	0.5	0.057	-3050	3290	2420	-730
	2.0	0.059	-2020	3380	4210	-2840
18	0.5	0.058	-2440	2240	4370	-1860
	2.0	0.057	-2470	3380	4080	-2130
20	0.5	0.058	-1180	2920	2740	-1280
	2.0	0.058	-2760	3510	3240	-1710
22	0.5	0.058	-3250	3120	2580	-1170
	2.0	0.057	-2650	3790	3250	-1870
*24	0.5	0.057	-3110	3130	2010	-870
	2.0	0.057	-3110	3800	3750	-1230
*26	0.5	0.057	-3590	3440	2630	-848
	2.0	0.057	-2910	3660	3130	-2780

* Tested in as-deposited condition.

UNCLASSIFIED

TABLE V
RESULTS OF PLASMA TORCH TESTING OF PYROLYTIC MATERIALS

Material	Vendor	Size (ins.)	Run Time (sec)	Sample Temp.* (°F)	Surface Emiss. (Assumed)	Erosion Rate (mil/sec)	Remarks
Boron Nitride	HTM	1 by 1 by 0.065	100	3880	0.35	00.15	
BN with Mo	HTM	1 by 1 by 0.073	100	4195	0.40	0.23	
BN with Mo	HTM	1 by 1 by 0.074	100	3940	0.40	0.34	
Pyrolytic Graphite	GE	1 by 1 by 0.067	100	3810	0.80	0.58	
BN with Zr	HTM	1 by 1 by 0.076	150	3870	0.35	> 0.50	Burned through
BN with Zr	HTM	1 by 1 by 0.076	150	3720	0.35	> 0.50	Burned through
Pyrolytic Graphite	HTM	1 by 1 by 0.065	100	3925	0.80	0.35	
Pyrolytic Graphite	Berylco	1 by 1 by 0.111	100	3935	0.80	0.41	
Titanium Carbide	Raytheon	1.5 by 1.5 by 0.105	30	--	--	--	Melted appearance
W. Pyro-Graphite	Raytheon	1 by 1 by 0.075	100	3815	0.75	0.75	Burned through
0.001 in. TaC on PG	Raytheon	1.5 by 1 by 0.110	6	--	--	--	Coating popped off
0.001 in. ZrC on ATJ Graphite	HTM	1 by 1 by 0.256	25	--	--	0	
0.001 in. ZrC on ATJ Graphite	HTM	1 by 1 by 0.256	50	3980	0.30	0.06	
0.001 in. ZrC on ATJ Graphite	HTM	1 by 1 by 0.256	100	3680	0.30	--	Coating failure
0.001 in. HfC on ATJ Graphite	HTM	1 by 1 by 0.256	25	--	--	0	Erosion on back side
0.001 in. HfC on ATJ Graphite	HTM	1 by 1 by 0.256	50	3870	0.30	0	Erosion on back side
0.001 in. HfC on ATJ Graphite	HTM	1 by 1 by 0.256	100	3780	0.3	0	Erosion on back side
0.001 in. HfC on ATJ Graphite	HTM	1 by 1 by 0.256	100			0.05	Erosion on back side

UNCLASSIFIED

UNCLASSIFIED

TABLE V (Continued)

Material	Vendor	Size (ins.)	Run Time (sec)	Sample Temp.* (°F)	Surface Emiss. (Assumed)	Erosion Rate (mil/sec)	Remarks
20% ZrC in PG	HTM	1 by 1 by 0.015	100	4350	0.35	0.15	Burned through
20% ZrC in PG	Raytheon	1 by 1 by 0.182	100	4170	0.35	0.12	
20% ZrC in PG	Raytheon	1 by 1 by 0.117	100	3900	0.35	0.04	
20% ZrC in PG	Raytheon	1 by 1 by 0.159	100	--	--	0.06	
20% ZrC in PG	Raytheon	1 by 1 by 0.195	100	4230	0.35	0.09	

* Corrected for emissivities of oxidized surface.

MAC A673

UNCLASSIFIED

UNCLASSIFIED

TABLE VI
RESULTS OF ACETYLENE TORCH TESTING OF PYROLYTIC MATERIALS

Material	Size (inches)	Test Time	Sample Temp.* (°F)	Weight Before (gms)	Weight After (gms)	Weight Loss (gms)	Loss (%)	Remarks
Pyrographite SAMCO	1 x 1 x 0.050	2 min 40 sec	3300	1.0470	0.2286	0.8184	78	
0.001 in. HfC on Graphite - HTM	2 x 3 x 1/4	5 min	3900	46.6610	27.6863	18.9747	41	Blistered on front face. Coating turned white and flaked off after run.
0.001 in. ZrC on Graphite - HTM	2 x 3 x 1/4	4 min	3620	46.1130	28.3748	7.7382	17	Coating glazed and peeled off. Test stopped.
20% ZrC in PG - Raytheon	2 x 3 x 1/4	5 min	3400	35.1868	27.6794	7.5074	21	Surface turned white - adherent looks good.
Pyrographite Raytheon	2 x 3 x 1/8	5 min	3400	26.2113	11.5113	14.7000	56	No cracks or delaminations.
Mg O - SAMCO	Approx. 1 in. long x 1/2 in. dia. (Irregular shape)	15 min	3900	18.037	17.997	0.040	< 1	No cracks or change in color. Looks very good.

* Temperatures as reported by Micro Optical Pyrometer - no correction.

UNCLASSIFIED

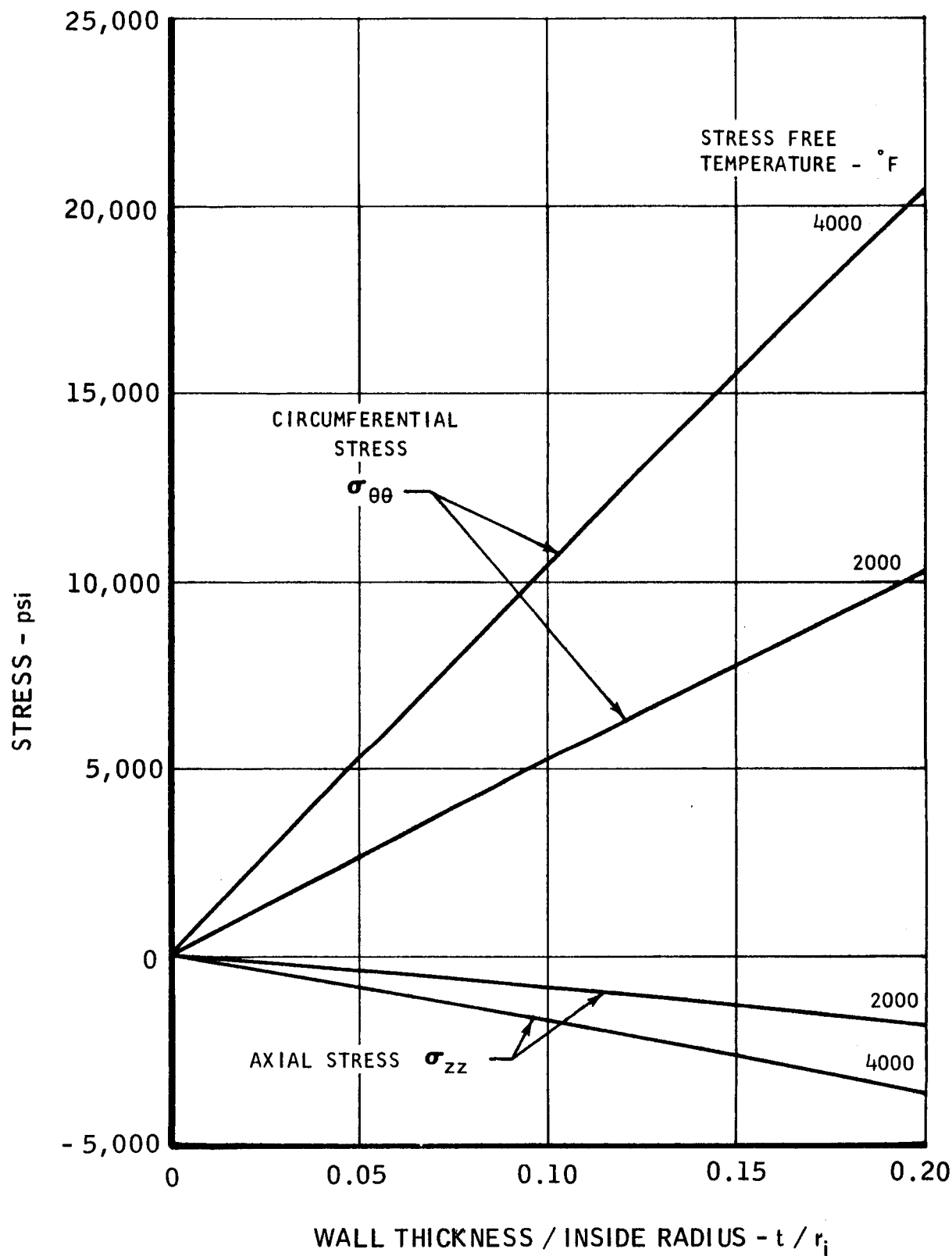
TABLE VII
SUMMARY OF TEST DATA FOR PYROLYTIC GRAPHITE THRUST CHAMBERS

Tests Made at ATL Pad E and AF-MTL Cell 1, 5 to 19 December 1962;
Multiple Doublet (6 on 6) Injector - Fuel Outside - Oxidizer Inside; Sea Level Exhaust Conditions

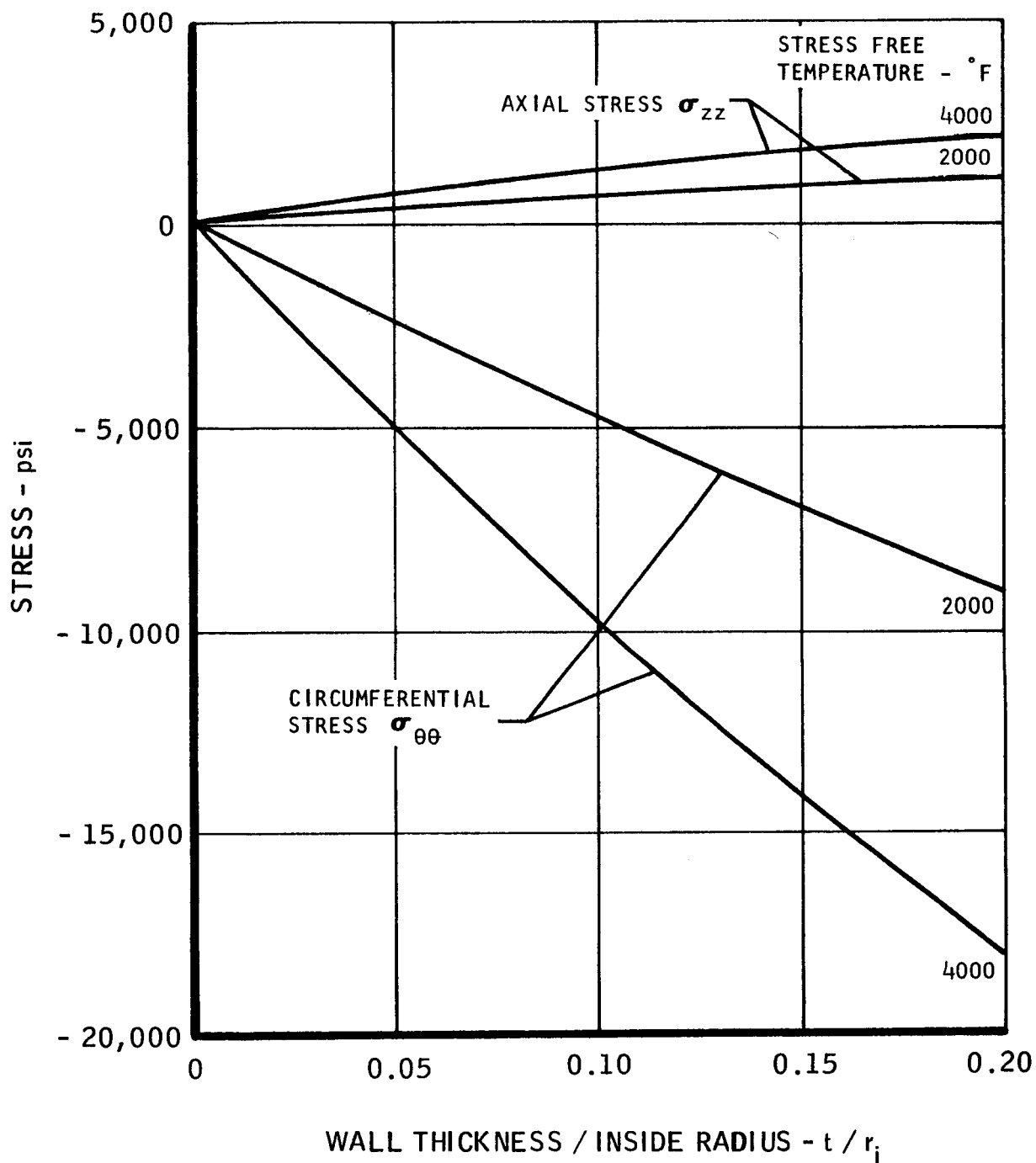
Thrust Chamber Description	Chamber Number	Test Dates	Propellants	O/F	P _c (psia)	F _{max} (lbf)	Propellant Flow (pps)	η_{c*} (%)	D _t Before	D _t After	Run No.	Time (sec)	Accum. Run Time (sec)	Average Erosion Rate (mil/sec)	Remarks
Reinforced Phenolic with Boron Nitride Washer Throat Insert (Cell 1)	1	12-5-62	N ₂ O ₄ /50% N ₂ H ₄ -50% UDMH	1.60	96.5	14.1	0.0765	94	0.4085**	--	1	30.0			
				1.60	106.0	15.2	0.0782	--	--	--	2	29.5			
				1.63	105.5	15.2	0.0786	--	--	0.4550	3	63.0	122.50	0.190	
	2	12-6-62		1.59	109.0	14.5	0.0752	102.5	0.3990**	0.5190 (calc.)	4	10 x 30	298	0.201 min. 2.00 max.	Throat eroded to point of mechanical failure.
Composite Pyrolytic Graphite (Pad E)	1*	12-7-62	N ₂ O ₄ /UDMH	1.71	107.0	50.0	0.274	98	0.7514**	--	5	29.6			Chamber burned through at joint of chamber and exit nozzle sections.
				1.72	107.5	50.5	0.271	--	--	--	6	29.2			
				1.67	105.0	50.0	0.272	--	--	--	7	29.8			
				1.70	105.0	49.0	0.275	96	--	0.7545**	8	49.1	137.7	0.0105	
Reinforced Phenolic with Free Standing Boron Nitride Throat Insert (Pad E)	1	12-10-62 12-12-62	N ₂ O ₄ /UDMH	1.92	110.5	41.5	0.236	98	0.6855**	0.7062	9	30.8			Large portion of Boron Nitride throat eroded during run.
				1.74	101.5	39.5	0.238	94	0.7062**	0.7315	10	28.8			
				1.85	102.5	46.0	0.265	97	0.7315**	--	11	30.2			
				1.69	105.0	47.5	0.280	--	--	--	12	30.1			
				1.52	93	43.0	0.282	--	--	0.8170	13	20.0	139.9	0.477	
	2	12-18-62		1.80	100.0 50.0	54.0 52.0	0.298 0.368	96 97	0.8088** --	-- 1.2716**	15	11 x 30	330		Endurance run on ablative section.
Composite Pyrolytic Graphite, Silicon Carbide Coated Chamber Inserts (Pad E)	1*	12-19-62	N ₂ O ₄ /UDMH	1.81	102.0	52.0	0.281	93	0.7545**	0.7603	16	79.3	217	0.0366	Thermal expansion of insert cracked chamber wall.
	2	12-14-62		1.83	109.0	51.5	0.274	100	0.7494**	0.7511	14	52.1	52.1	0.0163	

* Chamber repaired after 7 December test and silicon carbide coated carbon insert added prior to 19 December test.

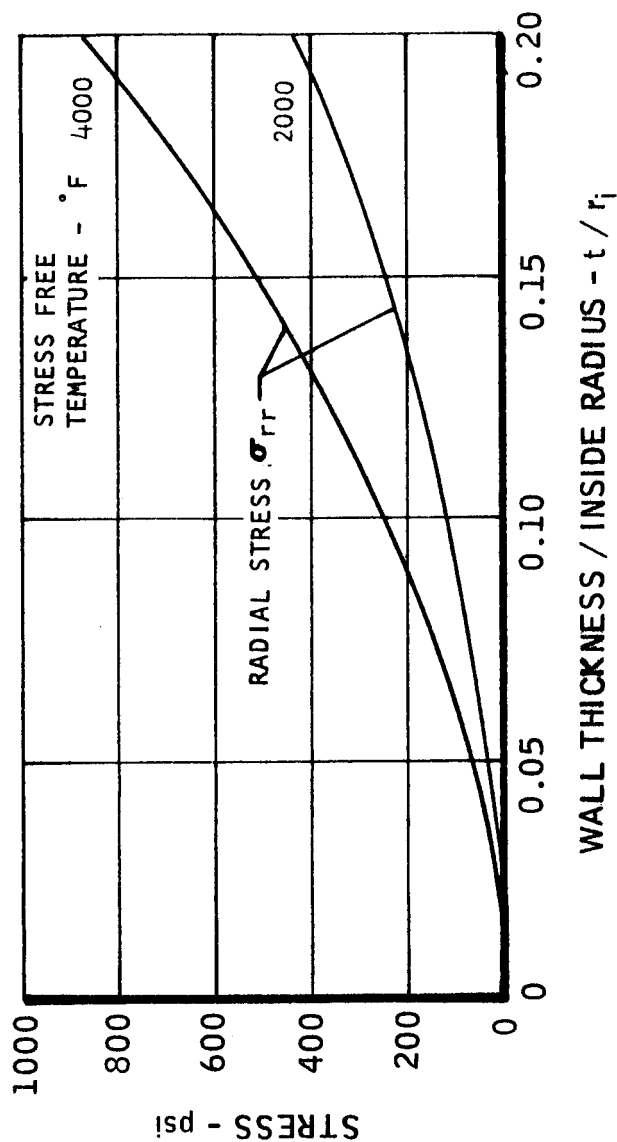
** Throat diameters used to calculate C*

RESIDUAL STRESS ON INSIDE SURFACE
PYROLYTIC GRAPHITE CYLINDER

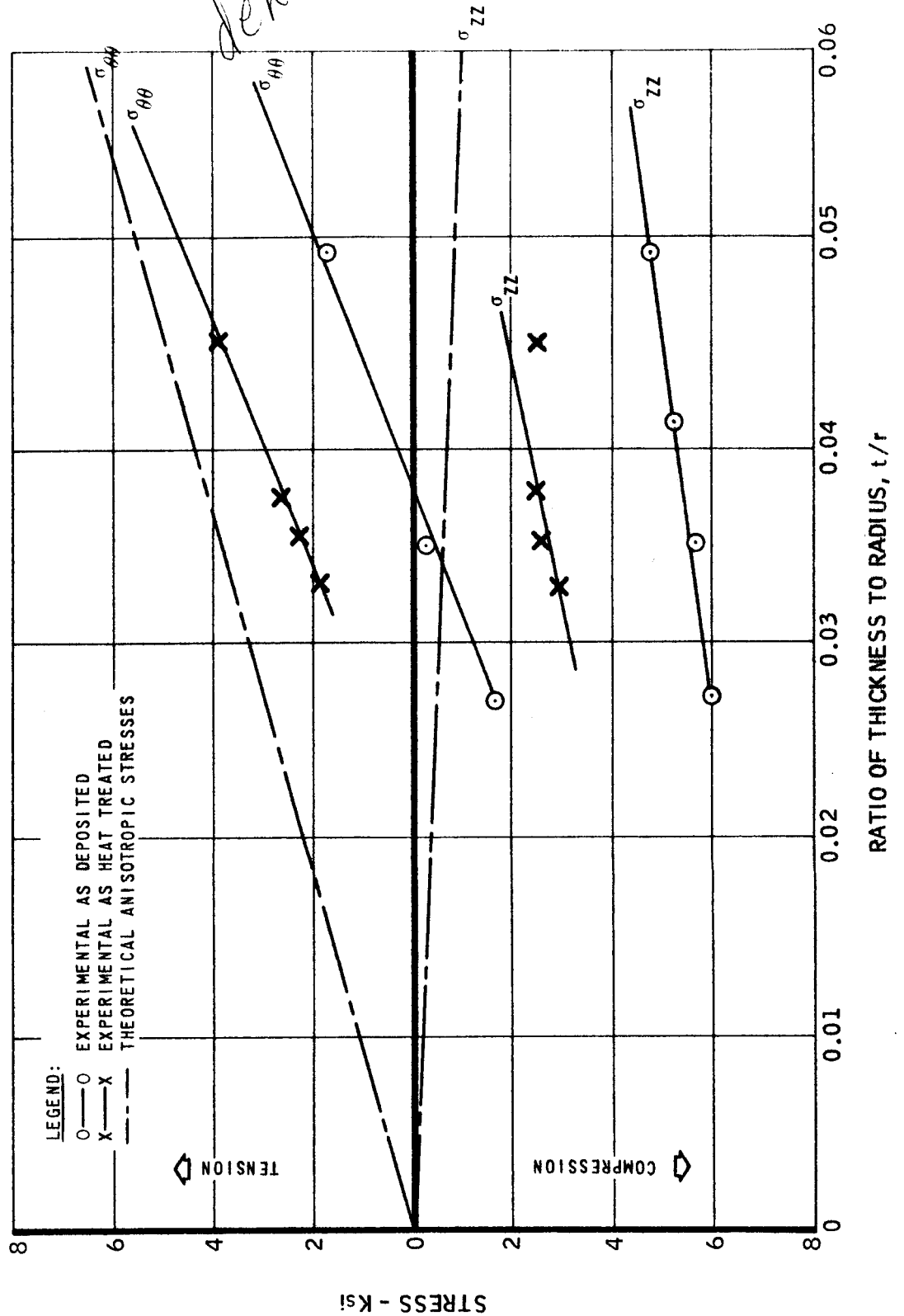
MAC A673

RESIDUAL STRESS ON OUTSIDE SURFACE
PYROLYTIC GRAPHITE CYLINDER

MAC A673

RESIDUAL STRESS ON MIDDLE a - b PLANE
PYROLYTIC GRAPHITE CYLINDER

LONGITUDINAL σ_{zz} AND TANGENTIAL $\sigma_{\theta\theta}$ STRESSES ON THE INSIDE SURFACE OF
PYROLYTIC GRAPHITE CYLINDERS AND CONES VS. THE RATIO OF THICKNESS TO RADIUS



LONGITUDINAL σ_{zz} AND TANGENTIAL $\sigma_{\theta\theta}$ STRESSES ON THE INSIDE SURFACE OF
PYROLYTIC GRAPHITE CYLINDERS AND CONES vs. THE RATIO OF THICKNESS TO RADIUS

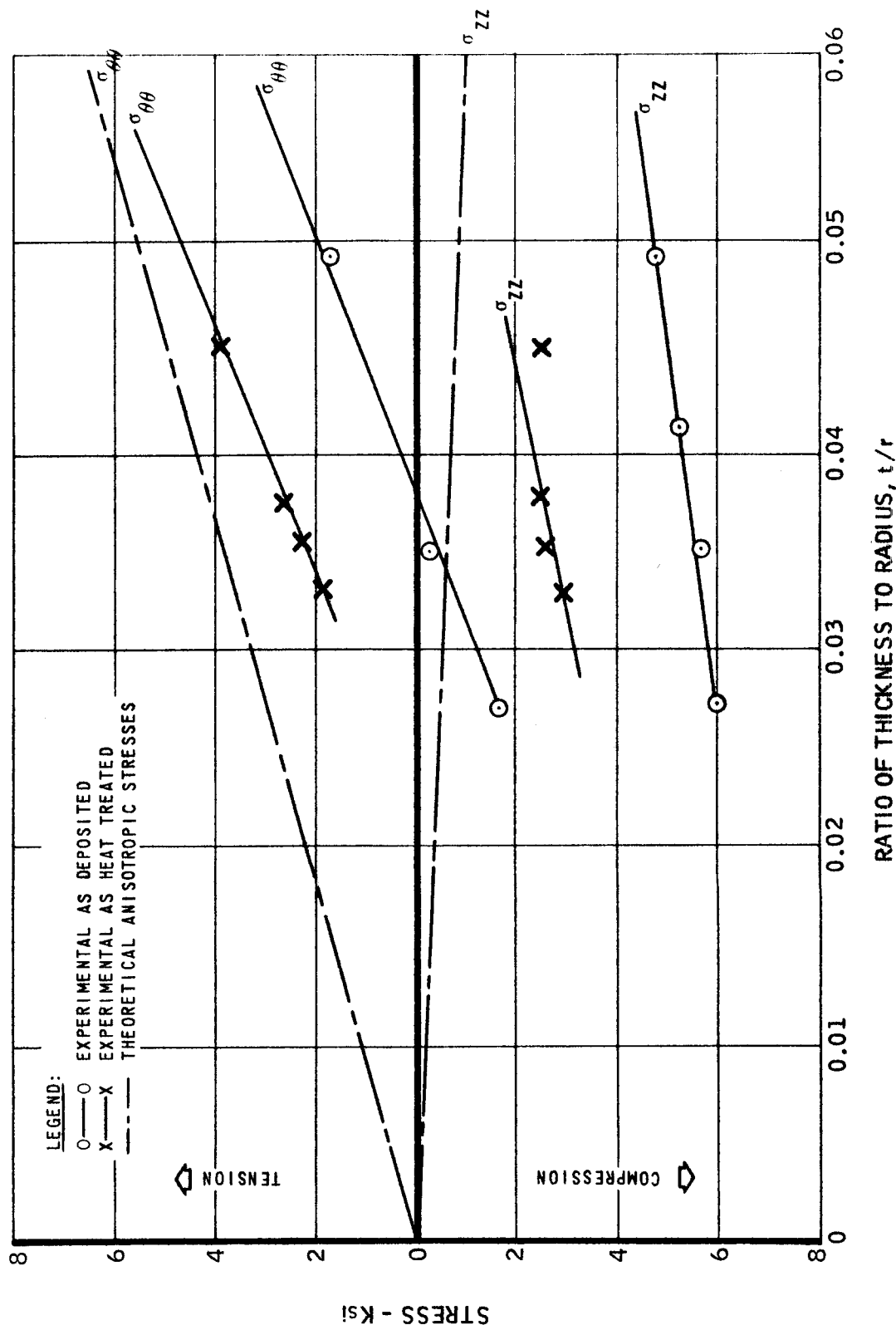
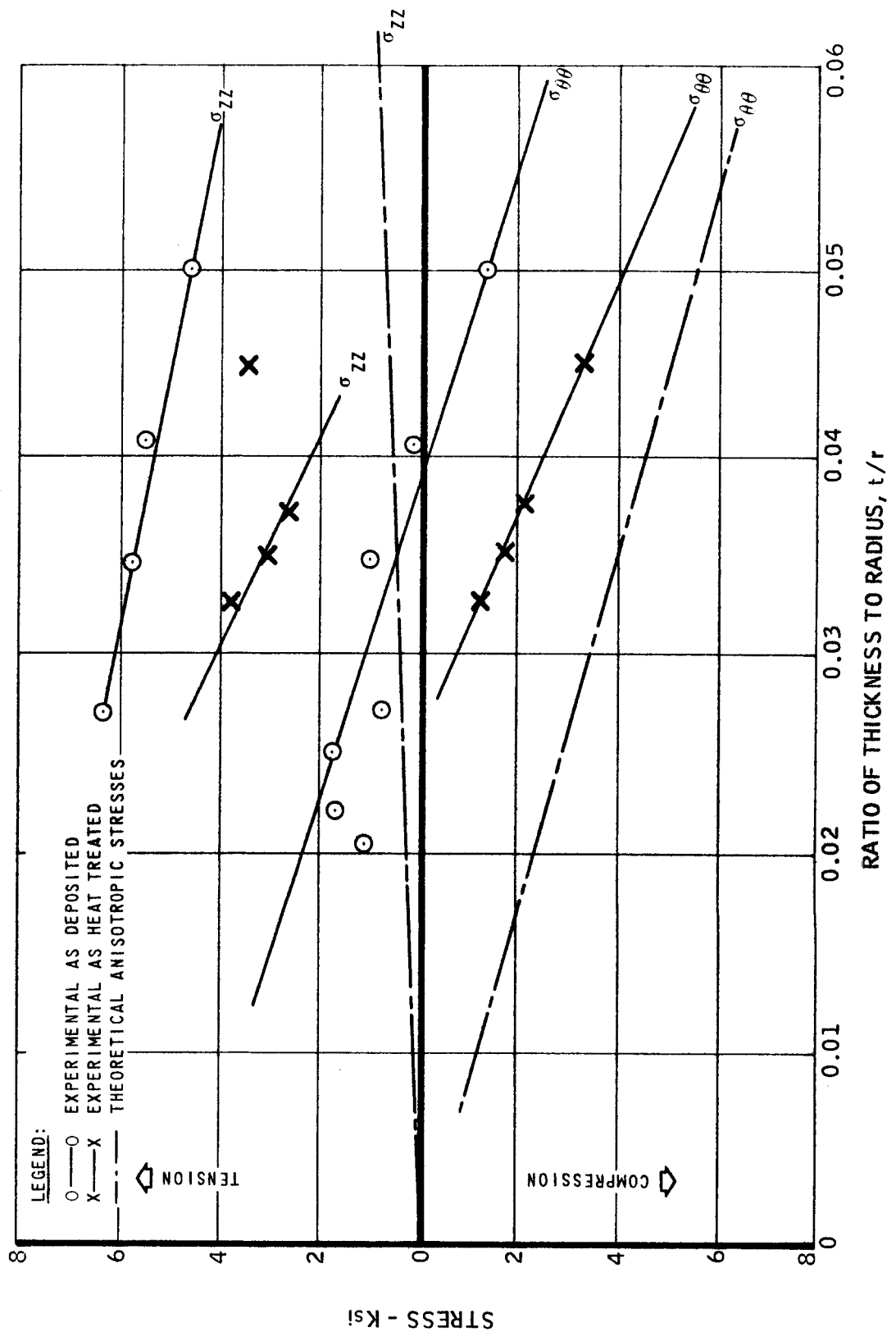


FIGURE 4

LONGITUDINAL σ_{zz} AND TANGENTIAL $\sigma_{\theta\theta}$ STRESSES ON THE OUTSIDE SURFACE OF
PYROLYTIC GRAPHITE CYLINDERS AND CONES VS. THE RATIO OF THICKNESS TO RADIUS



CIRCUMFERENTIAL GROWTH STRESS POST - DEPOSITION GROWTH

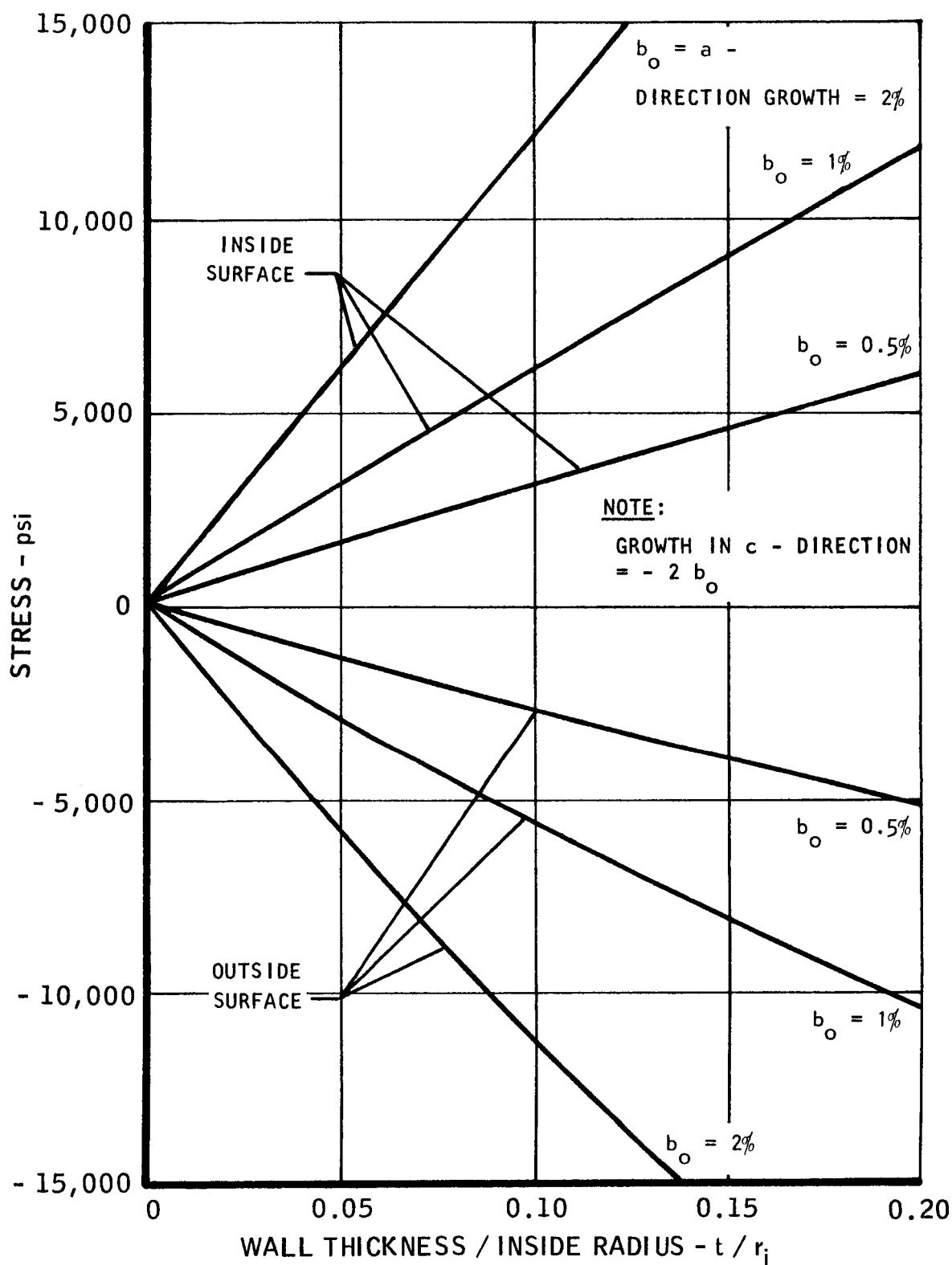
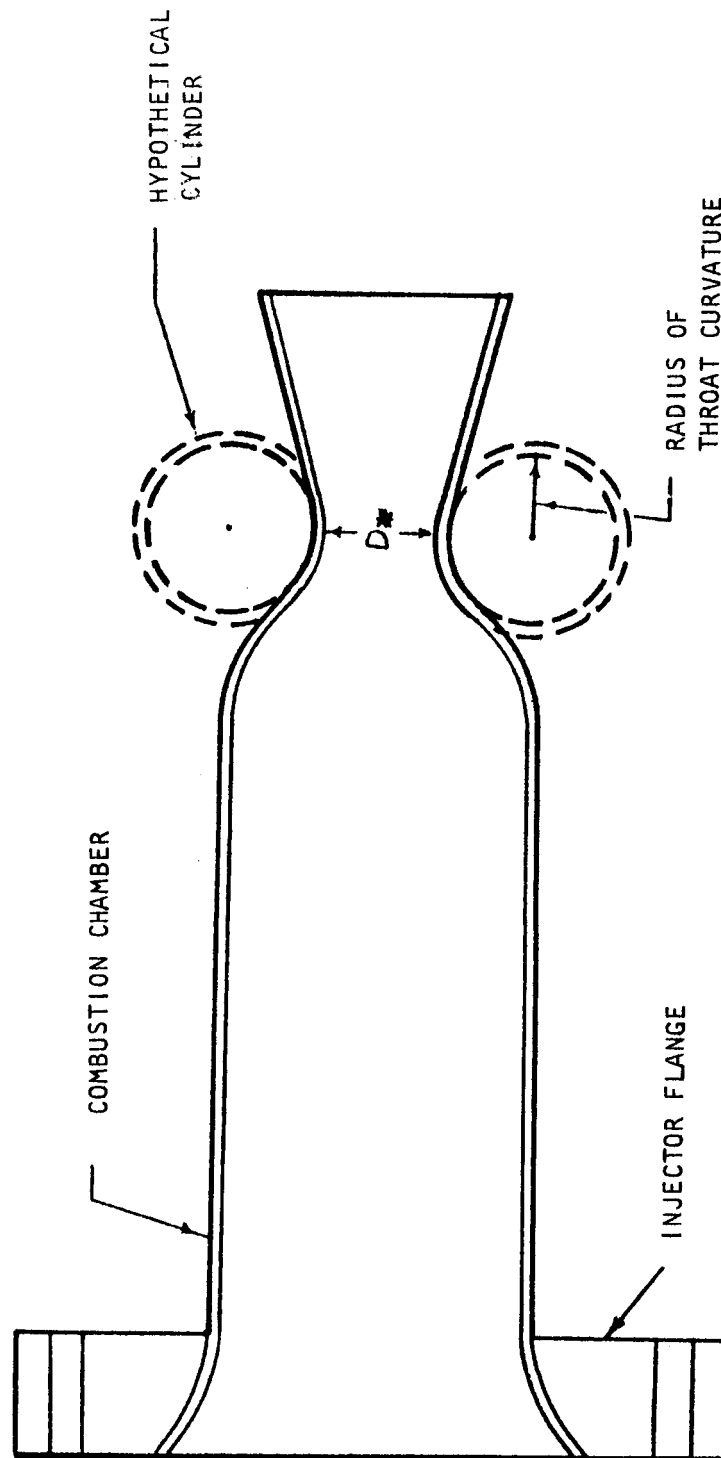


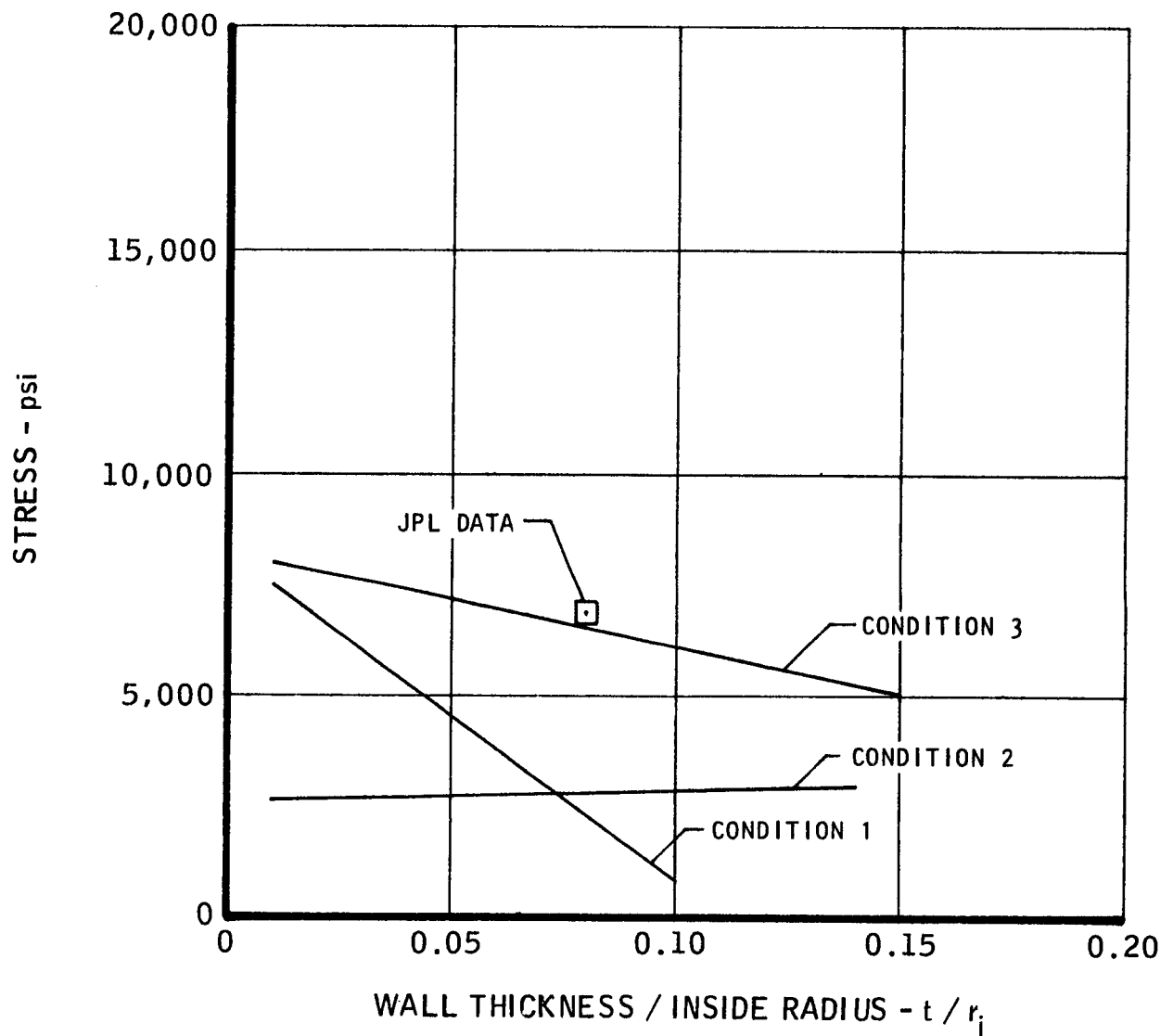
FIGURE 6

FREE STANDING PYROLYTIC GRAPHITE MOTOR

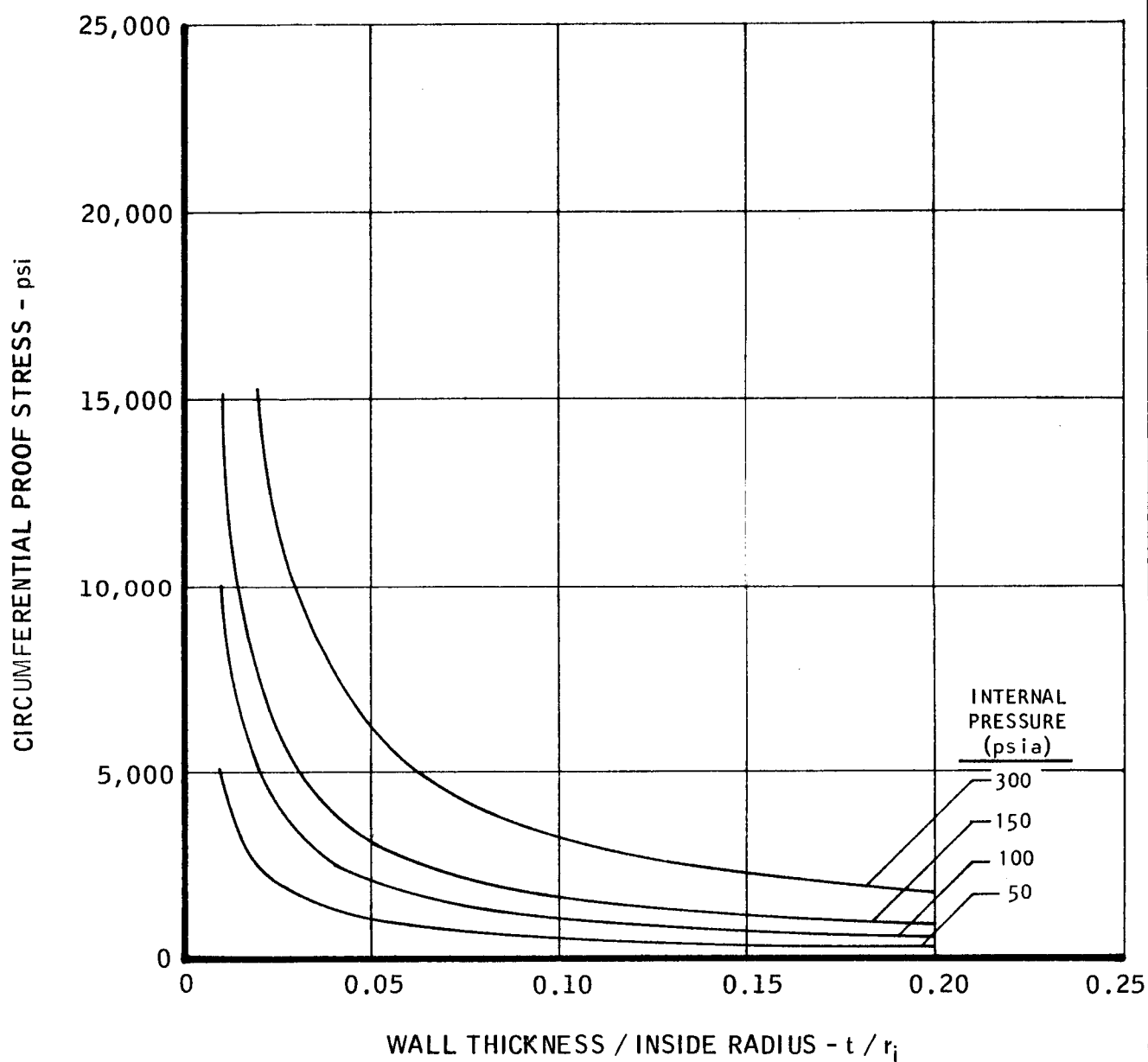


AXIAL RESIDUAL STRESS OUTSIDE SURFACE OF THROAT

RADIUS OF CURVATURE = THROAT DIAMETER

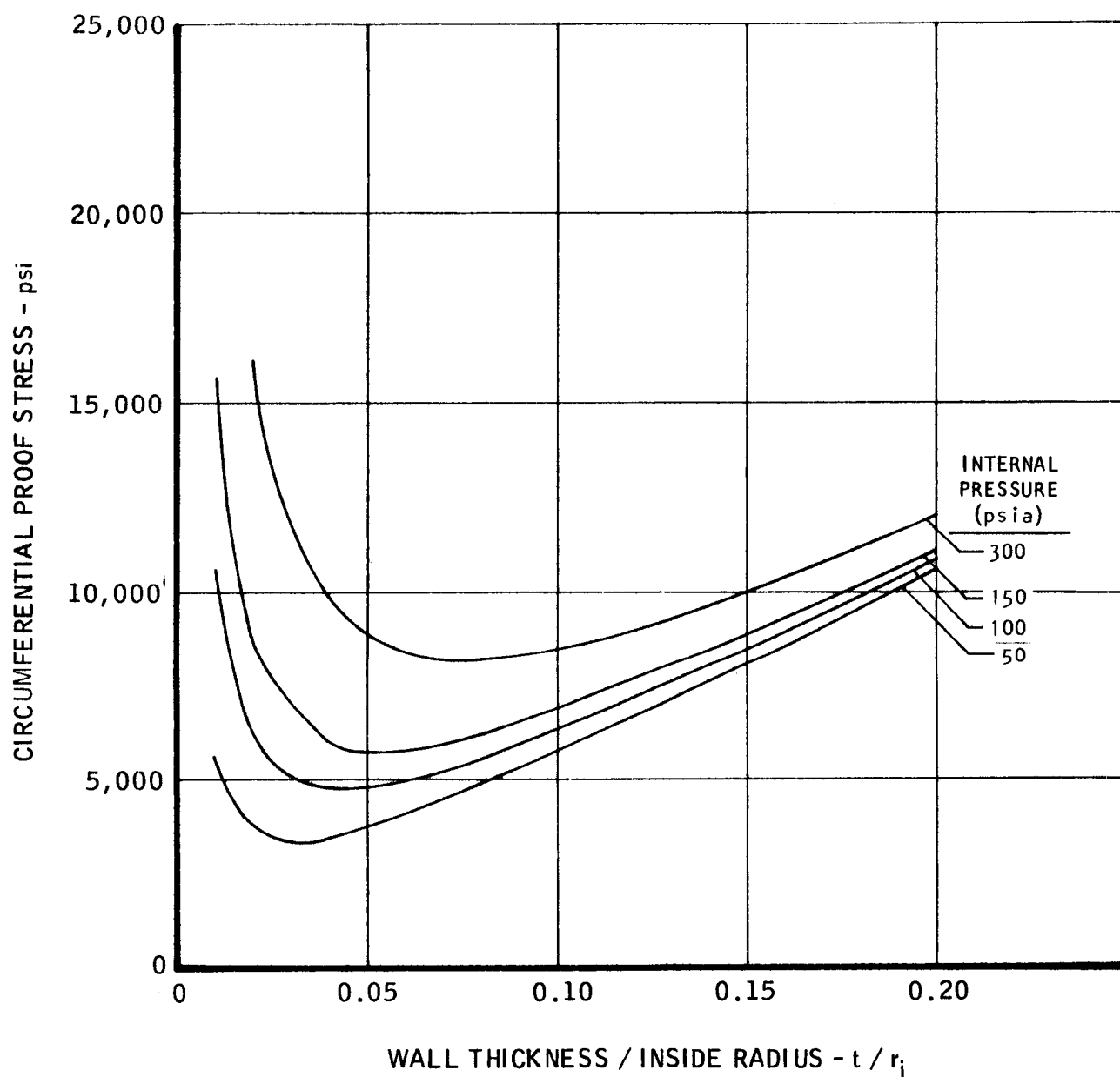


CIRCUMFERENTIAL PROOF STRESS
INSIDE SURFACE OF COMBUSTION CHAMBER
STRESS FREE TEMPERATURE = 0°F



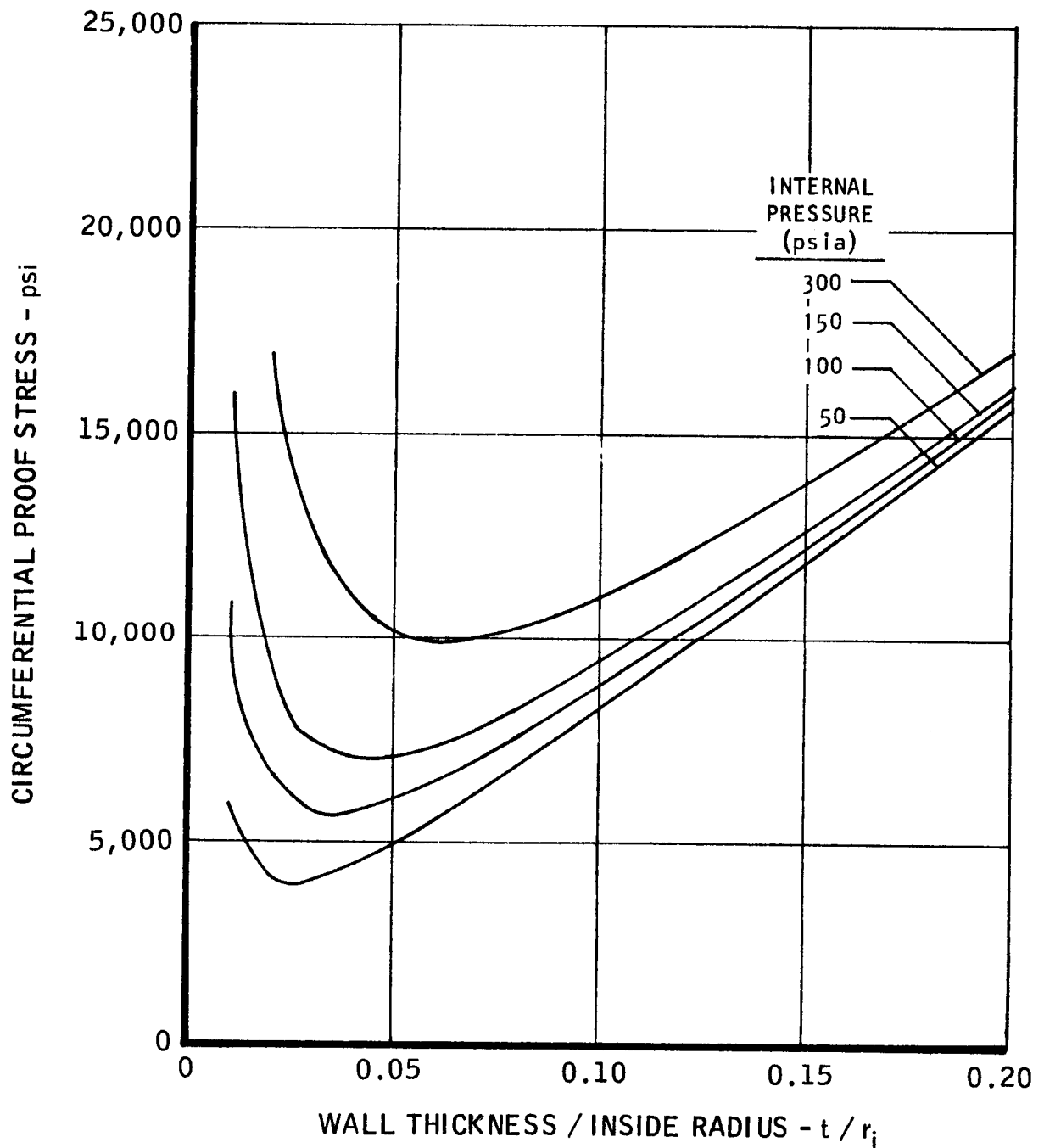
CIRCUMFERENTIAL PROOF STRESS
INSIDE SURFACE OF COMBUSTION CHAMBER

STRESS FREE TEMPERATURE = 2000°F



CIRCUMFERENTIAL PROOF STRESS
INSIDE SURFACE OF COMBUSTION CHAMBER

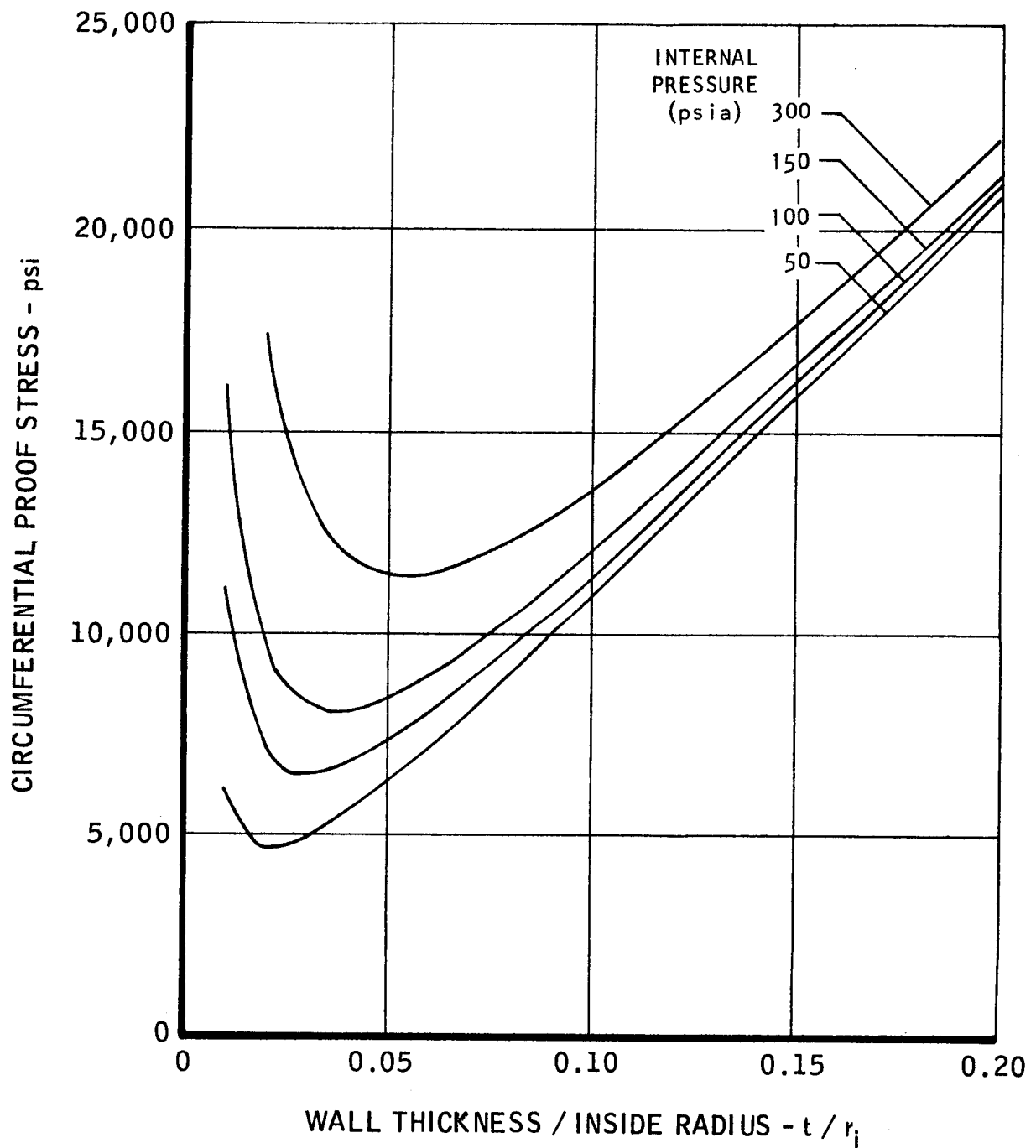
STRESS FREE TEMPERATURE = 3000°F



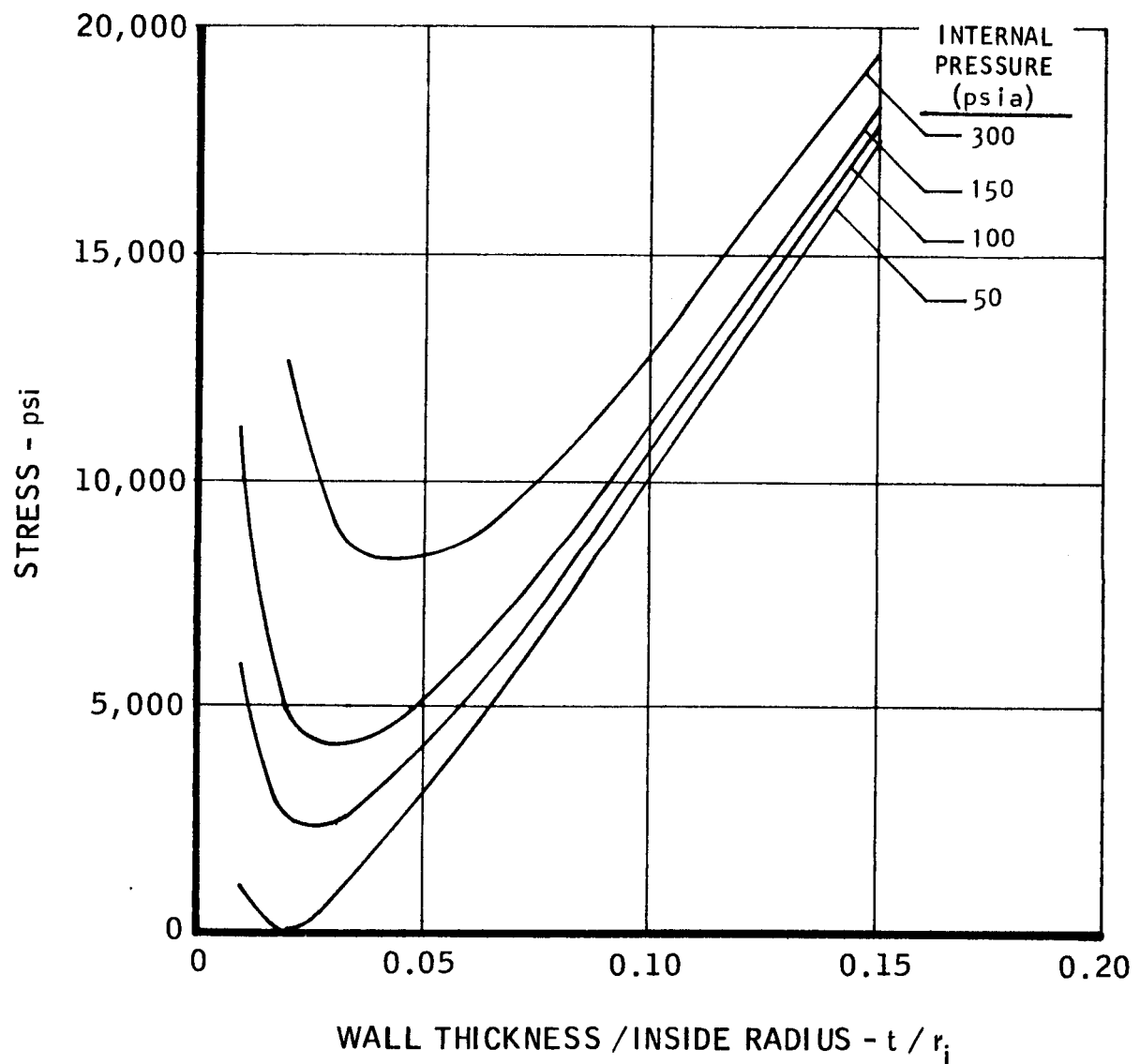
MAC A679

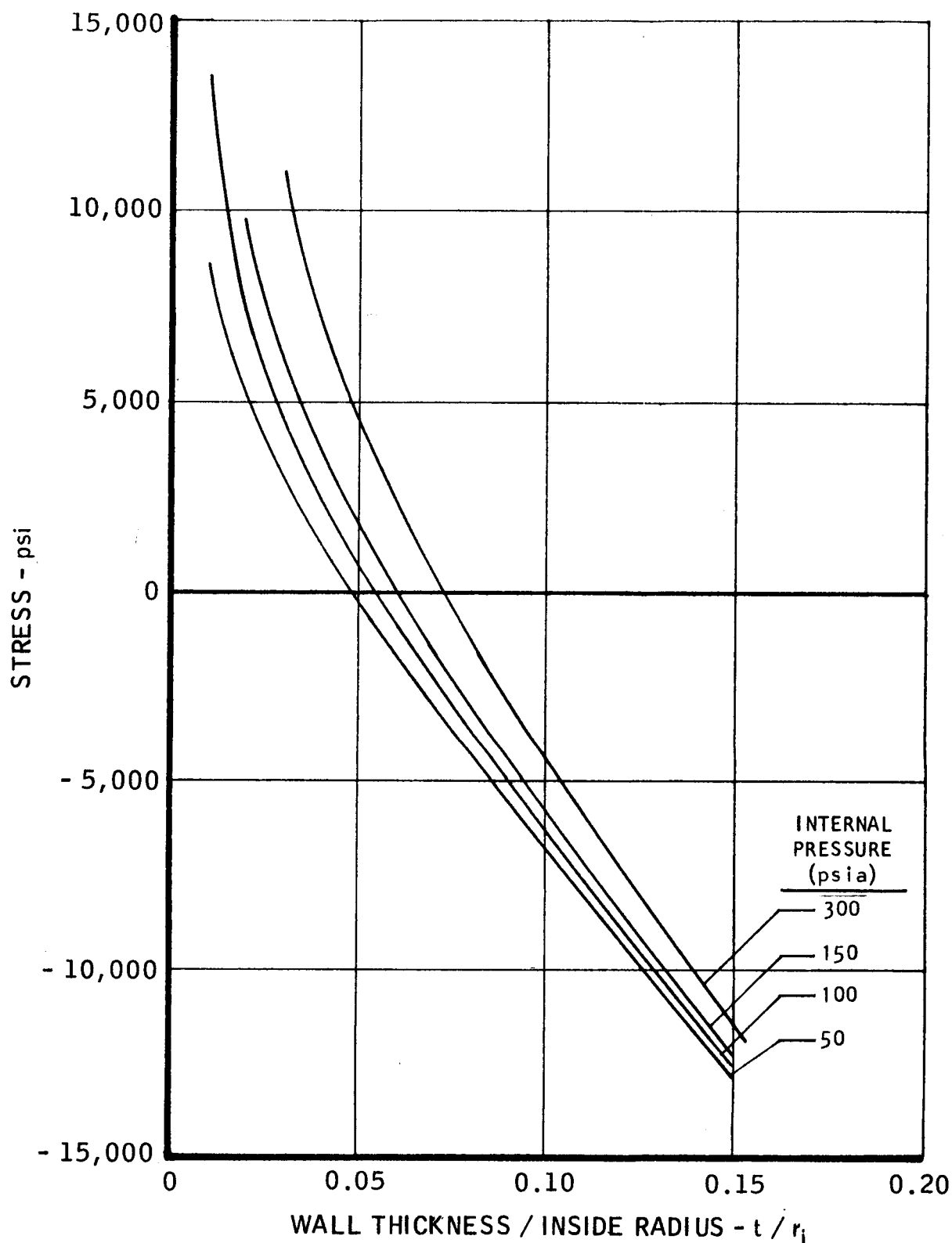
CIRCUMFERENTIAL PROOF STRESS
INSIDE SURFACE OF COMBUSTION CHAMBER

STRESS FREE TEMPERATURE = 4000 °F



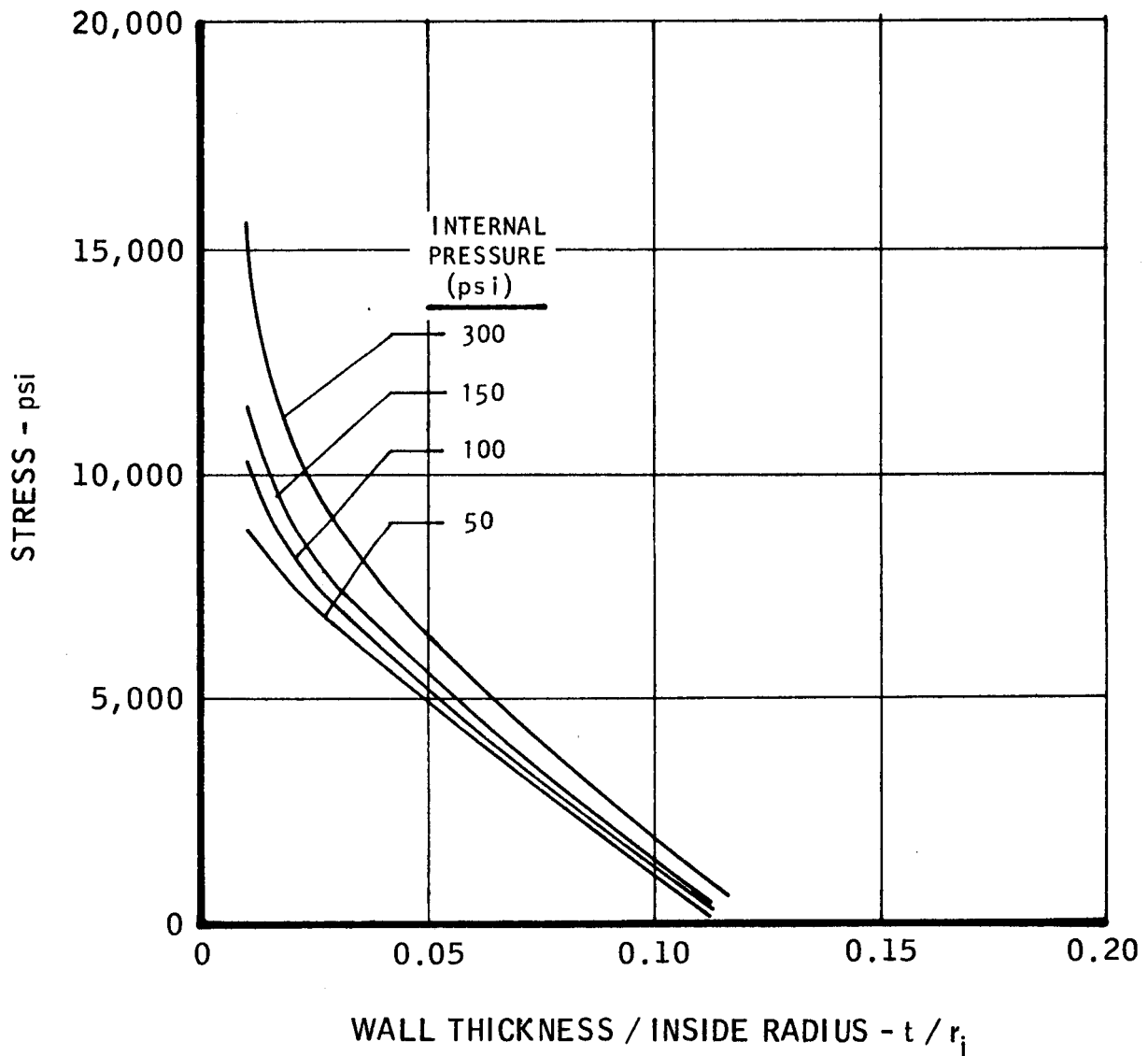
CIRCUMFERENTIAL PROOF STRESS
INSIDE SURFACE OF COMBUSTION CHAMBER
FOR AS - DEPOSITED MATERIAL

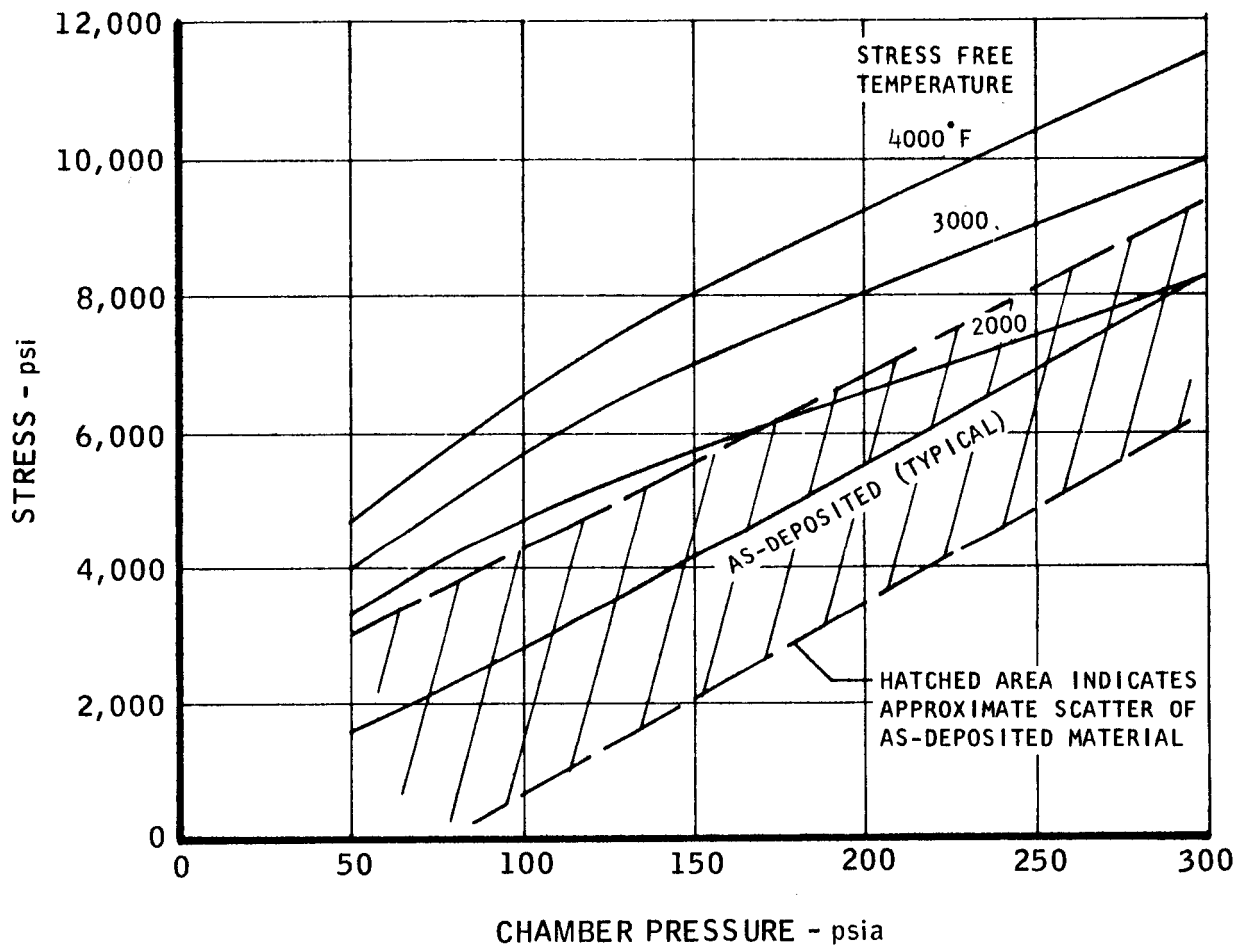


CIRCUMFERENTIAL PROOF STRESS
OUTSIDE SURFACE OF COMBUSTION CHAMBER
FOR AS - DEPOSITED MATERIAL

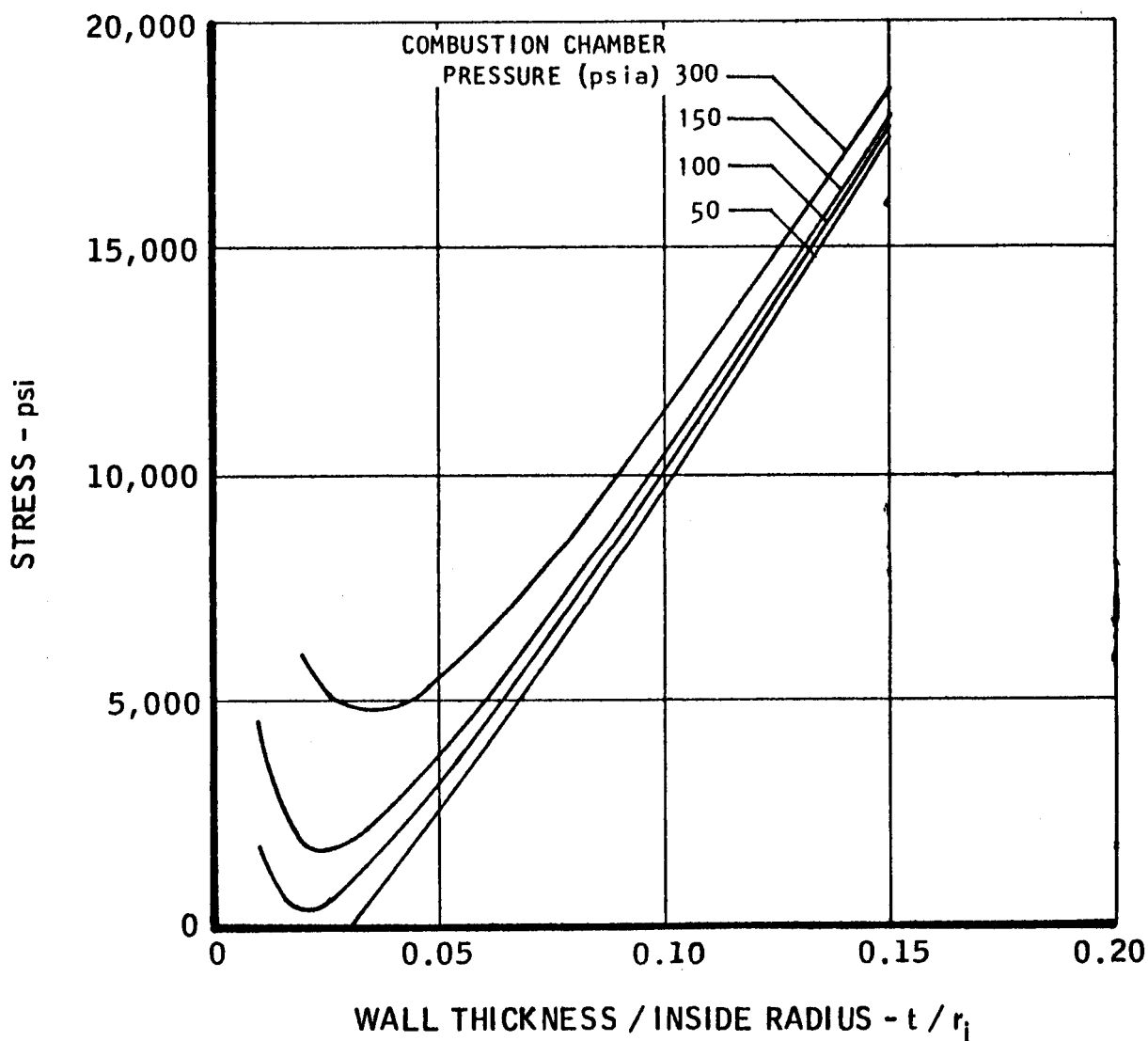
MAC A673

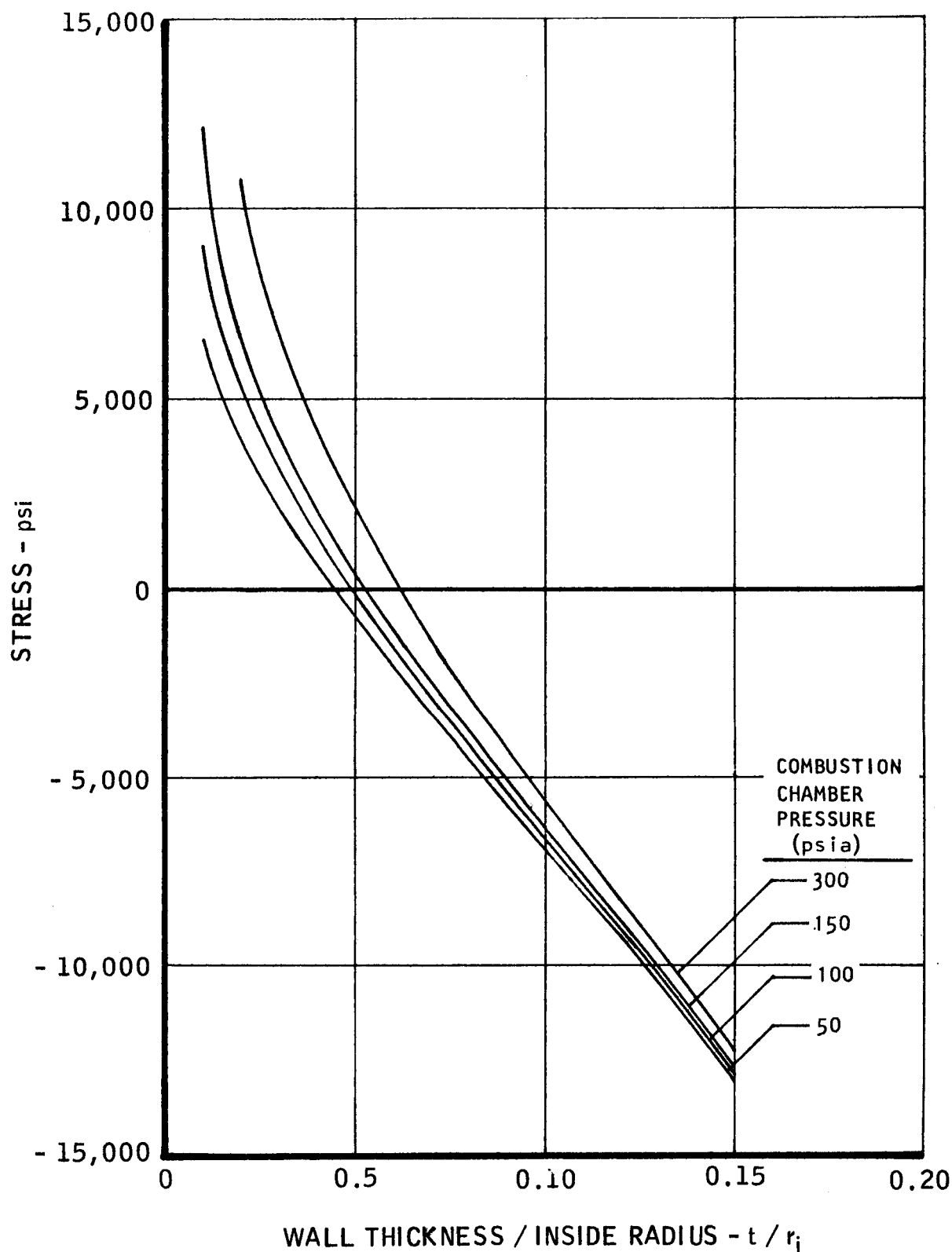
AXIAL PROOF STRESS
OUTSIDE SURFACE OF COMBUSTION CHAMBER
FOR AS - DEPOSITED MATERIAL



CIRCUMFERENTIAL PROOF STRESS
OPTIMUM THICKNESS / RADIUS RATIO
COMBUSTION CHAMBER

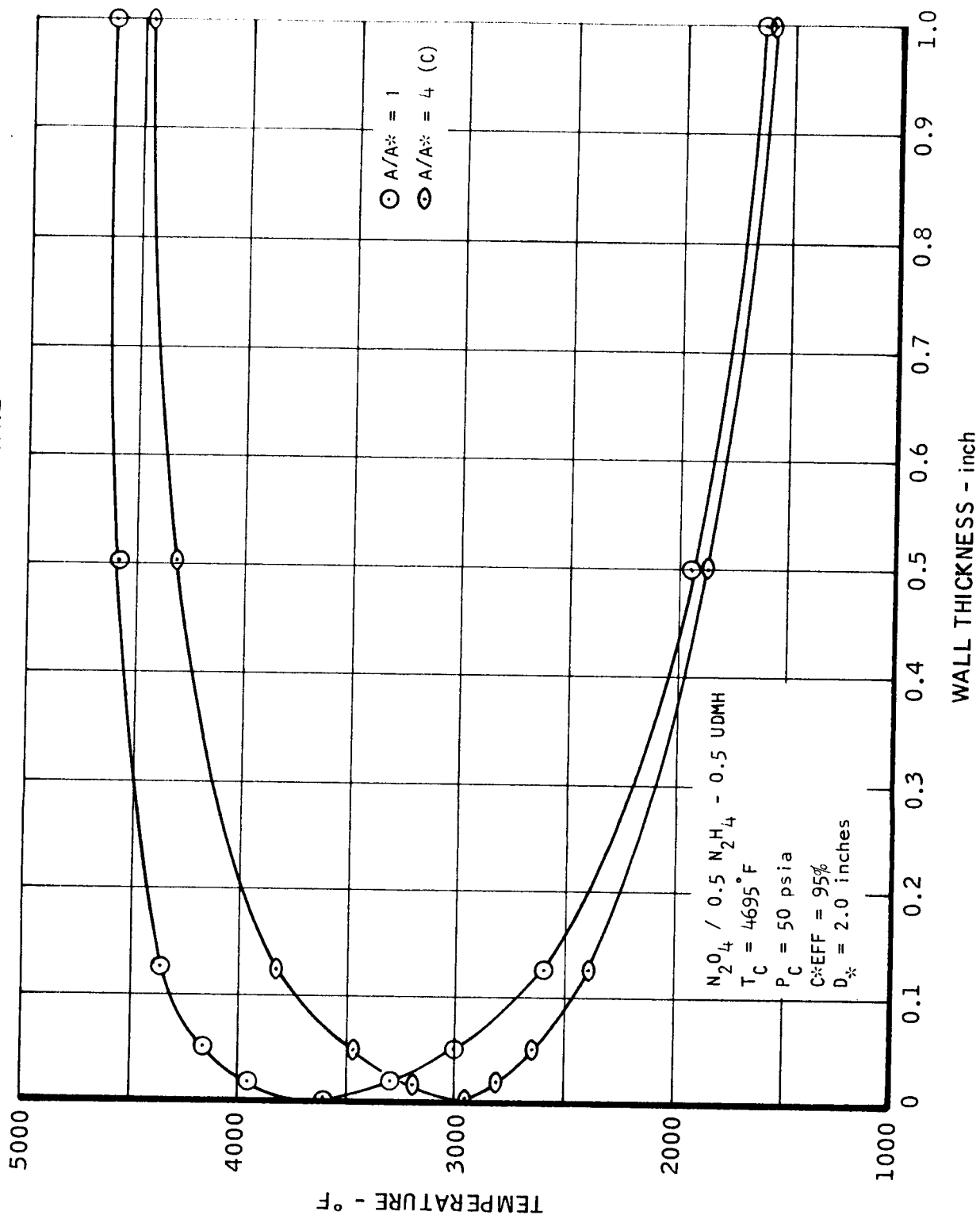
CIRCUMFERENTIAL PROOF STRESS
INSIDE SURFACE OF THROAT
FOR AS - DEPOSITED MATERIAL



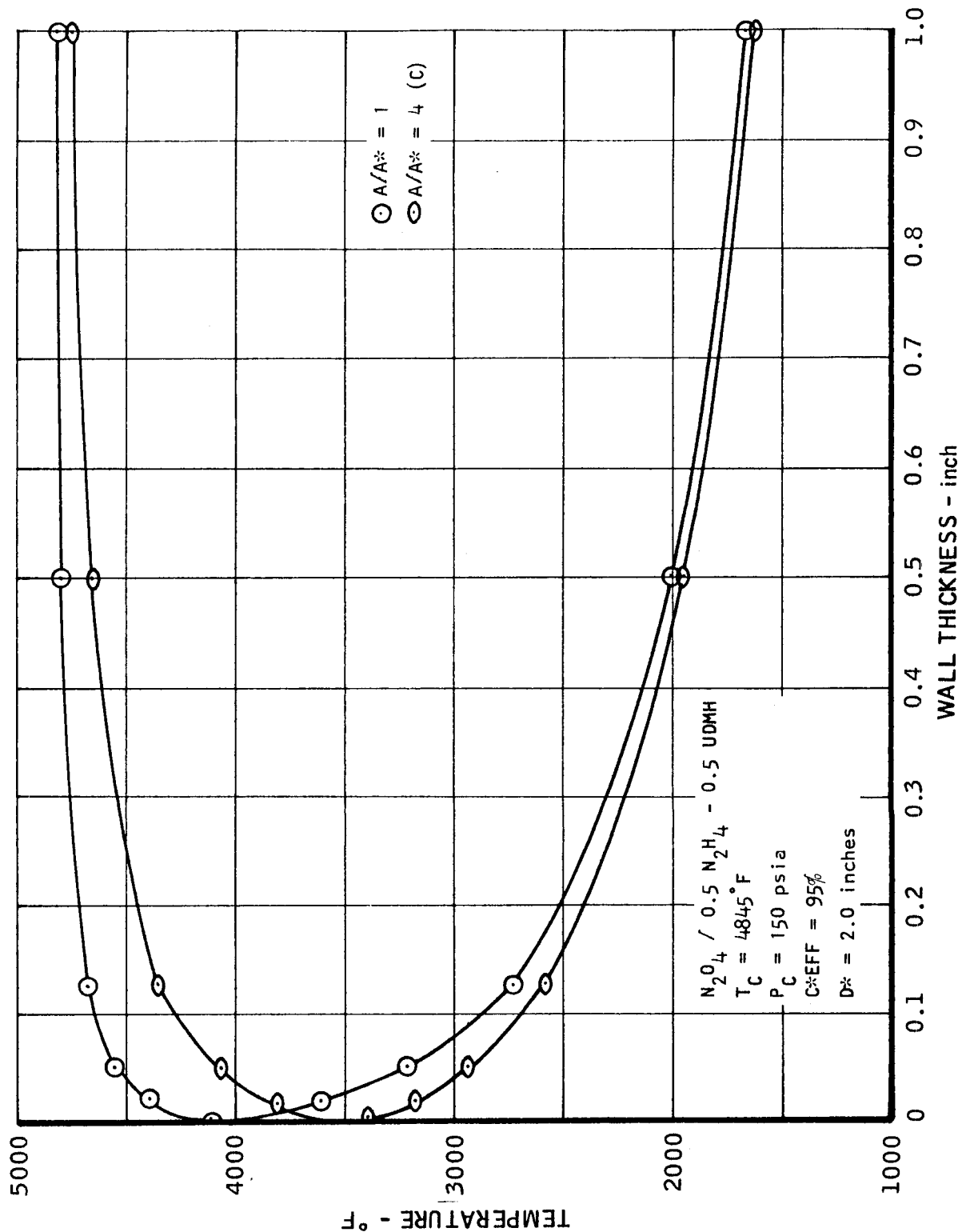
CIRCUMFERENTIAL PROOF STRESS
OUTSIDE SURFACE OF THROAT
FOR AS - DEPOSITED MATERIAL

MAC A673

PYROLYTIC GRAPHITE MOTOR WALL TEMPERATURES
RADIATION COOLED - STEADY STATE

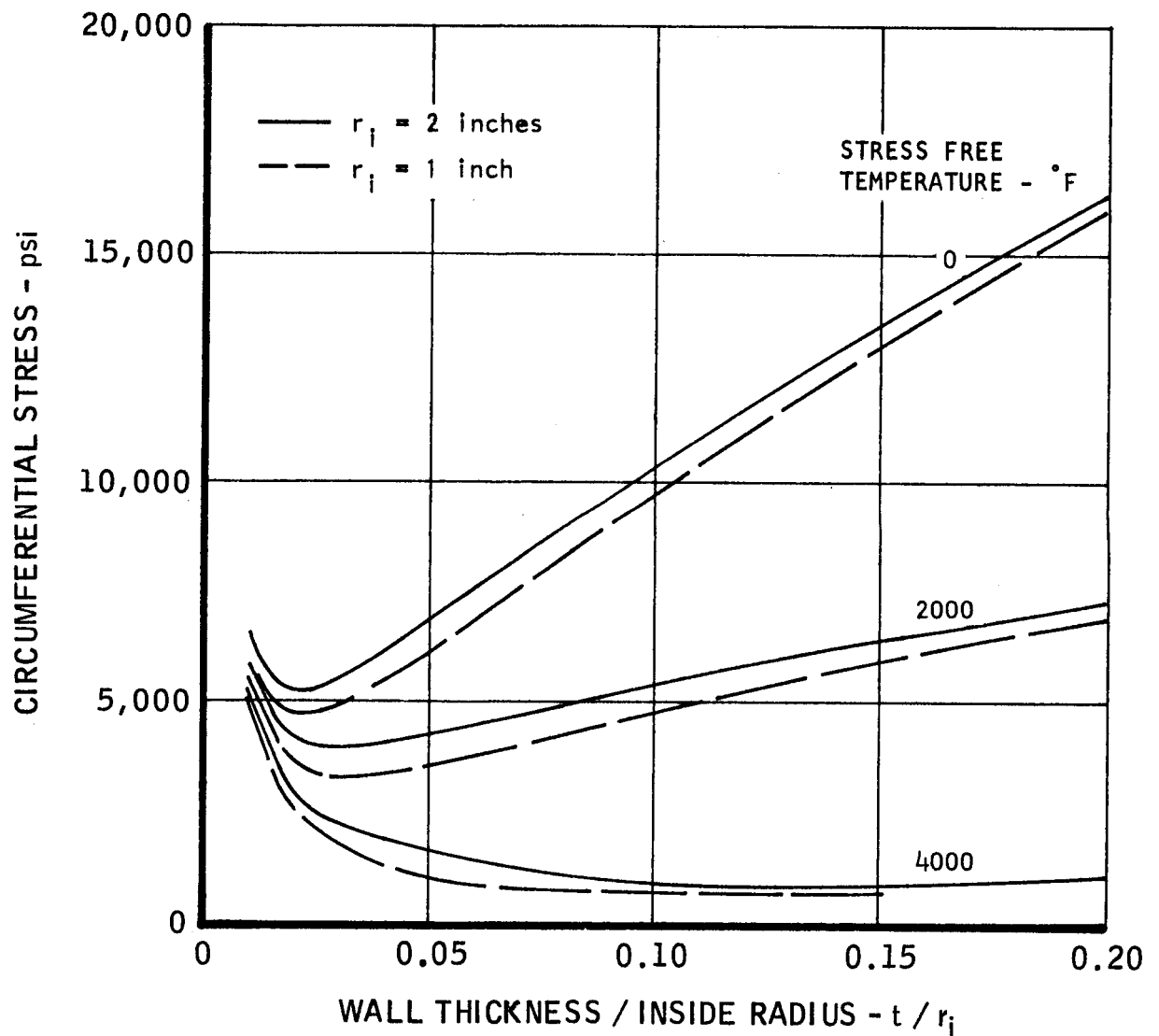


PYROLYTIC GRAPHITE MOTOR WALL TEMPERATURES
RADIATION COOLED - STEADY STATE



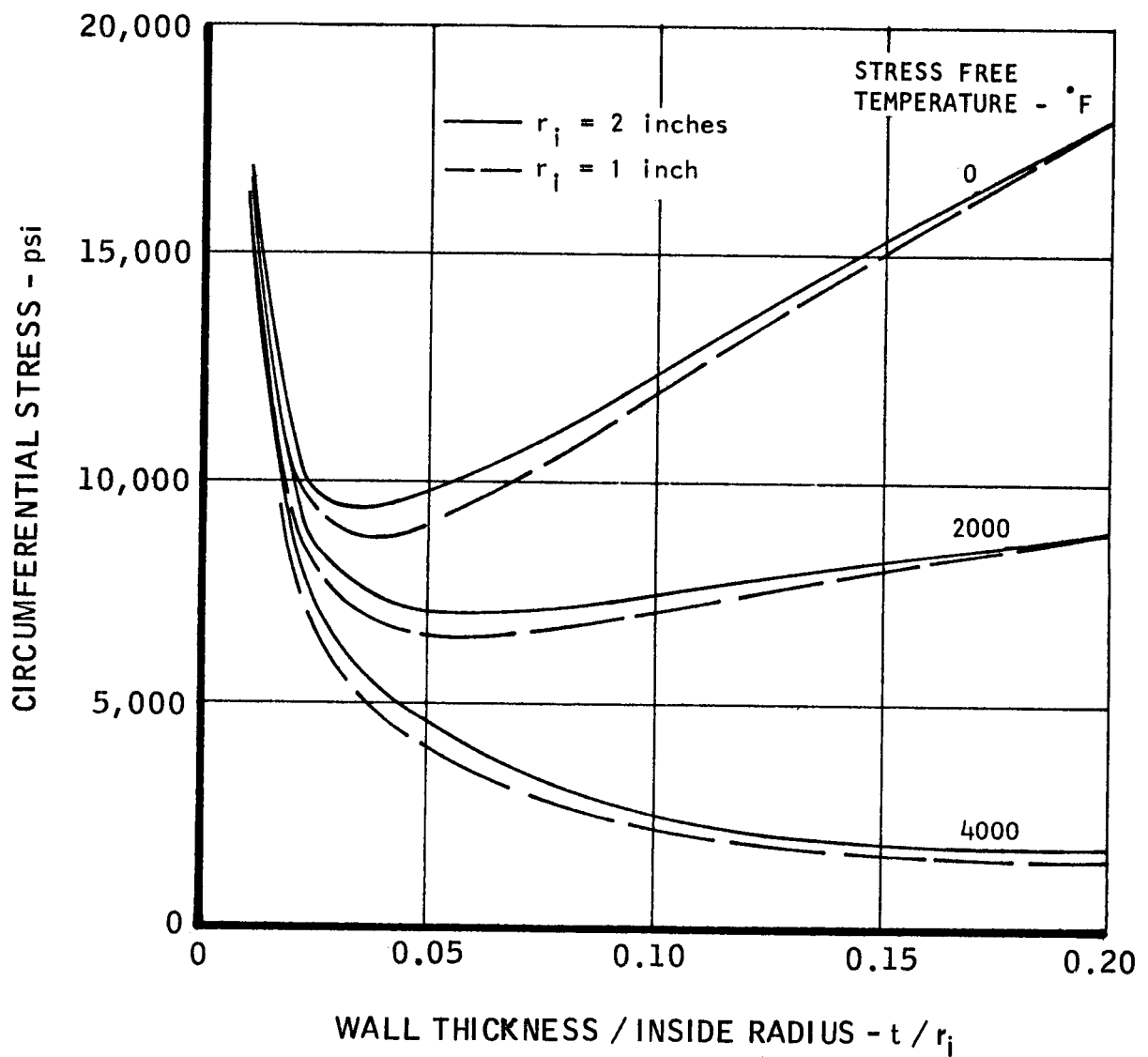
CIRCUMFERENTIAL OPERATING STRESS
COMBUSTION CHAMBER

$$P_c = 50 \text{ psia}$$



CIRCUMFERENTIAL OPERATING STRESS
COMBUSTION CHAMBER

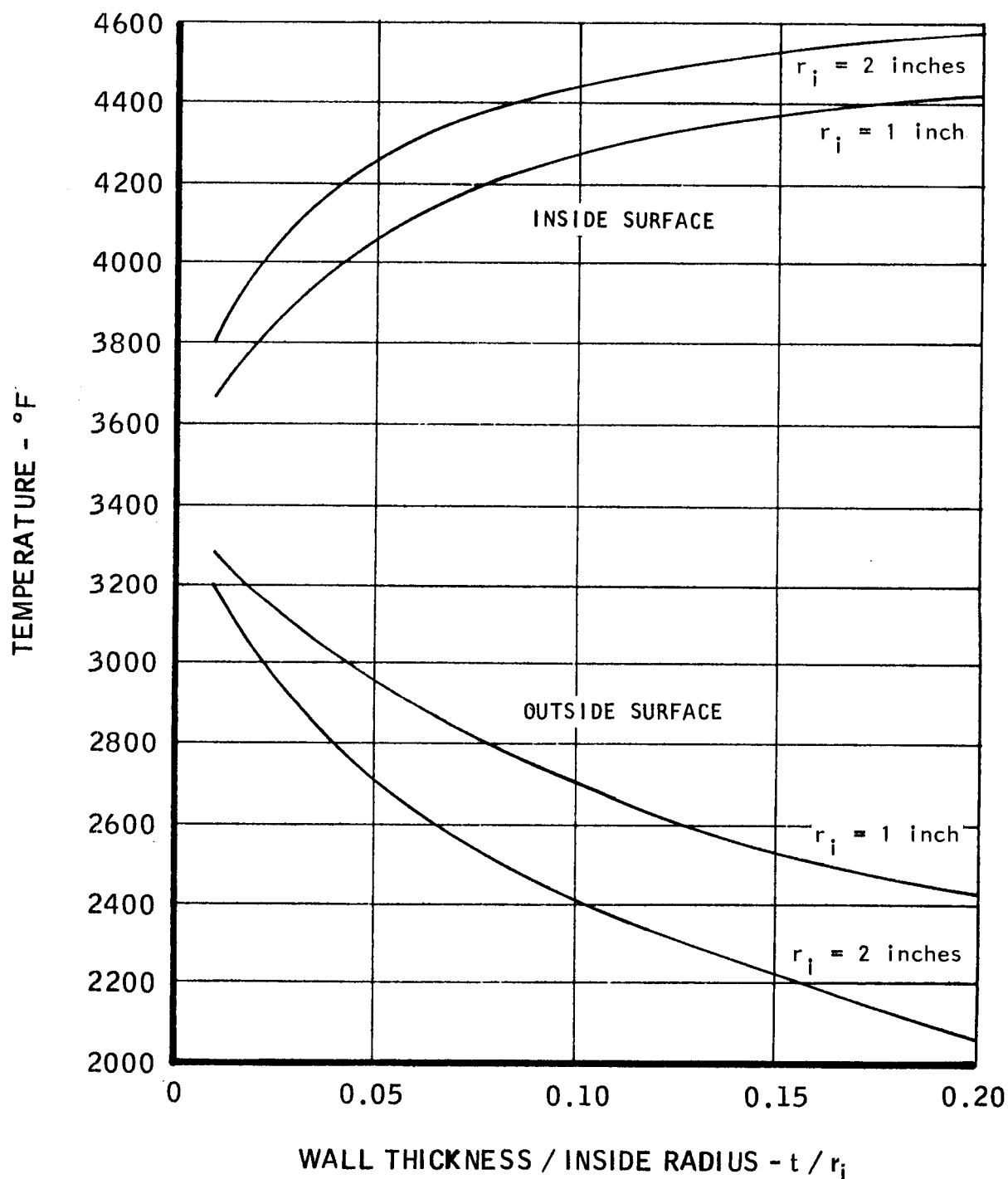
$$P_c = 150 \text{ psia}$$



MAC A673

PYROLYTIC GRAPHITE MOTOR WALL TEMPERATURE
COMBUSTION CHAMBER ($\epsilon_c = 4$)

$$P_c = 150 \text{ psia}$$

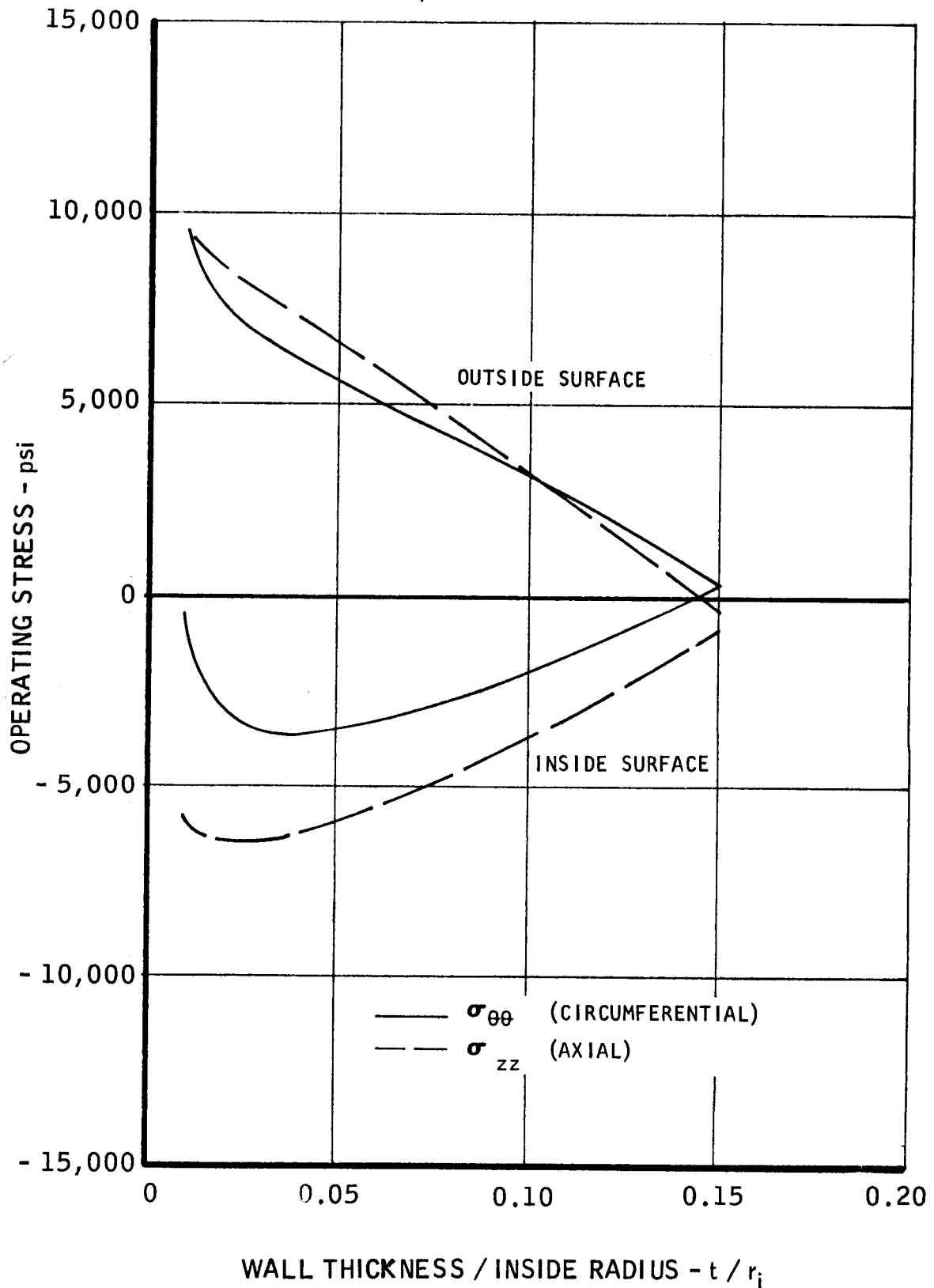


COMBUSTION CHAMBER OPERATING STRESS
FOR AS - DEPOSITED MATERIAL

$$P_c = 50 \text{ psia}$$

 c

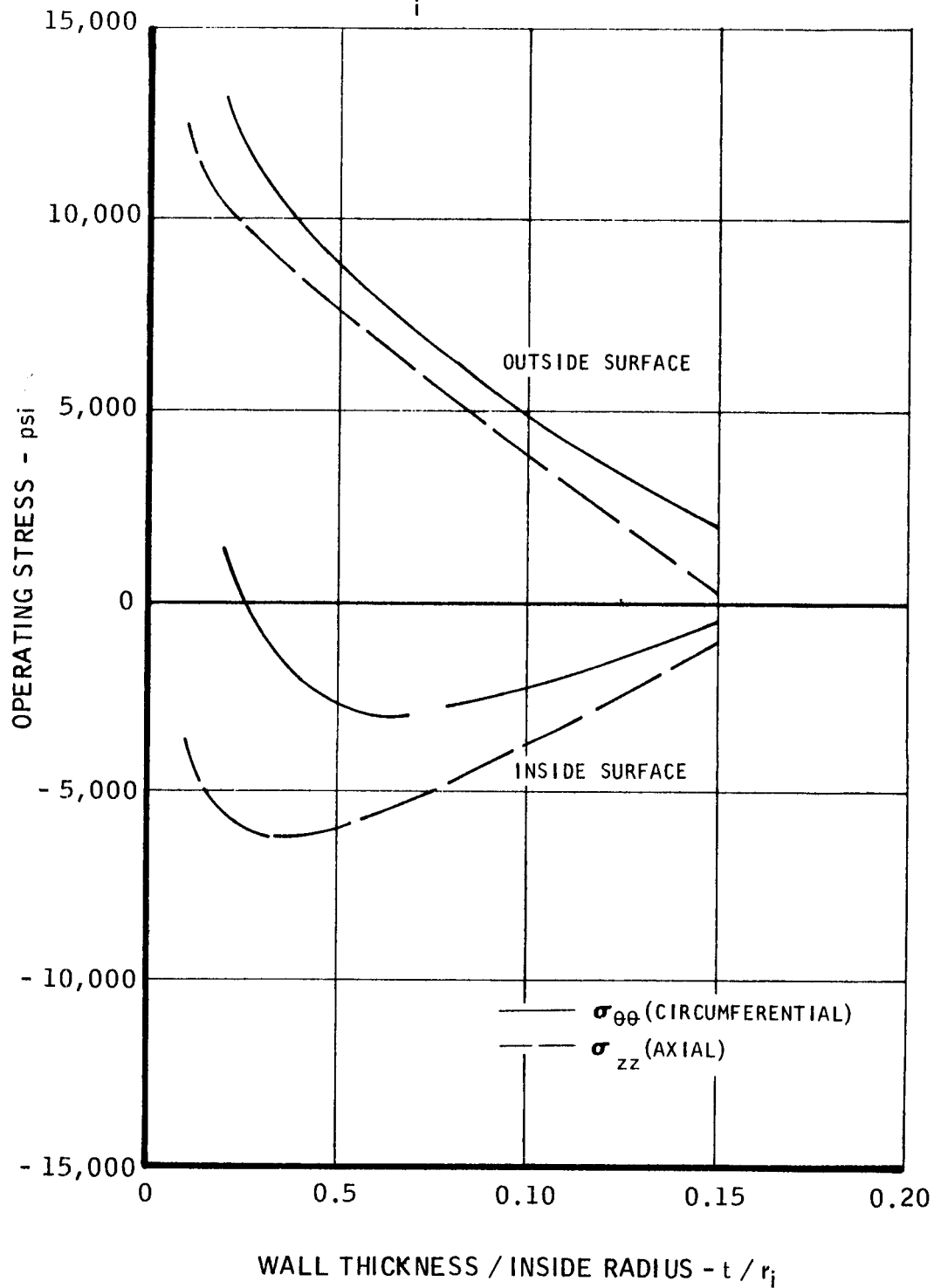
$$r_i = 2 \text{ inches}$$



COMBUSTION CHAMBER OPERATING STRESS
FOR AS - DEPOSITED MATERIAL

$$P_c = 150 \text{ psia}$$

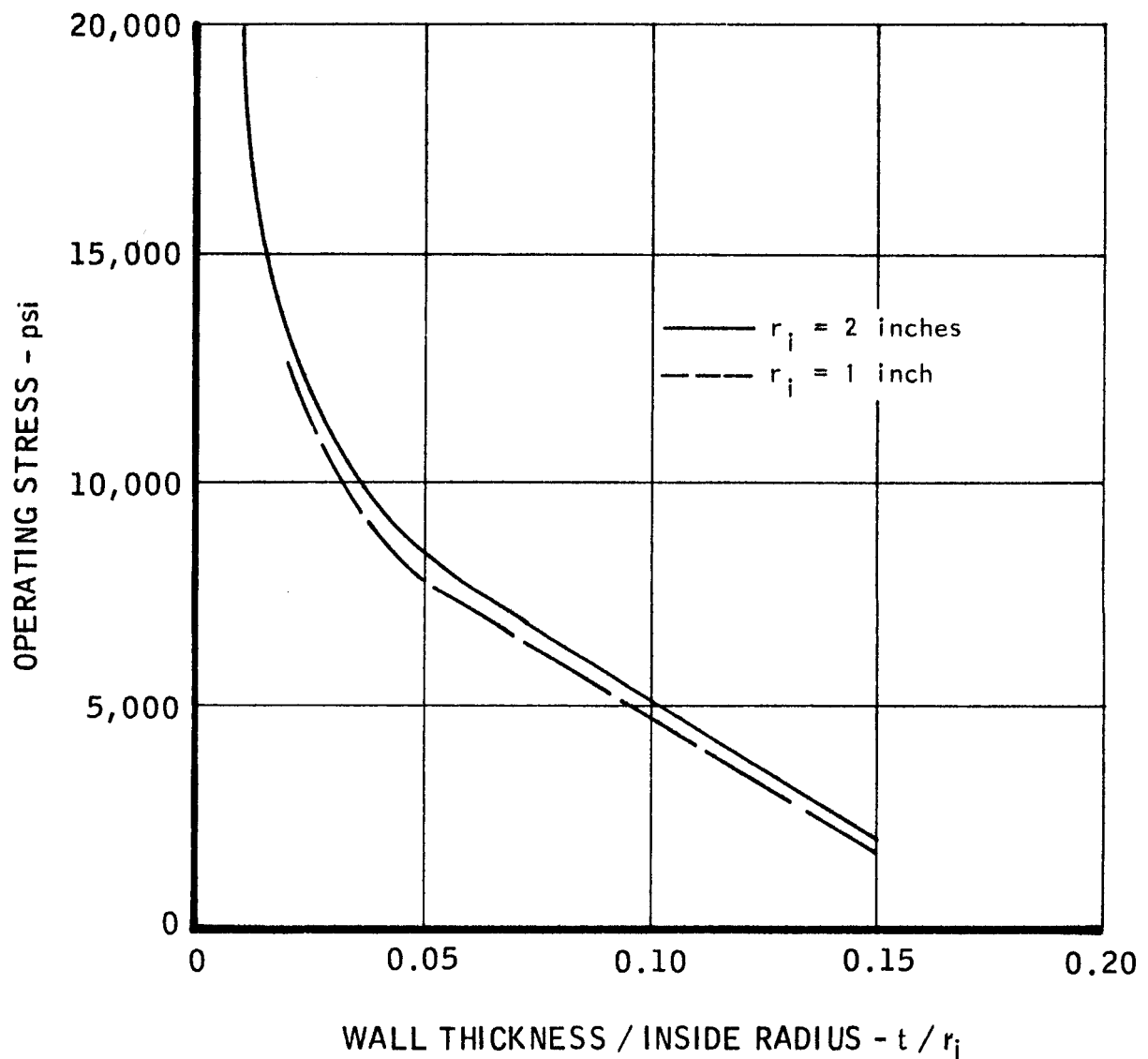
$$r_i = 2 \text{ inches}$$



COMBUSTION CHAMBER CIRCUMFERENTIAL OPERATING STRESS
FOR AS - DEPOSITED MATERIAL

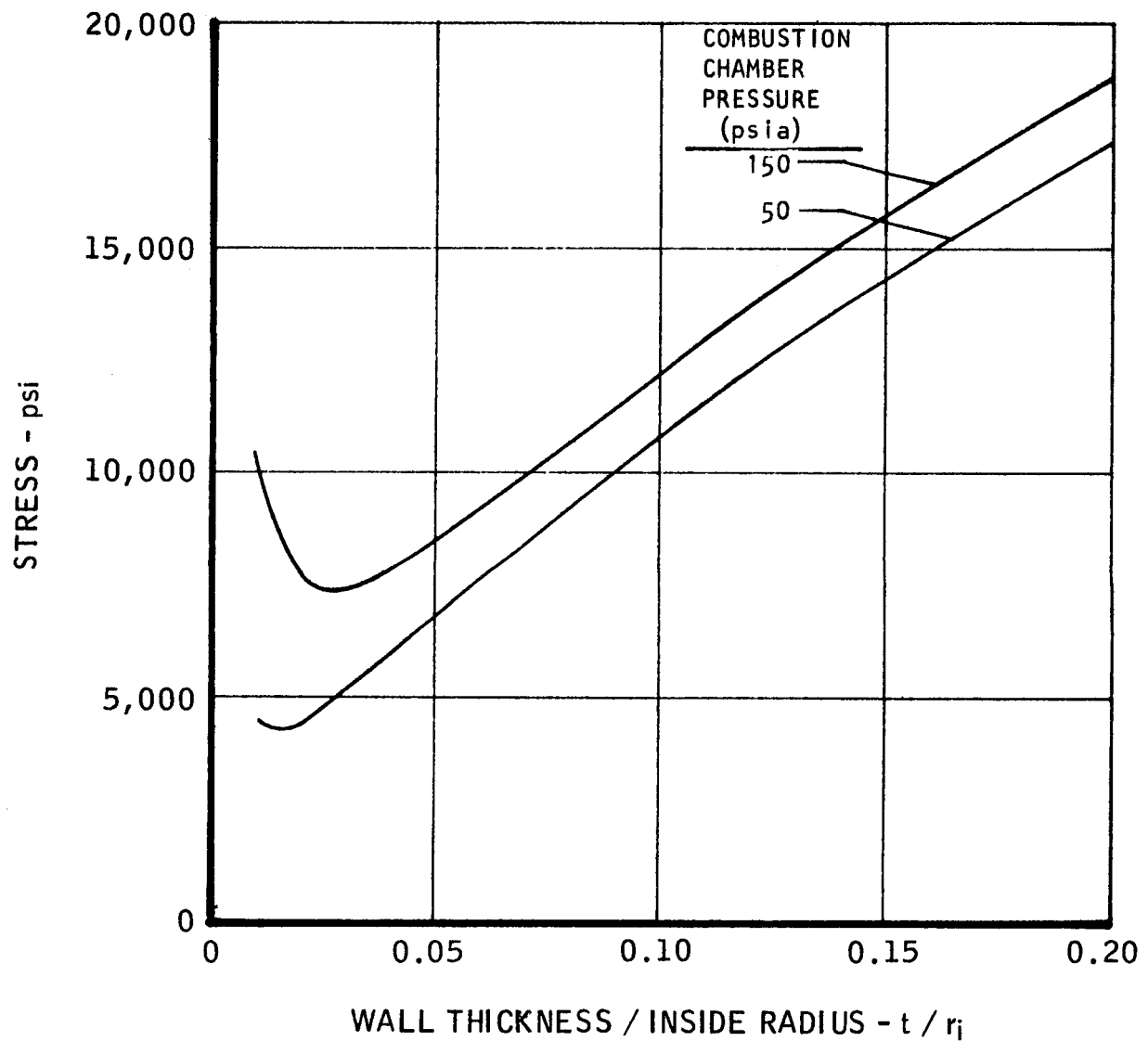
$$P_c = 150 \text{ psia}$$

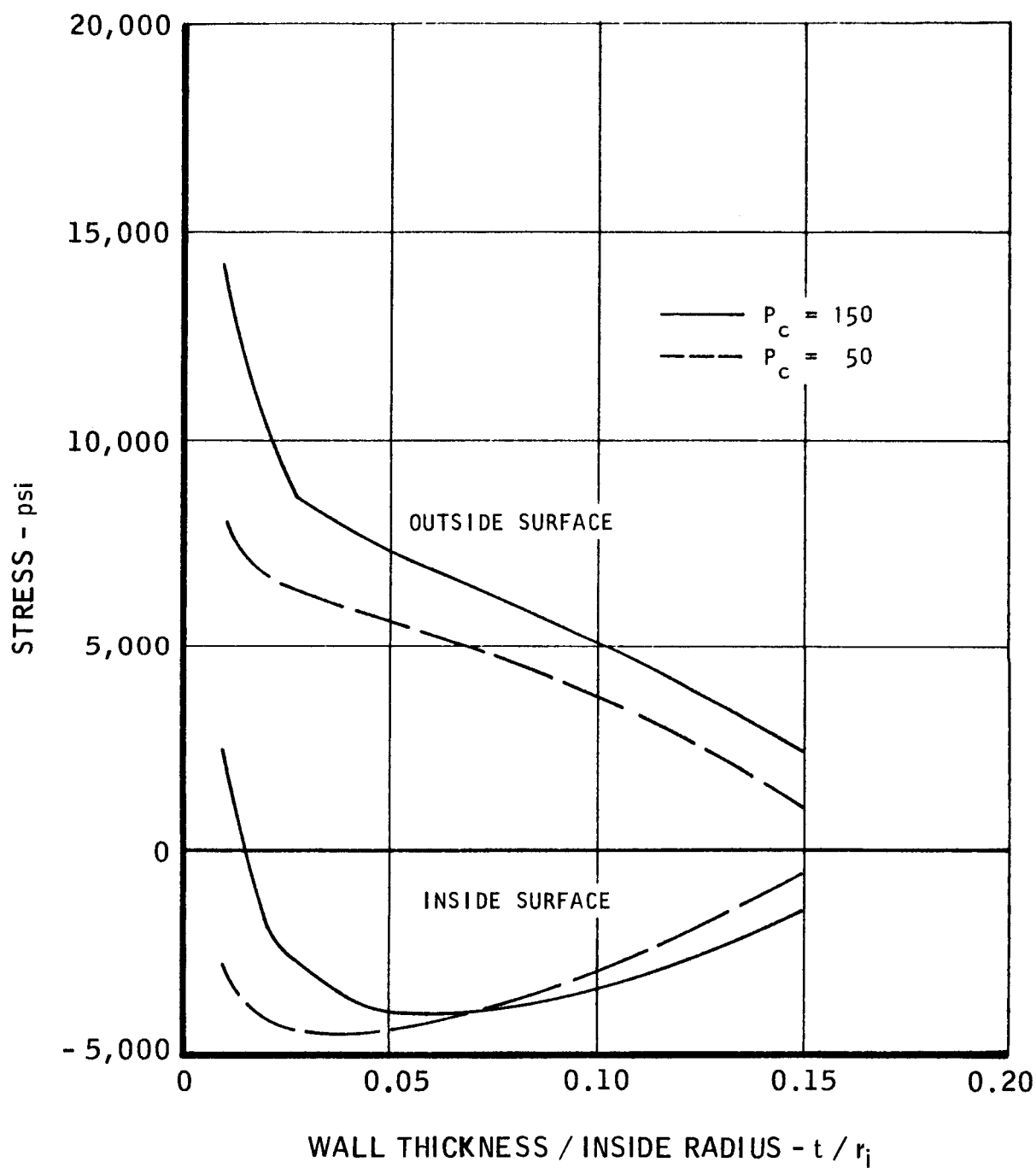
OUTSIDE SURFACE



CIRCUMFERENTIAL OPERATING STRESS
THROAT
OUTSIDE SURFACE

STRESS FREE TEMPERATURE = 0°F

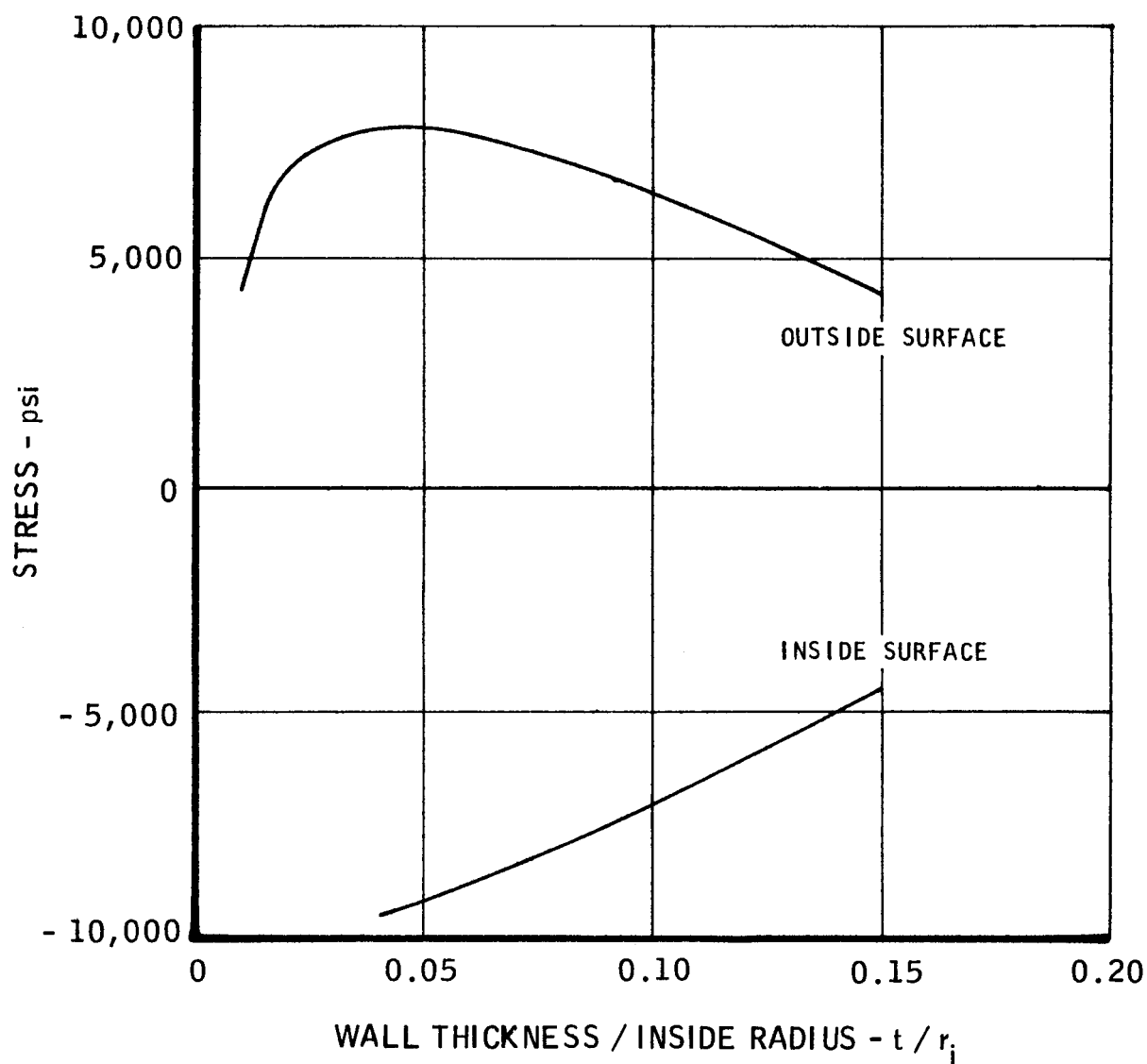


CIRCUMFERENTIAL OPERATING STRESS
THROAT
FOR AS - DEPOSITED MATERIAL

AXIAL OPERATING STRESS
THROAT
FOR AS - DEPOSITED (CONDITION 3) MATERIAL

$$r_i = 1 \text{ inch}$$

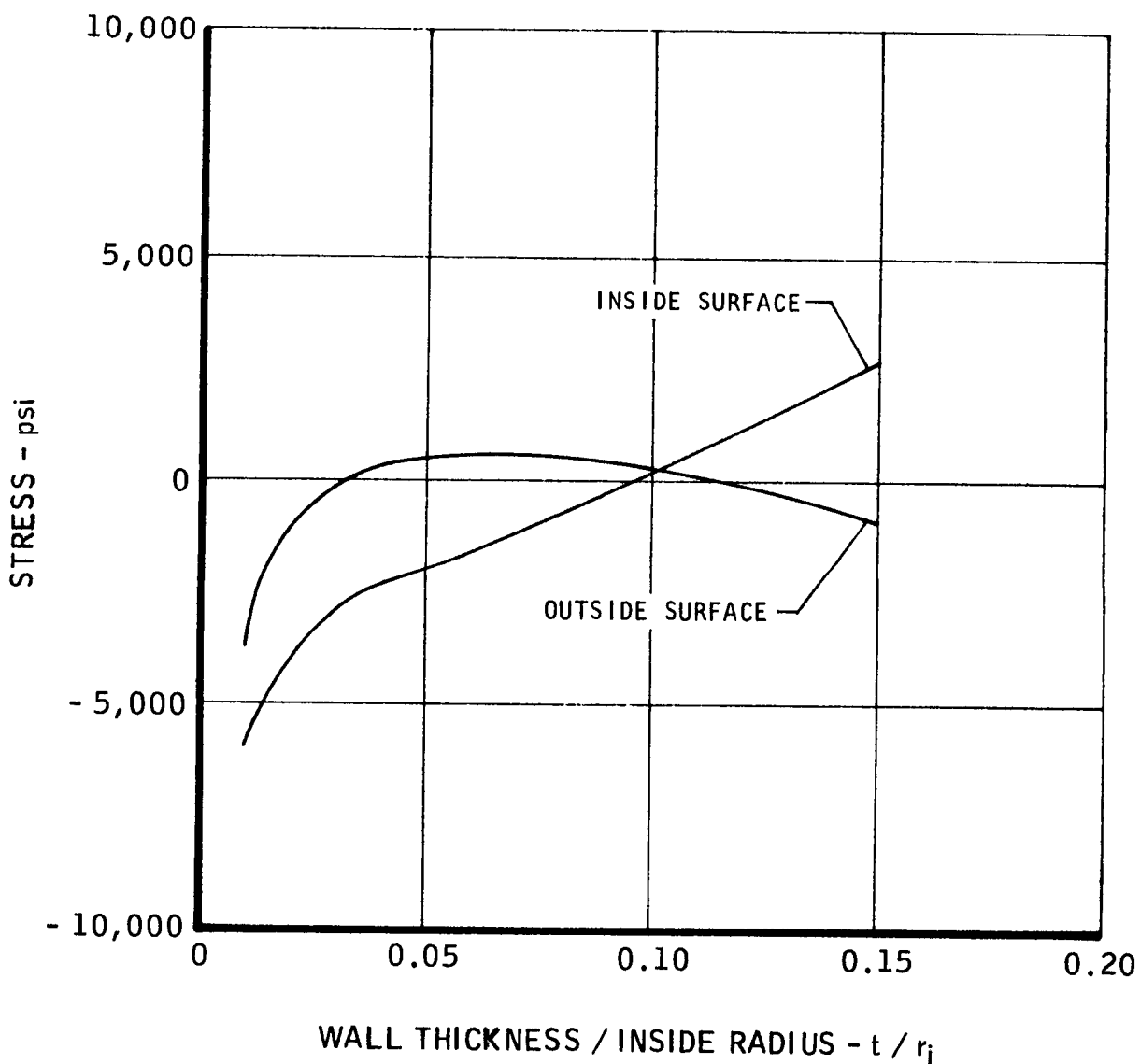
$$P_c = 150 \text{ psia}$$



AXIAL OPERATING STRESS
THROAT

STRESS FREE TEMPERATURE = 0°F

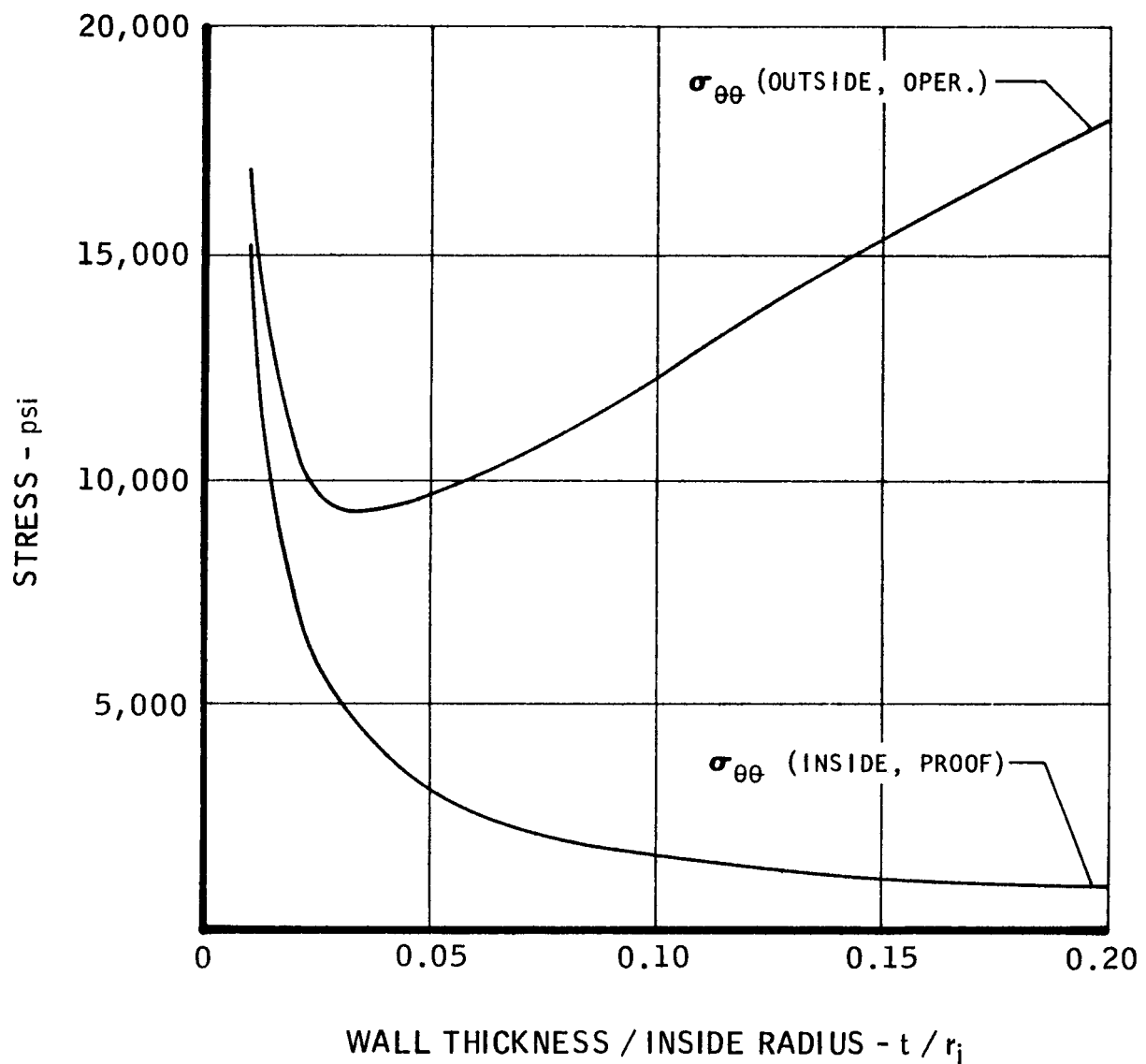
(CONDITION 4)

 $P_c = 150$ psia $r_i = 1$ inch

COMBUSTION CHAMBER STRESSES
STRESS FREE TEMPERATURE 0° F

$$r_i = 2 \text{ inches}$$

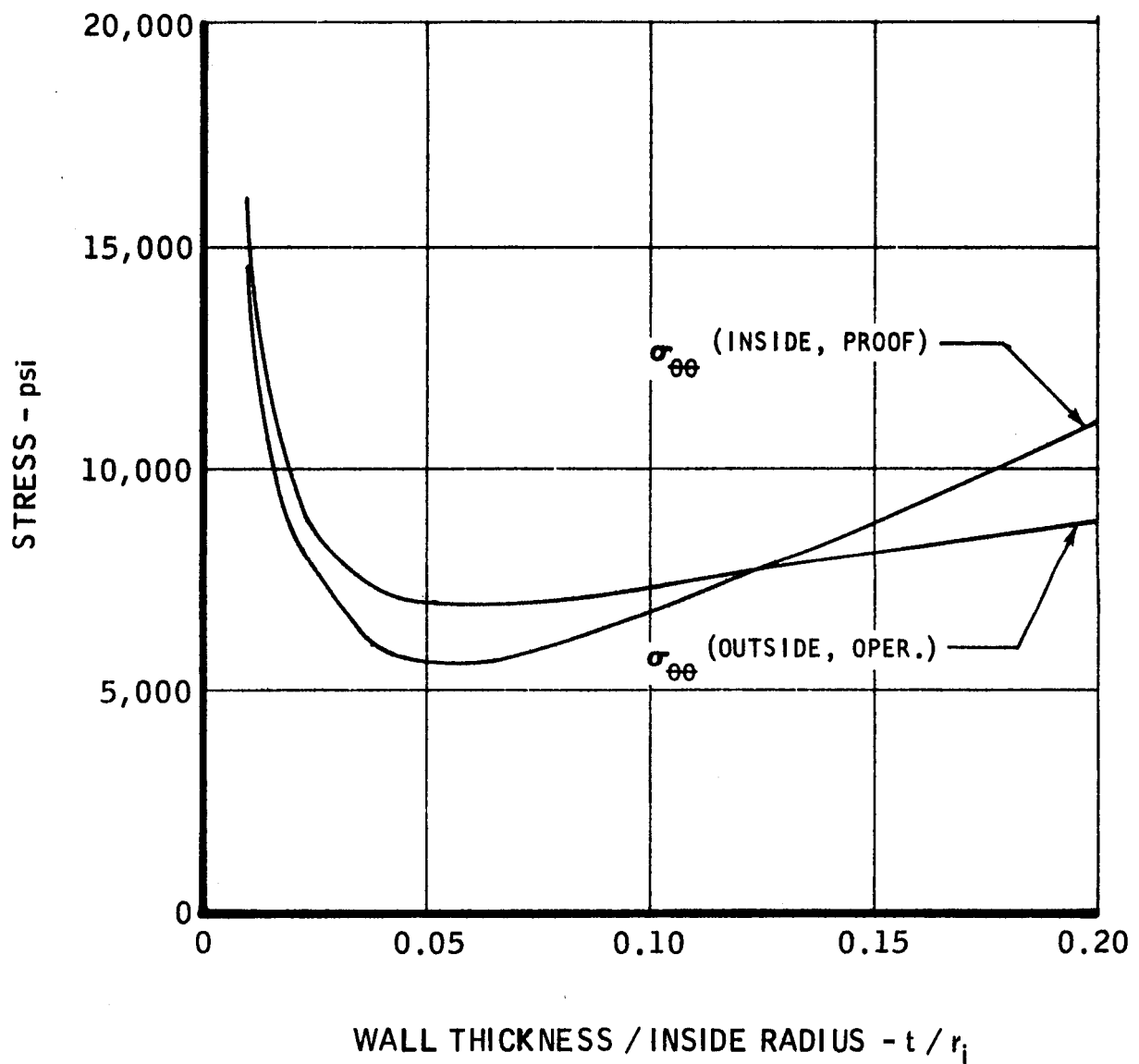
$$P_c = 150 \text{ psia}$$



COMBUSTION CHAMBER STRESSES
STRESS FREE TEMPERATURE = 2,000° F

$$r_i = 2 \text{ inches}$$

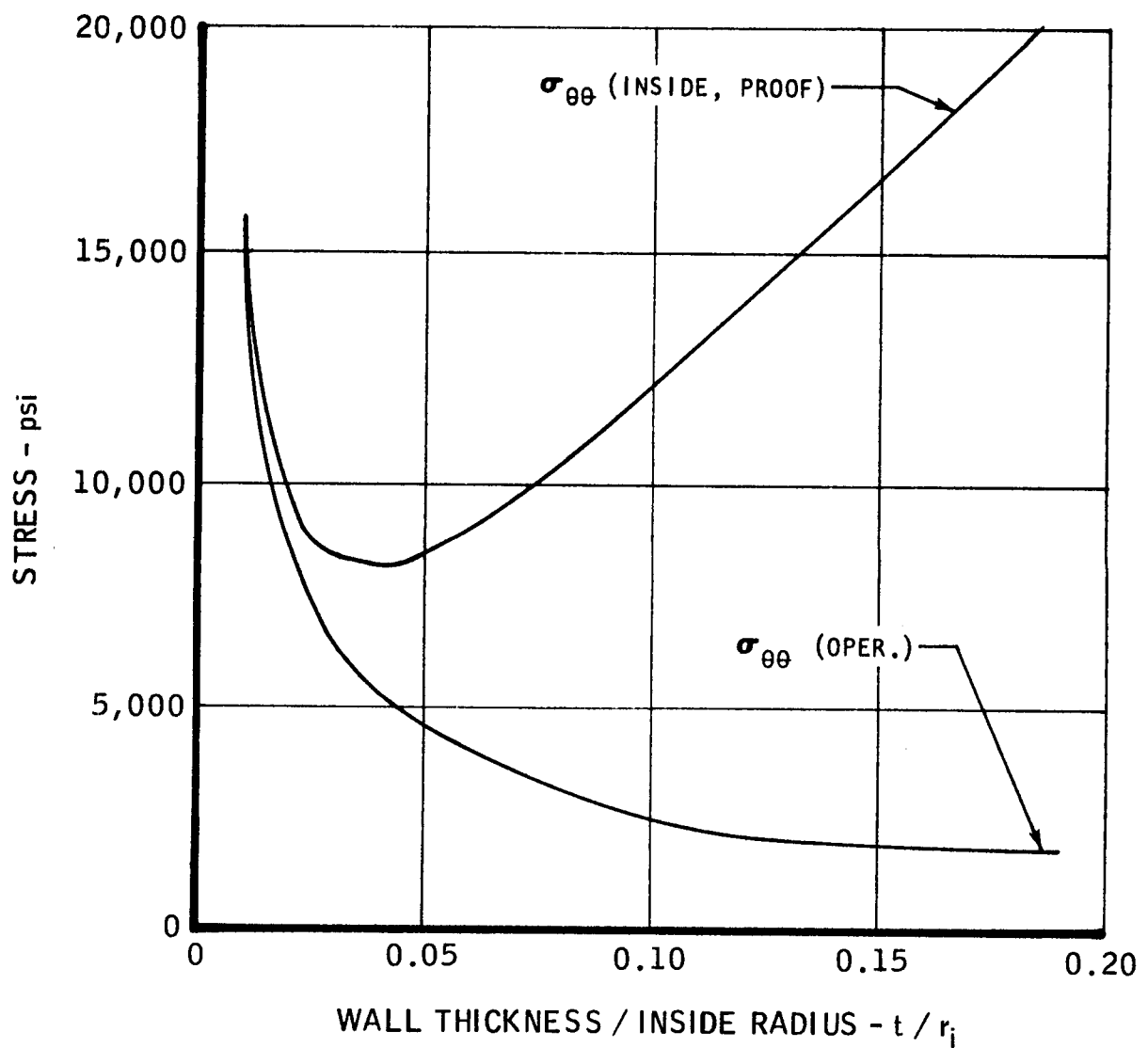
$$P_c = 150 \text{ psia}$$



COMBUSTION CHAMBER STRESSES
STRESS FREE TEMPERATURE - 4,000° F

$$r_i = 2 \text{ inches}$$

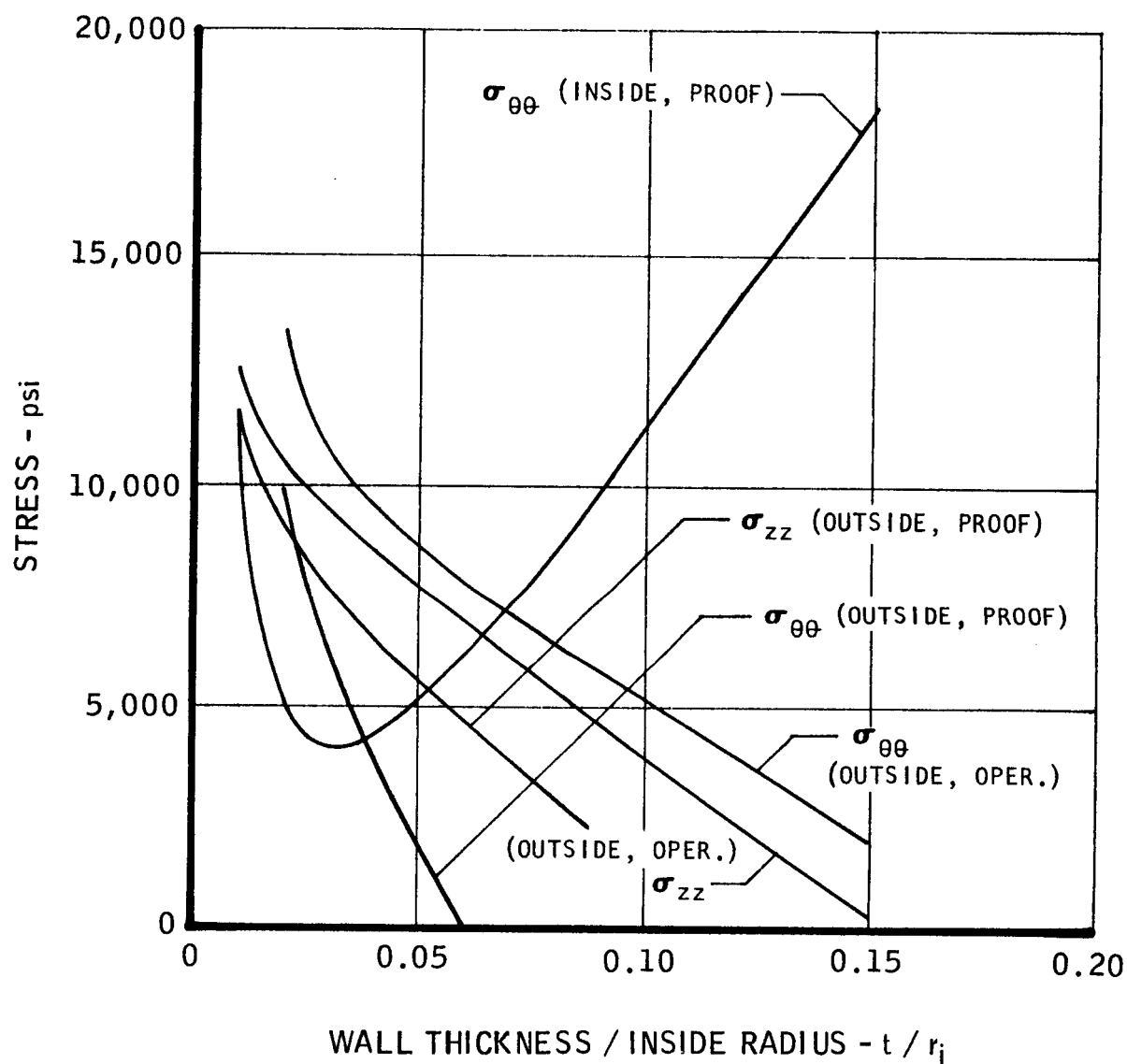
$$P_c = 150 \text{ psia}$$



COMBUSTION CHAMBER STRESSES
FOR AS - DEPOSITED MATERIAL

$$r_i = 2 \text{ inches}$$

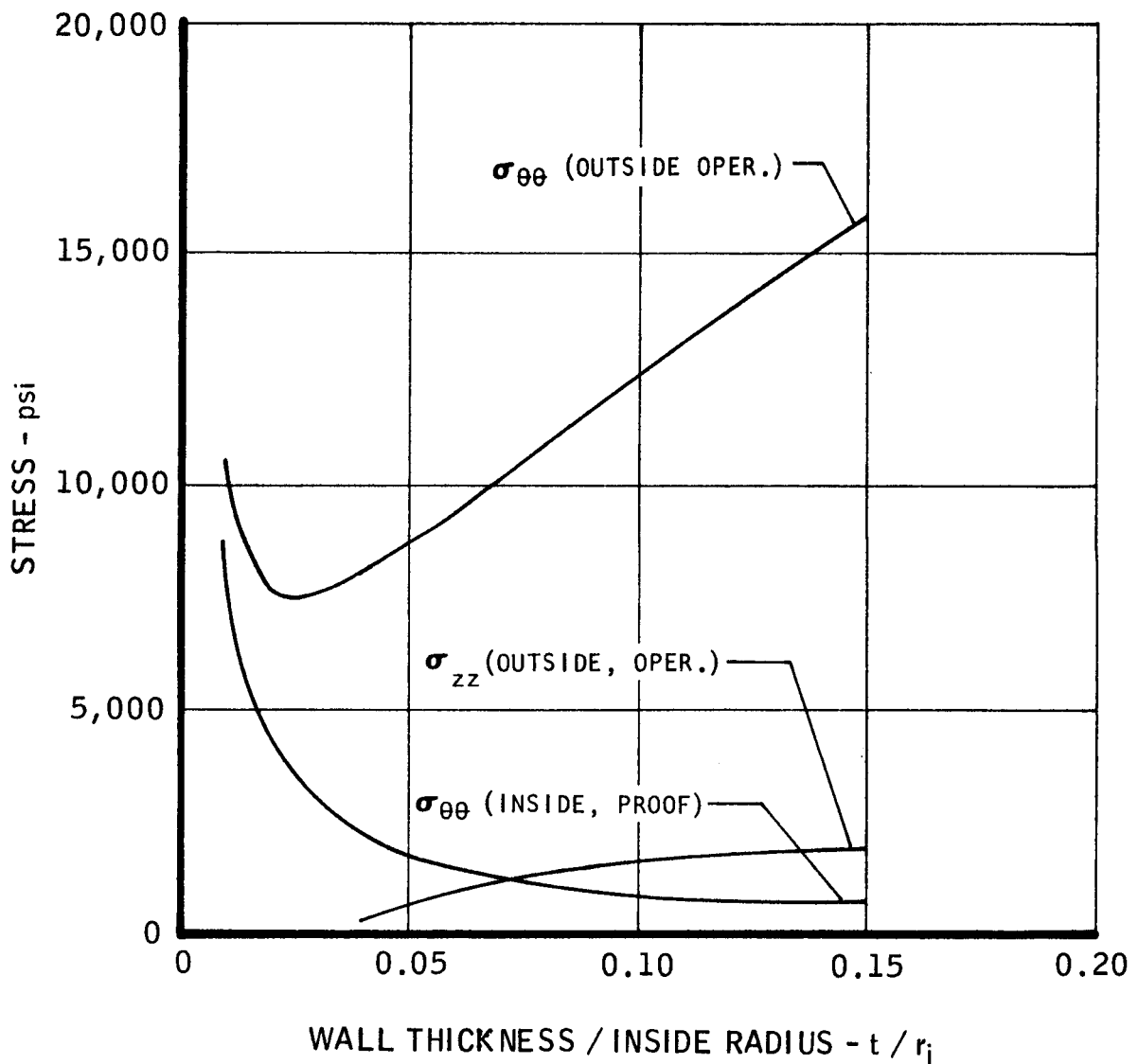
$$P_c = 150 \text{ psia}$$



THROAT STRESSES
STRESS FREE TEMPERATURE 0° F

$$r_i = 1 \text{ inch}$$

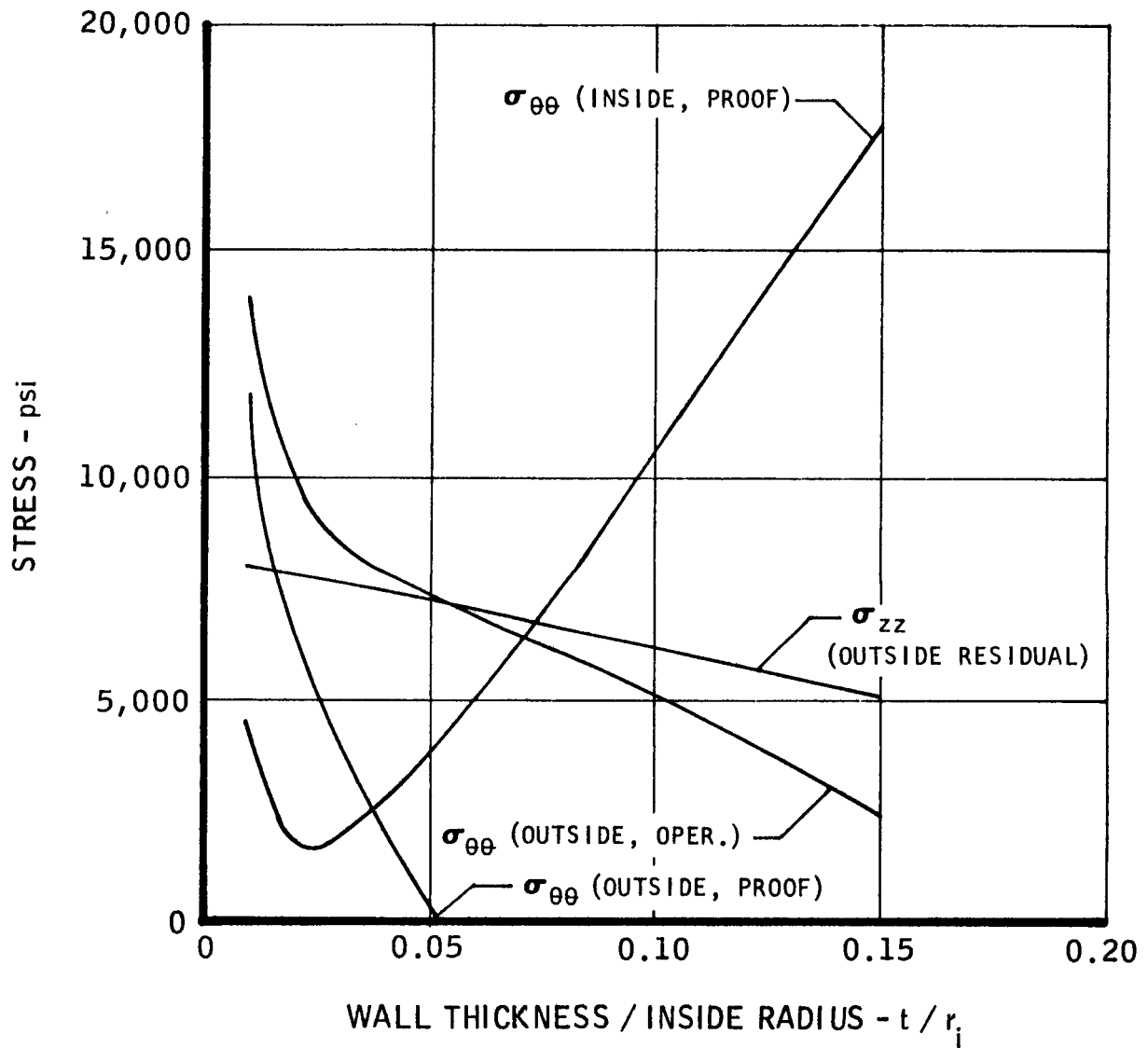
$$P_c = 150 \text{ psia}$$



THROAT STRESSES
FOR AS - DEPOSITED (CONDITION 3) MATERIAL

$$r_i = 1 \text{ inch}$$

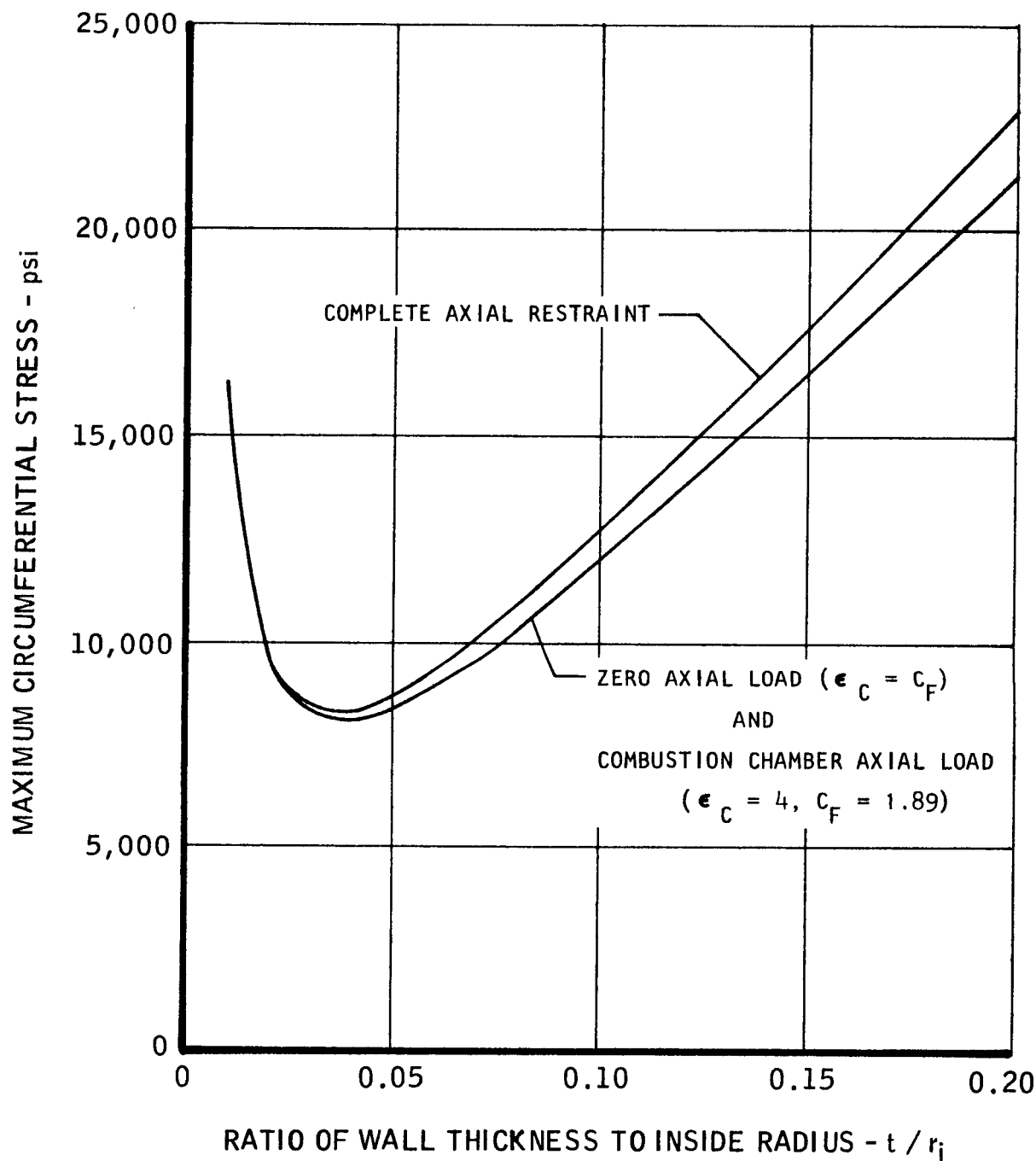
$$P_c = 150 \text{ psia}$$



UNCLASSIFIED

EFFECT OF AXIAL LOAD ON PROOF STRESS MAXIMUM CIRCUMFERENTIAL STRESS PYROLYTIC GRAPHITE CYLINDERS

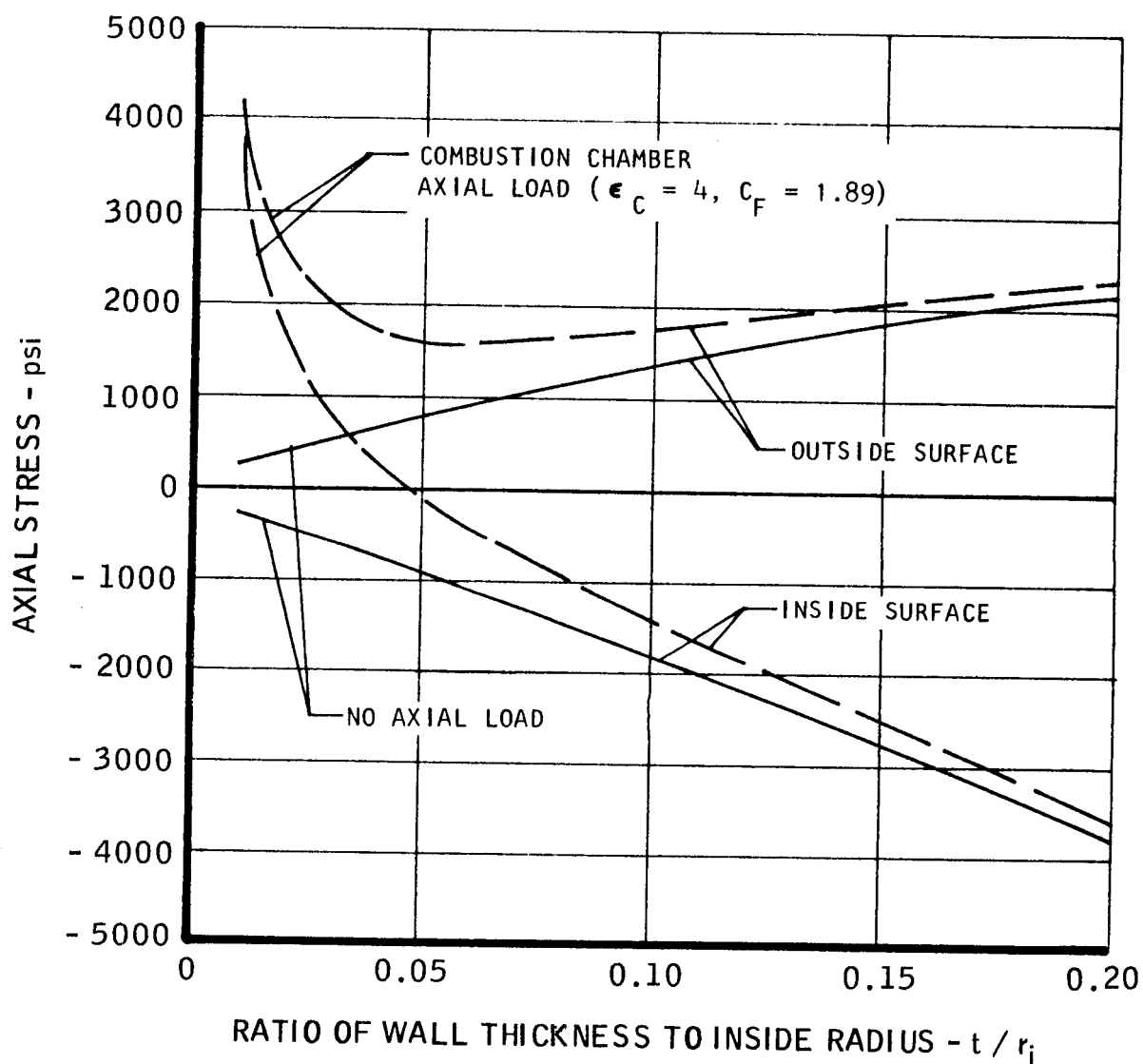
$P = 150$ psia
STRESS FREE TEMPERATURE = 4000°F



MAC A673

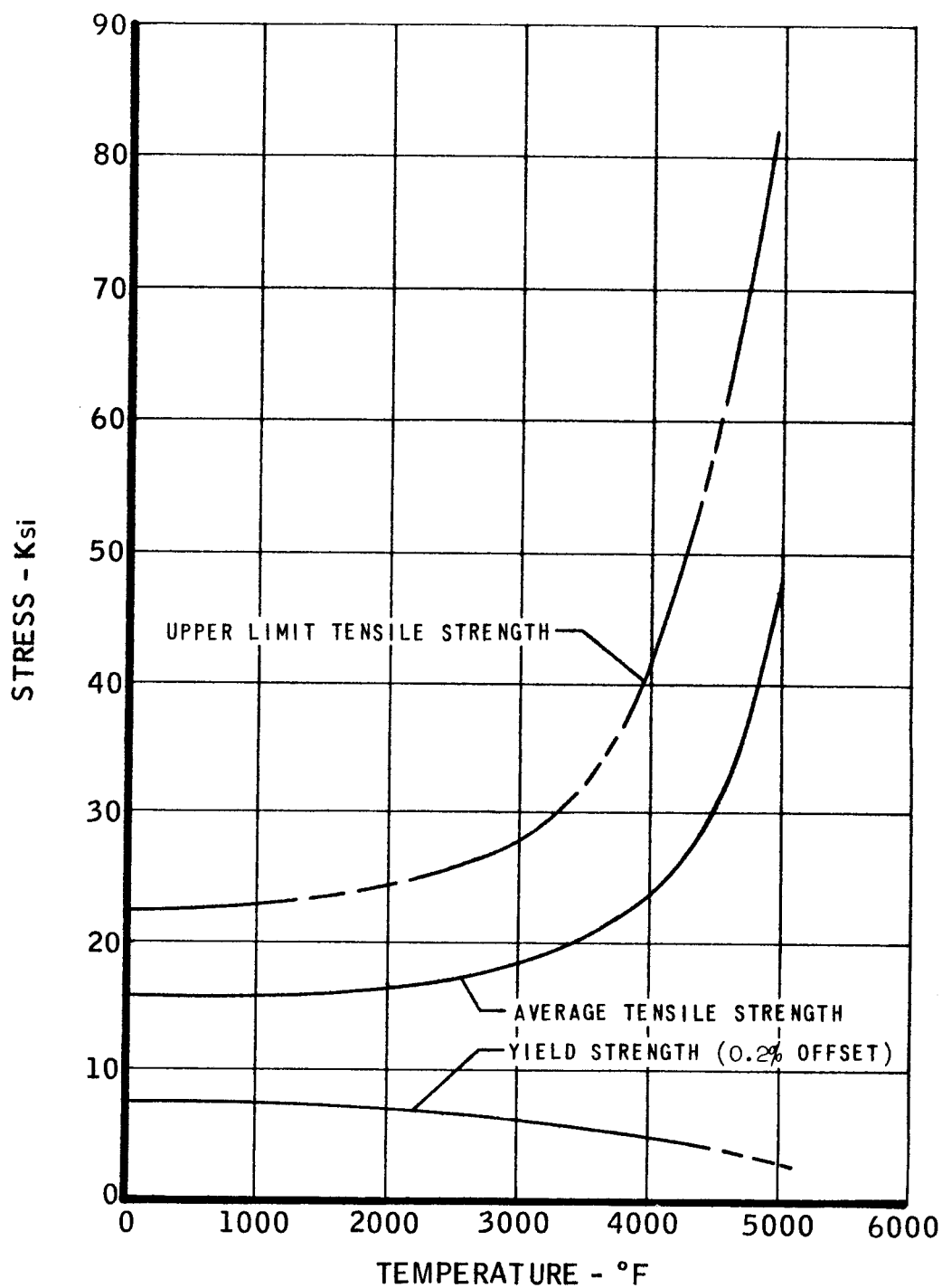
EFFECT OF AXIAL LOAD ON AXIAL PROOF STRESS
PYROLYTIC GRAPHITE CYLINDERS

$P = 150$ psia
STRESS FREE TEMPERATURE = 4000 °F



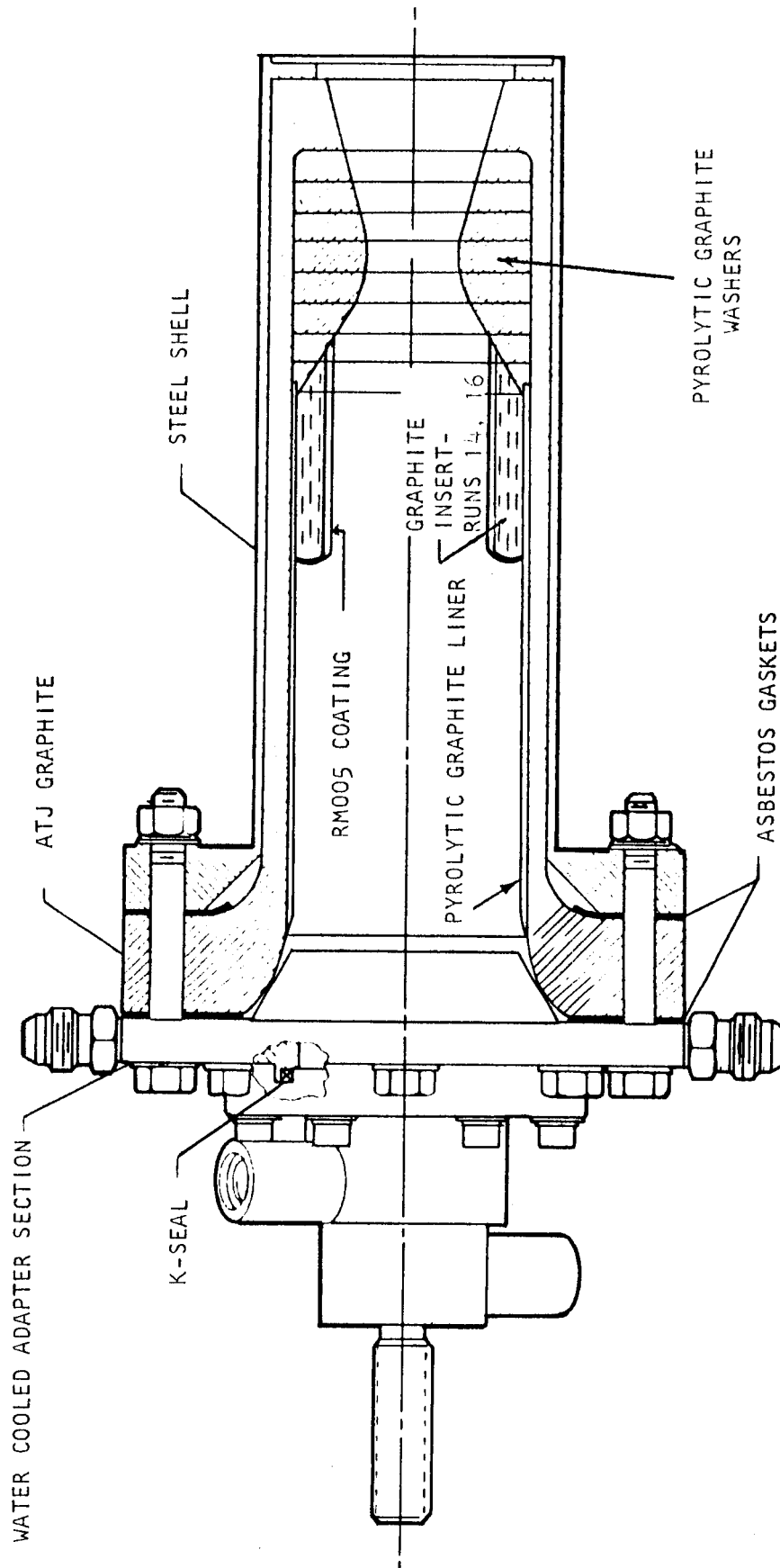
TENSILE AND YIELD STRENGTH OF PYROLYTIC GRAPHITE
IN THE a - DIRECTION

REFERENCE: GENERAL ELECTRIC COMPANY

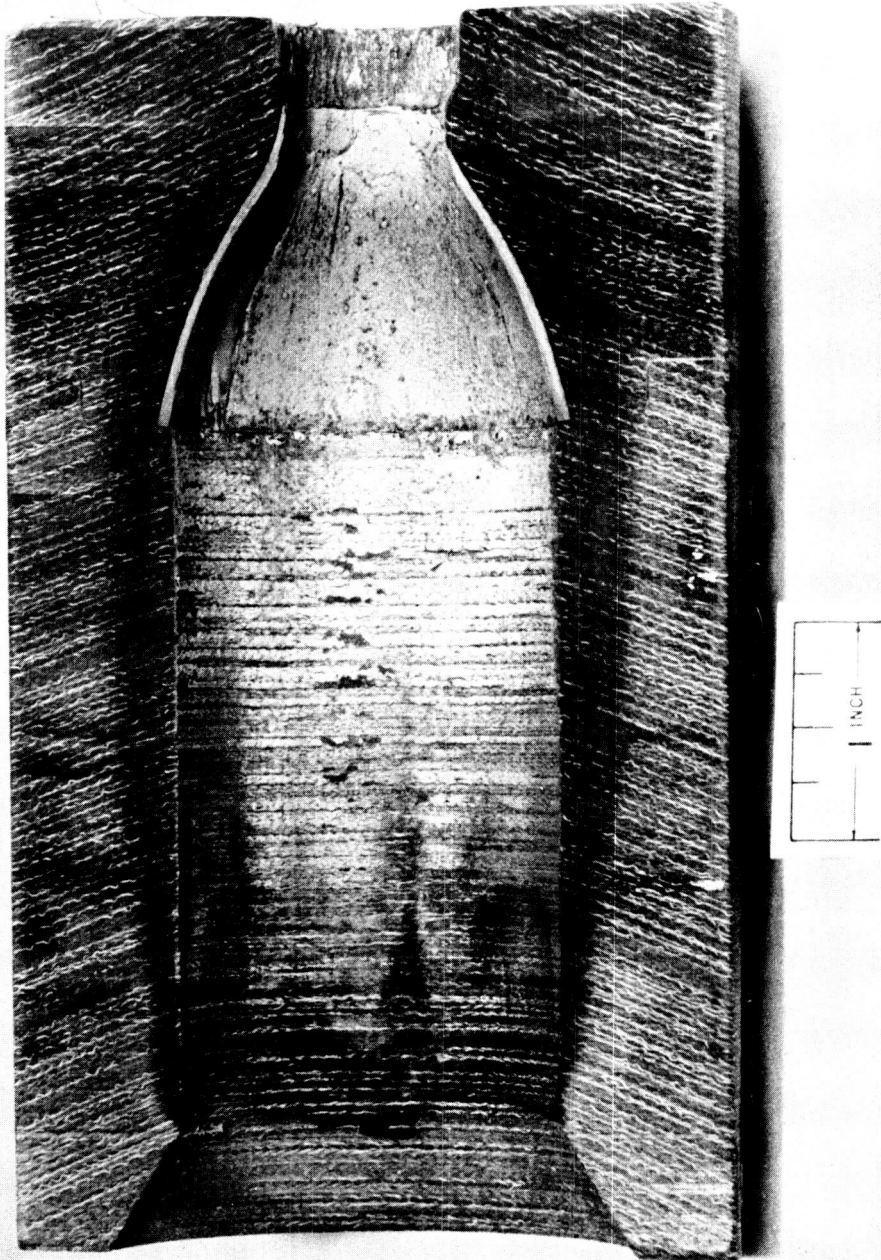


MAC A673

COMPOSITE PYROLYTIC GRAPHITE THRUST CHAMBER ASSEMBLY

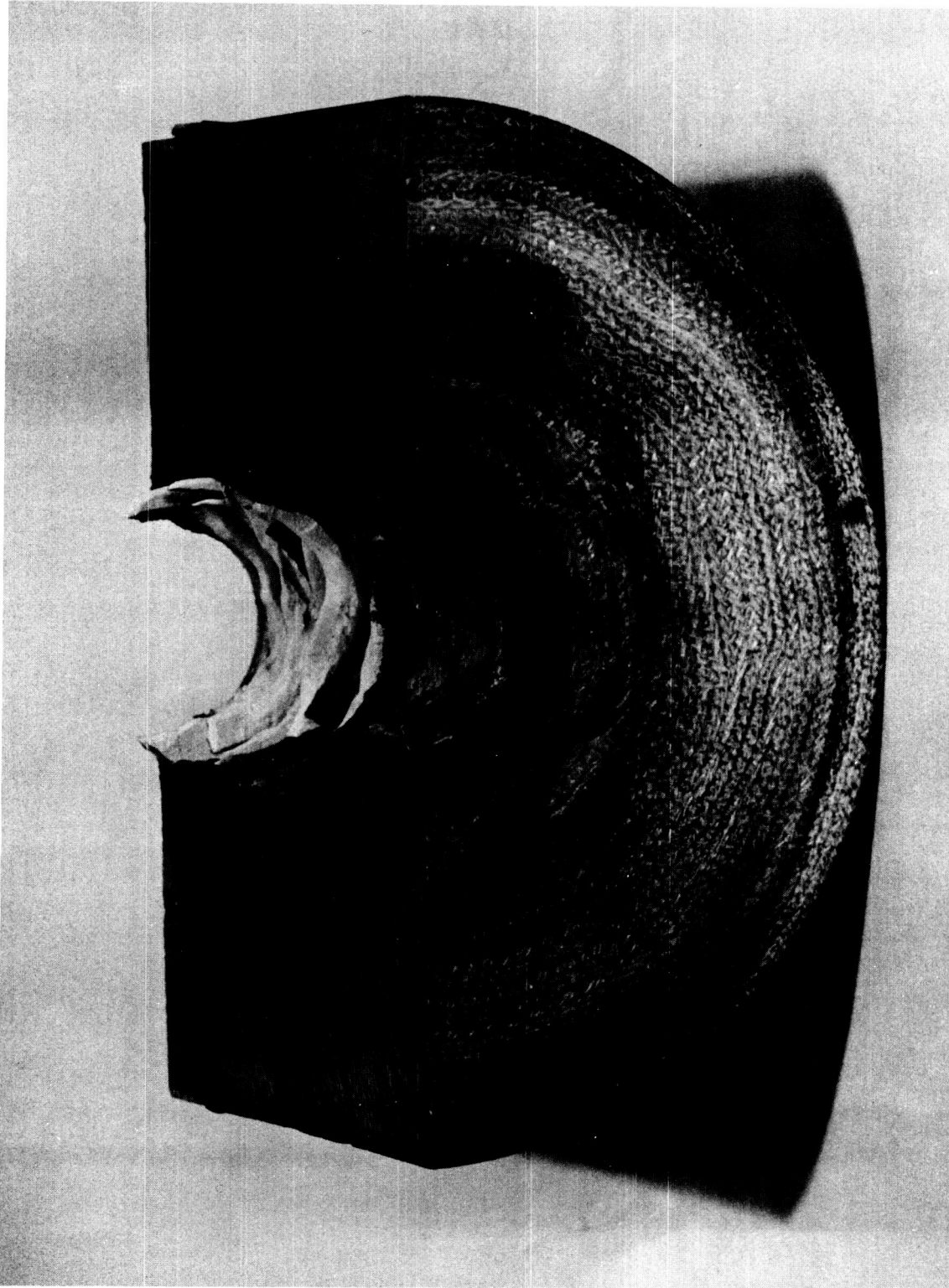


MAC A673



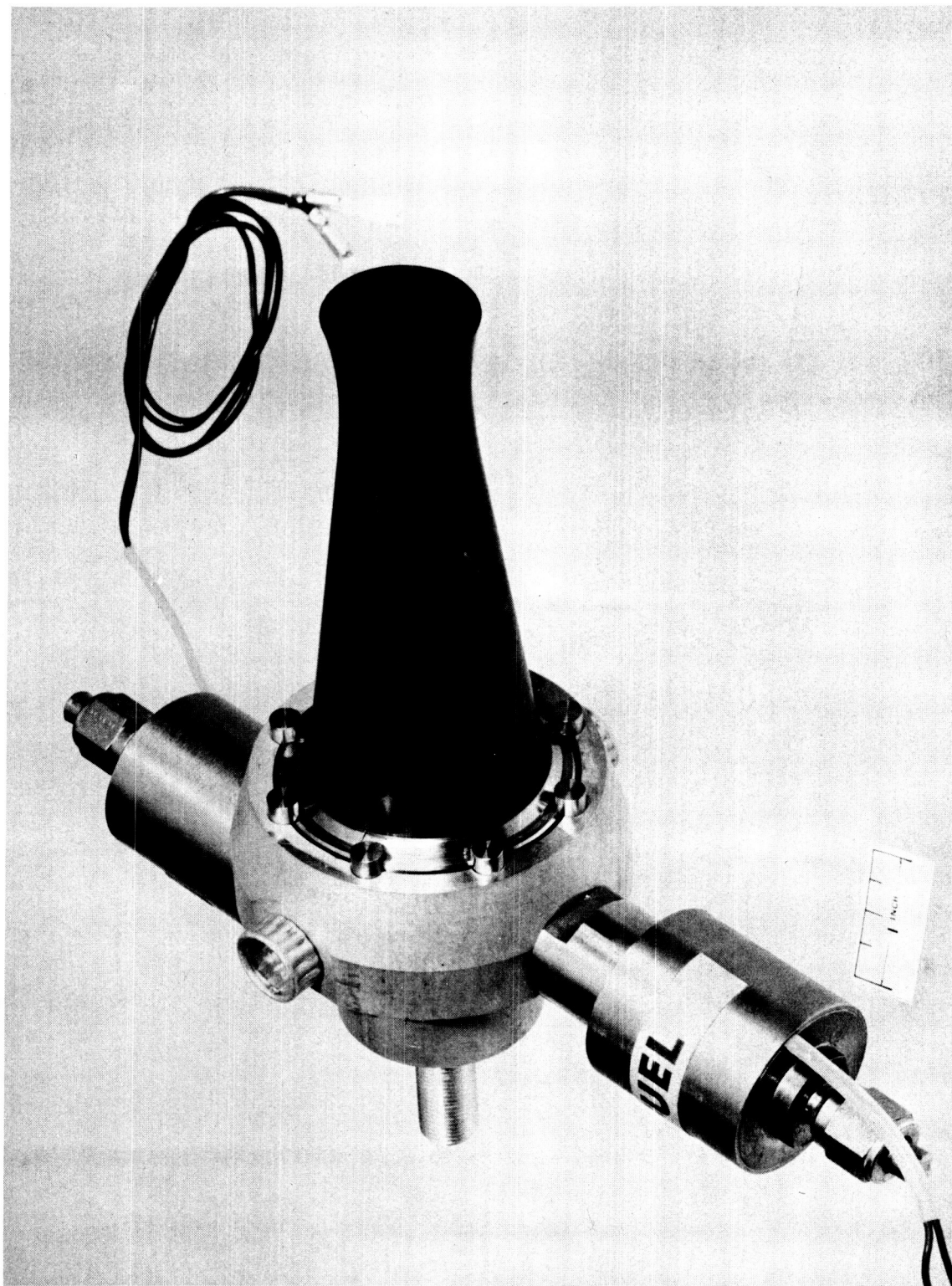
T 3073-28

FIGURE 41 - Free Standing Boron Nitride Throat Insert in Ablative Thrust Chamber



T 3073-9

FIGURE 42 - Pyrolytic Boron Nitride Washer Throat Insert After 300 seconds Burning Time



4697-1

FIGURE 43 - Sea Level Motor and Injector

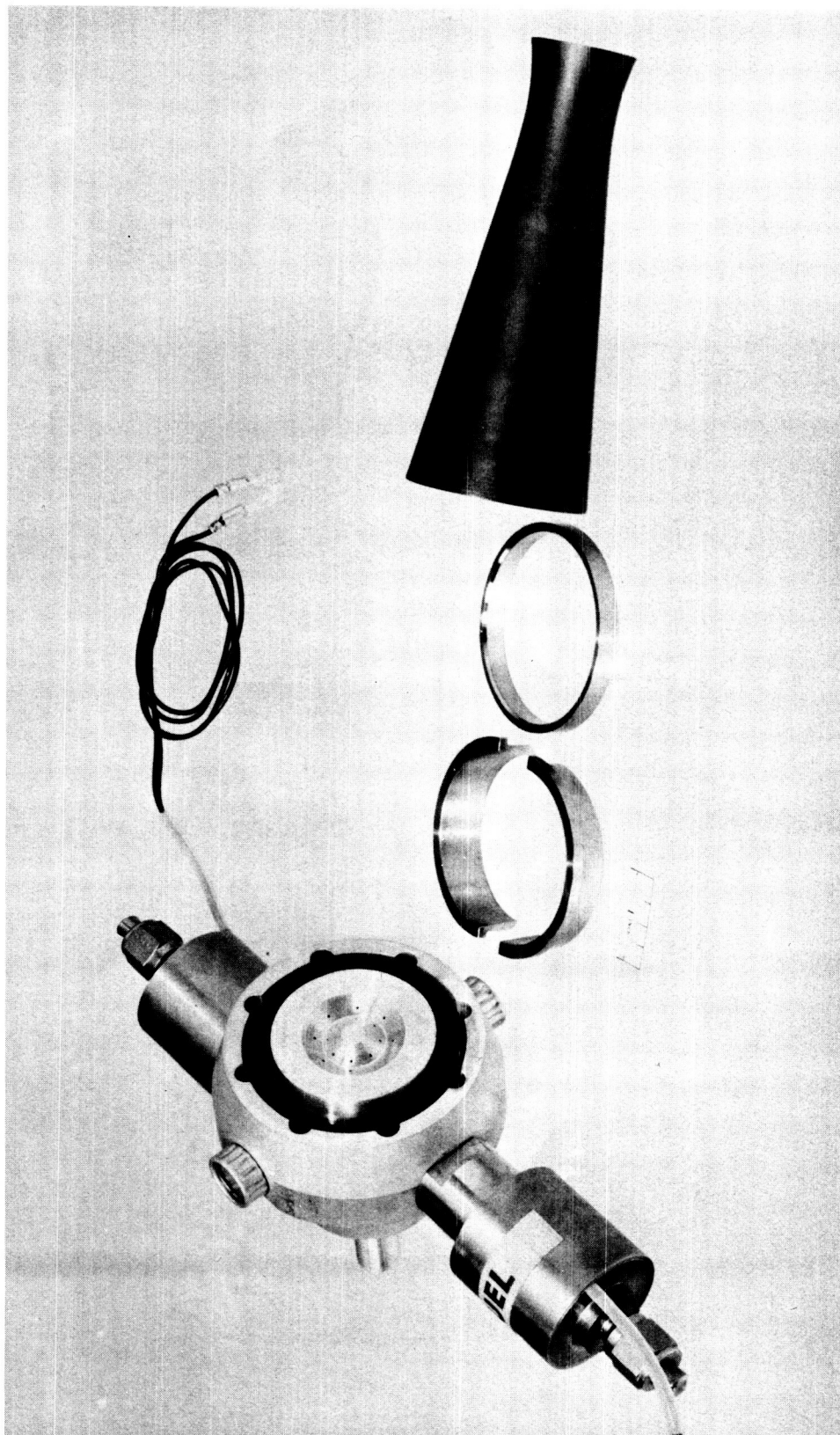


FIGURE 44 - Sea Level Motor and Injector--Disassembled

4697-2

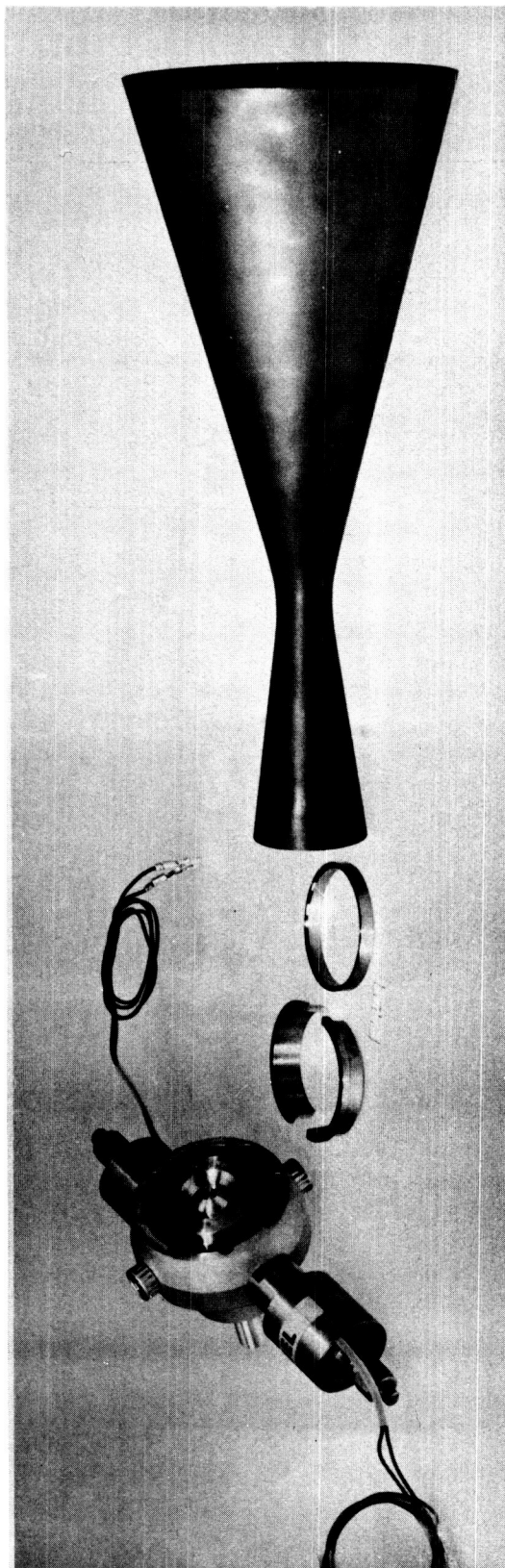
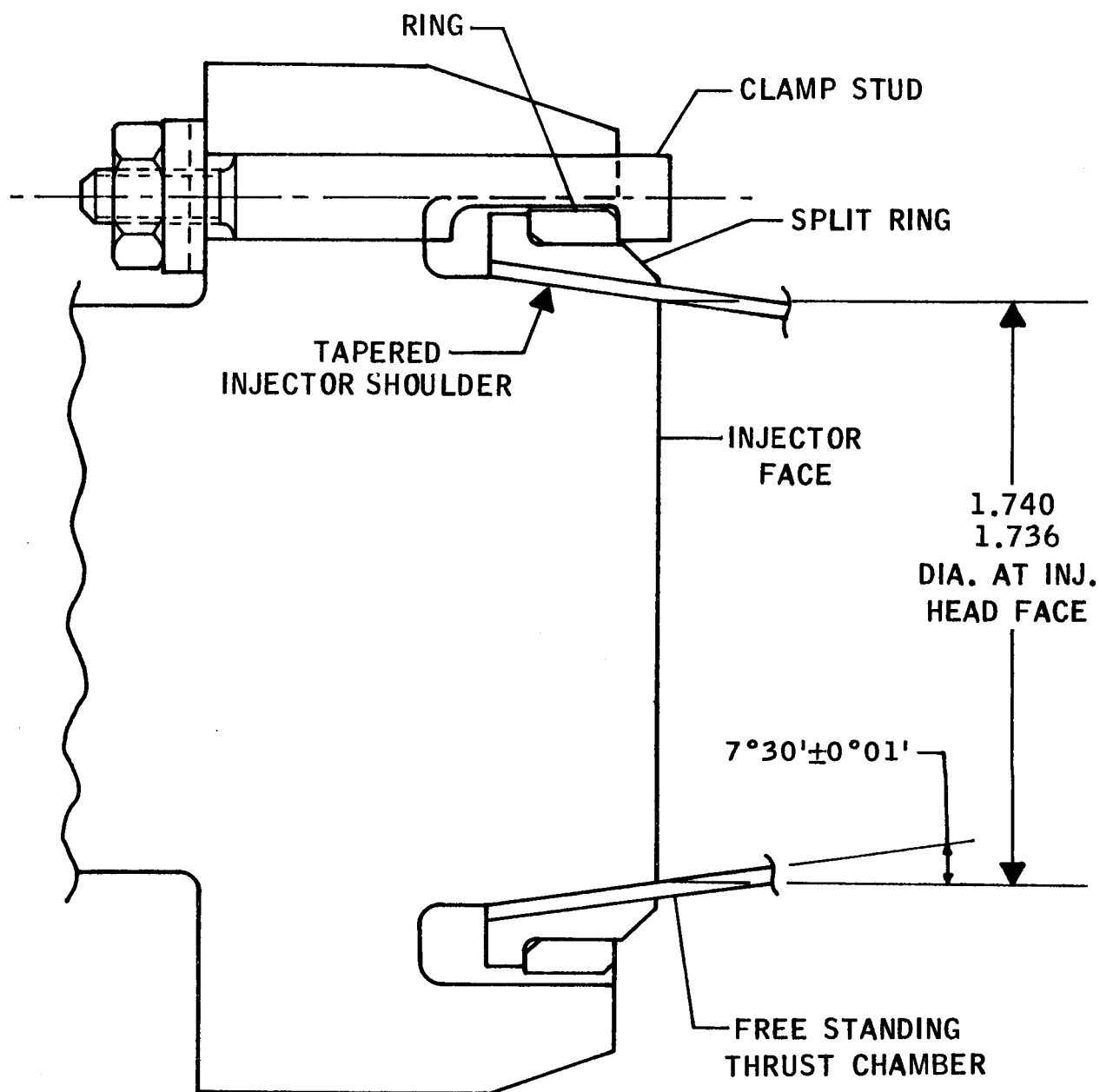


FIGURE 45 - Altitude Motor and Injector--Disassembled

4697-3

TAPERED CHAMBER - INJECTOR JOINT



MAC A673

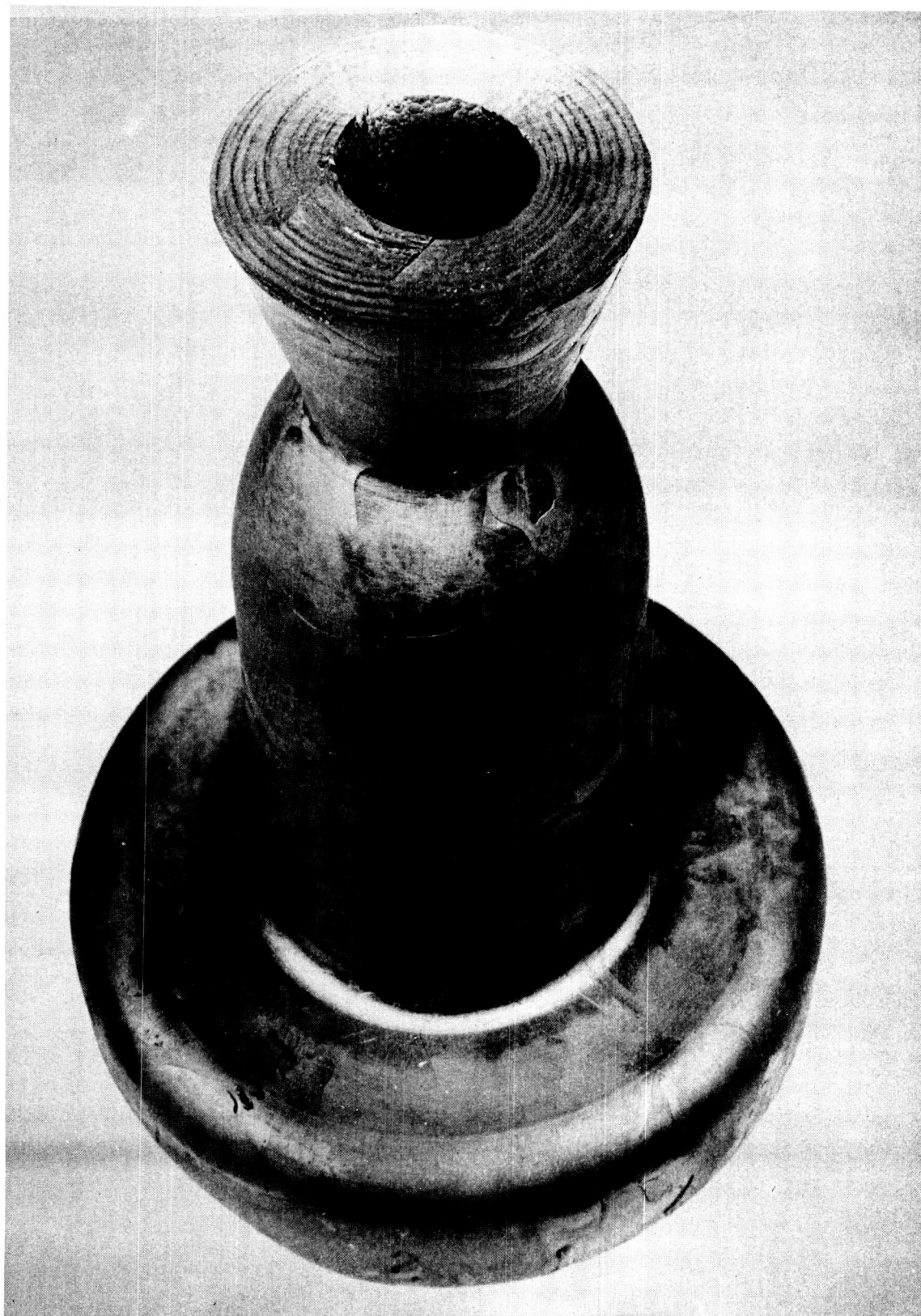


FIGURE 47 - Samco Pyrolytic Graphite Thrust Chamber

4658-4

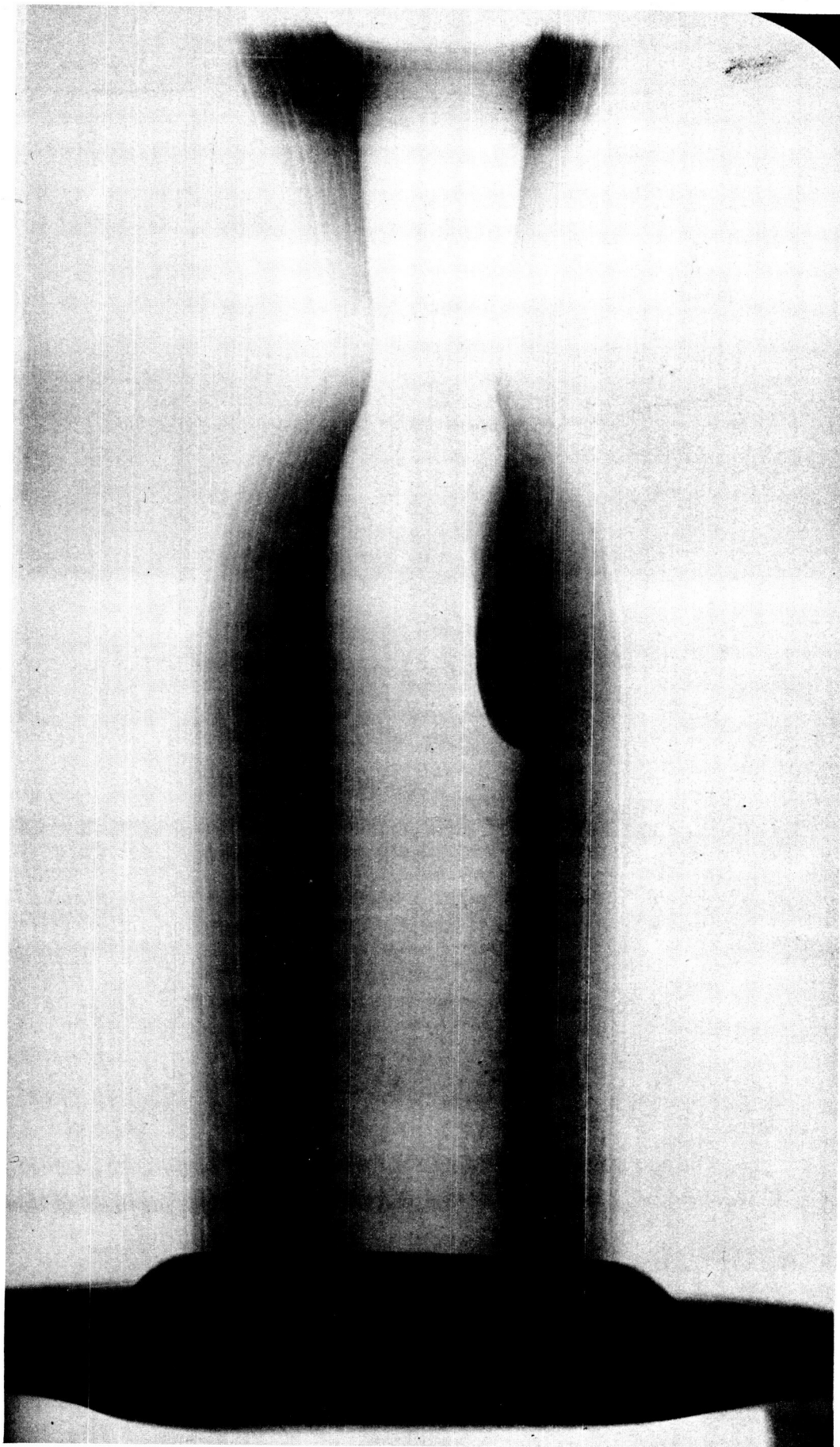


FIGURE 48 - X-Ray Photo of Samco Pyrolytic Graphite Thrust Chamber

MAC A673

APPENDIX A

SUMMARY OF NOMENCLATURE

Symbol	Description	Unit
A_c	Engine cross-sectional flow area	sq in.
A	Dimensionless quantity defined by Eq. (22)	--
a_o	Constant defined by Eq. (27)	--
a_1	Constant defined by Eq. (27)	--
B	Constant defined by Eq. (31)	--
c	Elastic stiffnesses	$\frac{\text{lb/in.}^2}{\text{in./in.}}$
C	Constant defined by Eq. (32)	--
C_1	Constant of integration	--
C_F	Thrust Coefficient	--
C_2	Constant of integration	--
C_3	Constant axial strain	--
C^*	Characteristic velocity	fps
D	Constant defined by Eq. (33)	--
D_*	Throat diameter	ins.
E	Modulus of elasticity (Young's Modulus)	$\frac{\text{lb/in.}^2}{\text{in./in.}}$
F_{zz}	Axial load on cylindrical combustion chamber	lbs
H_j	Constants defined for $j = 1 - 5$ by Eqs. (36) to (40)	--
O/F	Oxidizer/fuel flow rate ratio	--
P_c	Chamber pressure	psia
r	Radius of motor shell	in.
r_o	Outside radius of motor shell	in.
r_i	Inside radius of motor shell	in.
s	Elastic compliances	$\frac{\text{in./in.}}{\text{lb/in.}^2}$
T	Temperature increment from stress-free state	$^{\circ}\text{F}$

APPENDIX A (Continued)

Symbol	Description	Unit
T_c	Combustion gas total temperature	$^{\circ}\text{F}$
t	Thickness of motor shell	in.
u	Radial deflection of motor shell	in.
V_1	Integral defined by Eq. (25)	--
V_2	Integral defined by Eq. (26)	--
α	Coefficient of thermal expansion	in./in./ $^{\circ}\text{F}$
ϵ	Elastic strain	in./in.
ϵ_c	Chamber contraction ratio	--
λ	Thermal stress coefficient	--
ν	Poisson's ratio	--
σ	Elastic stress	lb/in. ²
$\sigma_{\theta\theta}$	Hoop stress	psi
σ_{zz}	Axial stress	psi
$\phi(r)$	Defined by Eq. (23)	--

DISTRIBUTION

<u>Copy No.</u>	<u>Transmitted to</u>
1.	NASA Western Operations Office 150 Pico Boulevard Santa Monica, California Attn.: Office of Technical Information
2.	NASA Western Operations Office 150 Pico Boulevard Santa Monica, California Attn.: Contracting Officer
3.	NASA Western Operations Office 150 Pico Boulevard Santa Monica, California Attn.: Patent Office
4 to 7.	National Aeronautics and Space Administration 400 Maryland Avenue, S.W. Washington 25, D.C. Attn.: Chief, Liquid Propulsion Systems (Code RPL), Mr. H. Burlage, Jr.
8.	National Aeronautics and Space Administration 400 Maryland Avenue, S.W. Washington 25, D.C. Attn.: Asst. Director for Propulsion (Code MLP), Mr. A. O. Tischler
9 to 33.	National Aeronautics and Space Administration P.O. Box 5700 Bethesda, Maryland Attn.: Scientific and Technical Information Facility (Code CRT), NASA Representative
34.	Jet Propulsion Laboratory 4800 Oak Grove Drive Pasadena, California Attn.: Mr. A. Briglio
35, 36.	National Aeronautics and Space Administration Ames Research Center Moffett Field, California Attn.: Technical Librarian
37, 38.	National Aeronautics and Space Administration Goddard Space Flight Center Greenbelt, Maryland Attn.: Technical Librarian

UNCLASSIFIED

DISTRIBUTION (Continued)

<u>Copy No.</u>	<u>Transmitted to</u>
39, 40.	Jet Propulsion Laboratory California Institute of Technology 4800 Oak Grove Drive Pasadena, California Attn.: Technical Librarian
41, 42.	National Aeronautics and Space Administration Langley Research Center Langley Field Hampton, Virginia Attn.: Technical Librarian
43, 44.	National Aeronautics and Space Administration Lewis Research Center 21000 Brookpark Road Cleveland 35, Ohio Attn.: Technical Librarian
45, 46.	National Aeronautics and Space Administration Marshall Space Flight Center Huntsville, Alabama Attn.: Technical Librarian
47, 48.	National Aeronautics and Space Administration Manned Spacecraft Center Houston, Texas Attn.: Technical Librarian
49.	Advanced Research Projects Agency The Pentagon, Room 3D154 Washington 25, D.C. Attn.: Technical Librarian
50.	Commander Aeronautical Systems Division Air Force Systems Command Wright-Patterson Air Force Base, Ohio Attn.: Technical Librarian
51.	Air Force Missile Development Center Holloman Air Force Base, New Mexico Attn.: Technical Librarian
52.	Air Force Missile Test Center Patrick Air Force Base, Florida Attn.: Technical Librarian

MAC A673

UNCLASSIFIED

UNCLASSIFIED

DISTRIBUTION (Continued)

<u>Copy No.</u>	<u>Transmitted to</u>
53.	Air Force Systems Command Dyna-Soar Air Force Unit Post Office Los Angeles 45, California Attn: Technical Librarian
54.	Army Ordnance Missile Command Redstone Arsenal, Alabama Attn.: Technical Librarian
55.	Arnold Engineering Development Center Tullahoma, Tennessee Attn.: Technical Librarian
56.	Bureau of Naval Weapons Department of the Navy Washington 25, D.C. Attn.: Technical Librarian
57.	Central Intelligence Agency 2430 E Street, N.W. Washington 25, D.C. Attn.: Technical Librarian
58.	Headquarters, United States Air Force Washington 25, D.C. Attn.: Technical Librarian
59.	Picatinny Arsenal Dover, New Jersey Attn.: Technical Librarian
60.	Rocket Research Laboratories Edwards Air Force Base, California Attn.: Technical Librarian
61.	U.S. Naval Ordnance Test Station China Lake, California Attn.: Technical Librarian
62.	U.S. Atomic Energy Commission Technical Information Services Box 62 Oak Ridge, Tennessee Attn.: Technical Librarian

MAC A673

UNCLASSIFIED

DISTRIBUTION (Continued)

<u>Copy No.</u>	<u>Transmitted to</u>
63.	Defense Documentation Center Headquarters Cameron Station, Building 5 5010 Duke Street Alexandria, Virginia Attn.: TISIA
64.	Chemical Propellant Information Agency Johns Hopkins University Applied Physics Laboratory 8621 Georgia Avenue Silver Spring, Maryland Attn.: Technical Librarian
65.	Aerojet-General Corporation P.O. Box 296 Azusa, California Attn.: Technical Librarian
66.	Aerojet-General Corporation P.O. Box 1947 Sacramento 9, California Attn.: Technical Librarian
67.	Aeronutronic A Division of Ford Motor Company Ford Road Newport Beach, California Attn.: Technical Librarian
68.	Aerospace Corporation 2400 East El Segundo Boulevard El Segundo, California Attn.: Technical Librarian
69.	Arthur D. Little, Inc. Acorn Park Cambridge 40, Massachusetts Attn.: Technical Librarian
70.	Astropower, Inc. A Subsidiary of Douglas Aircraft Company, Inc. 2968 Randolph Avenue Costa Mesa, California Attn.: Technical Librarian
71.	Astrosystems, Inc. 82 Naylon Avenue Livingston, New Jersey Attn.: Technical Librarian

DISTRIBUTION (Continued)

<u>Copy No.</u>	<u>Transmitted to</u>
72.	Atlantic Research Corporation Edsall Road and Shirley Highway Alexandria, Virginia Attn.: Technical Librarian
73.	Beech Aircraft Corporation Boulder Facility Box 631 Boulder, Colorado Attn.: Technical Librarian
74.	Bell Aerosystems Company P.O. Box 1 Buffalo 5, New York Attn.: Technical Librarian
75.	Bendix Systems Division Bendix Corporation Ann Arbor, Michigan Attn.: Technical Librarian
76.	Boeing Company P.O. Box 3707 Seattle 24, Washington Attn.: Technical Librarian
77.	Convair (Astronautics) Division of General Dynamics Corporation P.O. Box 2672 San Diego 12, California Attn.: Technical Librarian
78.	Curtiss-Wright Corporation Wright Aeronautical Division Woodridge, New Jersey Attn.: Technical Librarian
79.	Douglas Aircraft Company, Inc. Missile and Space Systems Division 3000 Ocean Park, Boulevard Santa Monica, California Attn.: Technical Librarian
80.	Fairchild Stratos Corporation Aircraft Missiles Division Hagerstown, Maryland Attn.: Technical Librarian

DISTRIBUTION (Continued)

<u>Copy No.</u>	<u>Transmitted to</u>
81.	General Electric Company Missile and Space Vehicle Department Box 8555 Philadelphia, Pennsylvania Attn.: Technical Librarian
82.	General Electric Company Rocket Propulsion Units Building 300 Cincinnati 15, Ohio Attn.: Technical Librarian
83.	Grumman Aircraft Engineering Corporation Bethpage, Long Island, New York Attn.: Technical Librarian
84.	Kidde Aero-Space Division Walter Kidde and Company, Inc. 675 Main Street Belleville 9, New Jersey Attn.: Technical Librarian
85.	Lockheed Aircraft Corporation Missile and Space Division Sunnyvale, California Attn.: Technical Librarian
86.	Lockheed Propulsion Company P.O. Box 111 Redlands, California Attn.: Technical Librarian
87.	Martin Marietta Corporation Martin Division Baltimore 3, Maryland Attn.: Technical Librarian
88.	Martin Marietta Corporation Martin Denver Division Denver, Colorado Attn.: Technical Librarian
89.	McDonnell Aircraft Corporation P.O. Box 6101 Lambert Field, Missouri Attn.: Technical Librarian

DISTRIBUTION (Continued)

<u>Copy No.</u>	<u>Transmitted to</u>
90.	North American Aviation, Inc. Space and Information Systems Division Downey, California Attn.: Technical Librarian
91.	Northrop Corporation 1001 East Broadway Hawthorne, California Attn.: Technical Librarian
92.	Pratt & Whitney Aircraft Corporation Florida Research & Development Center West Palm Beach, Florida Attn.: Technical Librarian
93.	Lockheed California Company 10445 Glen Oaks Boulevard Pacoima, California Attn.: Technical Librarian
94.	Radio Corporation of America Astro-Electronics Division Defense Electronic Products Princeton, New Jersey Attn.: Technical Librarian
95.	Thiokol Chemical Corporation Reaction Motors Division Denville, New Jersey Attn.: Technical Librarian
96.	Republic Aviation Corporation Farmingdale, Long Island, New York Attn.: Technical Librarian
97.	Rocketdyne Division of North American Aviation, Inc. 6633 Canoga Avenue Canoga Park, California Attn.: Technical Librarian
98.	Space-General Corporation 9200 Flair Avenue El Monte, California Attn.: Technical Librarian
99.	Space Technology Laboratories P.O. Box 95001, Airport Station Los Angeles 45, California Attn.: Technical Librarian

DISTRIBUTION (Continued)

<u>Copy No.</u>	<u>Transmitted to</u>
100.	Stanford Research Institute 333 Ravenswood Avenue Menlo Park, California Attn.: Technical Librarian
101.	Thompson-Ramo-Wooldridge, Inc. TAPCO Division 23555 Euclid Avenue Cleveland 17, Ohio Attn.: Technical Librarian
102.	Thiokol Chemical Corporation Redstone Division Huntsville, Alabama Attn.: Technical Librarian
103.	United Aircraft Corporation East Hartford Plant 400 Main Street Hartford, Connecticut Attn.: Technical Librarian
104.	United Technology Corporation 587 Methilda Avenue Sunnyvale, California Attn.: Technical Librarian
105.	Vought Astronautics Box 5907 Dallas 22, Texas Attn.: Technical Librarian